Simulation of Flares from the Galactic Center Black Hole

Nico Hamaus

Simulation of Flares from the Galactic Center Black Hole

Diploma thesis

Nico Hamaus

Max Planck Institute for Extraterrestrial Physics

Ludwig-Maximilians-Universität München

Referees:
Prof. Dr. Reinhard Genzel
Prof. Dr. Andreas Burkert

Submission date: 08.01.2008

Abstract

This thesis is a theoretical work dealing with the flares from the Galactic Center. On the basis of a physical model for this phenomenon (*hot spot model*), simulations are used to investigate its observational implications. To this end light curves and centroid motions from the emission region close to a supermassive black hole are generated with the help of general relativistic ray tracing methods.

Furthermore the influence of various parameters of this model is studied in detail to help constrain some properties of the Galactic Center black hole and its immediate environment from future observations. Existing measurements of flare light curves are used to determine some of these parameters, whereas others are anticipated by the model.

As a result we find the hot spot model to be in good agreement with the observations and give some constraints on the shape and evolution of the hot spot. Simulations for the astrometric motion of the flares anticipate the observability of high-order general relativistic effects with instruments of the next generation. We present two examples of such an observation on the basis of available flare data. The resulting centroid tracks serve as theoretical predictions of the hot spot model and particularly general relativity.

Contents

1 Introduction **4**
- 1.1 Observations of the Galactic Center . . . 4
  - 1.1.1 Stellar dynamics . . . 4
  - 1.1.2 Radio and X-ray emission from SgrA* . . . 6
  - 1.1.3 Near infrared emission from SgrA* . . . 6
- 1.2 Flare-models . . . 7
  - 1.2.1 Star-disk interactions . . . 7
  - 1.2.2 Jet-model . . . 8
  - 1.2.3 Orbiting hot spot model . . . 8

2 Theoretical background **11**
- 2.1 Foundations of general relativity . . . 11
  - 2.1.1 Equivalence principle . . . 11
  - 2.1.2 From flat to curved spacetime . . . 12
  - 2.1.3 Equations of motion . . . 14
  - 2.1.4 Frequency shift . . . 15
  - 2.1.5 Relativistic beaming . . . 18
  - 2.1.6 Einstein field equation . . . 19
- 2.2 The static black hole . . . 21
  - 2.2.1 Schwarzschild metric . . . 22
  - 2.2.2 Orbital motion . . . 25
- 2.3 The rotating black hole . . . 29
  - 2.3.1 Kerr metric . . . 30
  - 2.3.2 Orbital motion . . . 31

3 Visualization **37**
- 3.1 Concept . . . 37
  - 3.1.1 Conventional ray tracing . . . 37
  - 3.1.2 Ray tracing in special relativity . . . 39
  - 3.1.3 Ray tracing in general relativity . . . 39
- 3.2 Visualization of an orbiting hot spot . . . 41
  - 3.2.1 Setup . . . 41
  - 3.2.2 Data output . . . 43

3.2.3 Simulation parameters 44

4 The code **45**
4.1 Subroutines 45
4.1.1 Simulation initializer 45
4.1.2 Image integrator 46
4.1.3 Photometry and astrometry calculator 48
4.1.4 Movie generator 50
4.2 Model implementation 50
4.2.1 Blob-arc-model 51
4.2.2 Accretion disk 52
4.2.3 Gravitational shear 53
4.2.4 Magnetohydrodynamic shear 55

5 Modeling flares from SgrA* **57**
5.1 Compact blob-model 57
5.1.1 Photometry 57
5.1.2 Astrometry 62
5.1.3 Combination of photometry and astrometry 65
5.1.4 Multiple blobs 66
5.2 Shearing blob-arc-model 68
5.2.1 Photometry 70
5.2.2 Astrometry 72
5.3 Fitting observational data 74
5.3.1 Approach 74
5.3.2 L-band flare from April 4, 2007 75
5.3.3 L-band flare from July 22, 2007 81

6 Analytic approach **86**
6.1 Photometry 87
6.2 Astrometry 90

7 Conclusion **91**

A Fundamental constants and units **93**

B Geometrized unit system **94**

C How to use the code developed in this work **95**
C.1 Processing raw data 95
C.2 Running a simulation 96
C.3 Simulation output 97

Chapter 1

Introduction

The rotational center of our own galaxy, the Milky Way, is briefly called *Galactic Center*. It is located about 26 000 lightyears away from earth in the direction of *Sagittarius*, a constellation in the southern hemisphere of the night sky. It cannot be observed in the visible, ultraviolet or soft X-ray regime due to cool interstellar dust along the line of sight, absorbing all radiation with such wavelengths. The windows allowing observations of the Galactic Center region are located at gamma ray, hard X-ray, infrared, sub-millimeter and radio wavelengths.

The very center of our galaxy coincides with an extended radio source named *Sagittarius A*, containing the compact source *Sagittarius A** (SgrA*). Various indications give rise to the conviction that this source must contain a supermassive black hole. The radiation from SgrA* is presumably generated via accretion of the surrounding gas onto the black hole, producing an extended emission and probably an accretion disk. The latter is too small to be resolved with present instruments, but new concepts in astronomical interferometry may soon lead to observations with high enough precision to observe objects in the black hole's direct vicinity.

1.1 Observations of the Galactic Center

Substantial progress in observational techniques during the past decades provided ever better knowledge of the Galactic Center and its components. In the following, some of the most recent findings are outlined in brief.

1.1.1 Stellar dynamics

For several years the Galactic Center stars have been observed in the near infrared (NIR), providing measurements of their proper motions (see Figure 1.1). The observations clearly show that some stars in the immediate vicinity of SgrA* - i.e. at distances up to about 30 lightdays - move on Keplerian

orbits around a central compact mass distribution. The location of the central object is consistent with the radio-position of SgrA* to high accuracy. From the shape of the orbits, the distance as well as the mass of SgrA* can be determined [12]:

$$D_{\mathrm{SgrA}^\star} = 7.62 \pm 0.32\, kpc \qquad M_{\mathrm{SgrA}^\star} = 3.61 \pm 0.32 \cdot 10^6 M_\odot \tag{1.1}$$

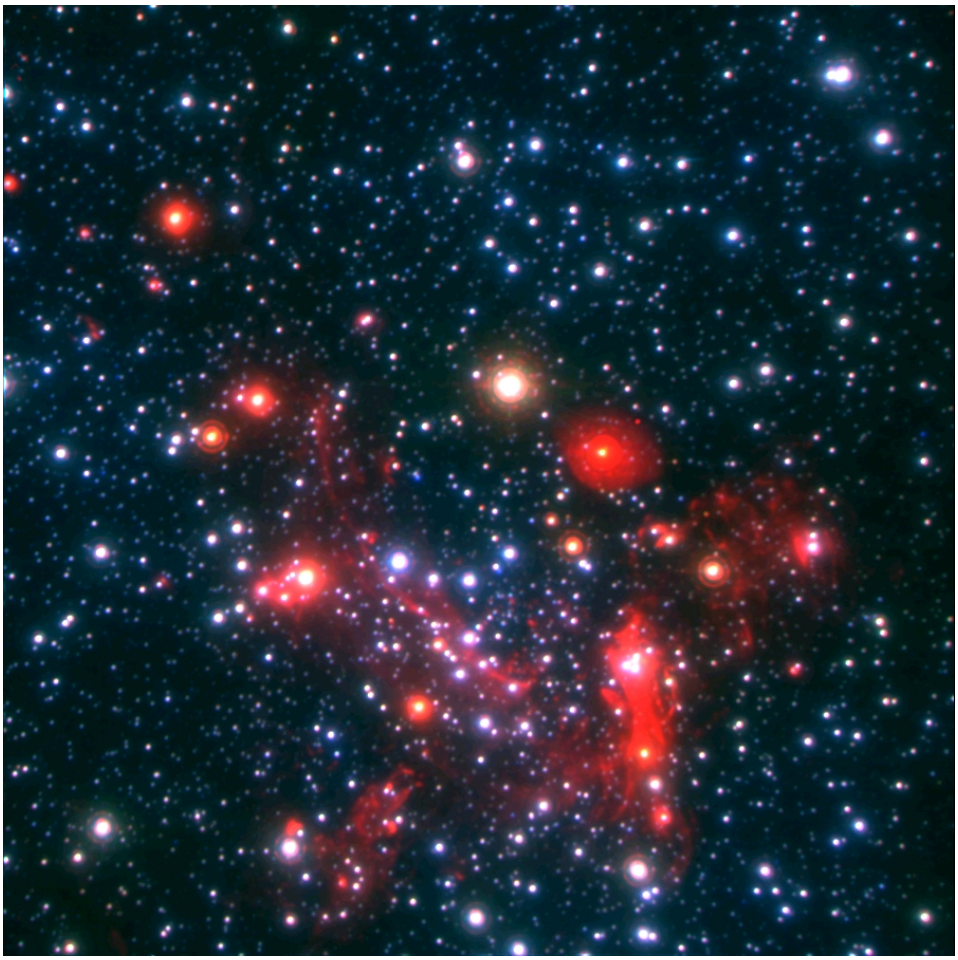

Figure 1.1: Pseudo-color image of the central parsec of the Milky Way in the near infrared (from ESO, MPE).

Since the star *S2* approaches the dynamical center by a distance down to 100AU, the upper limit for the extension of the central object can be estimated by this number. Without any reasonable doubt such a high mass density can only be explained with the occurrence of a supermassive black hole. Its event horizon can be calculated to be roughly $15R_\odot$. This yields an apparent size of about 10μas on sky, the largest of all known black hole candidates.

1.1.2 Radio and X-ray emission from SgrA*

The German X-ray satellite *ROSAT* first detected potential radiation from SgrA* in the 1990's. Later, a more reliable identification of X-rays from this source was possible with *Chandra* and *XMM-Newton* thanks to their high spatial resolution and sensitivity.

While the radio emission of SgrA* only varies slowly on time scales of several to a few hundred days with an amplitude below ten percent, in the X-ray regime it is found to exhibit two different states [10]. On the one hand, weak X-rays are emitted from a slightly extended area around the black hole (quiescent state), suggesting the existence of hot accreting gas in the environment of SgrA*. On the other hand, bright flares show up with a period of about one per day. Then, during several tens of minutes, SgrA* brightens up strongly (up to 100 times as bright as the quiescent state) and a distinctive point source emerges at its location. This radiation must originate from a region within less than 10 Schwarzschild radii of the supermassive black hole because of the short rise- and decay-times of the X-ray flares.

1.1.3 Near infrared emission from SgrA*

In the near infrared regime the Galactic Center can be observed with high angular resolution since the beginning of the 1990's. However, for quite a long time no such radiation has been detected at the location of SgrA*. The first NIR-flare was witnessed during routine observations of the Galactic Center star cluster at the *Very Large Telescope* (VLT) on mount Paranal in Chile on may 9, 2003. Since then many more have been recorded.

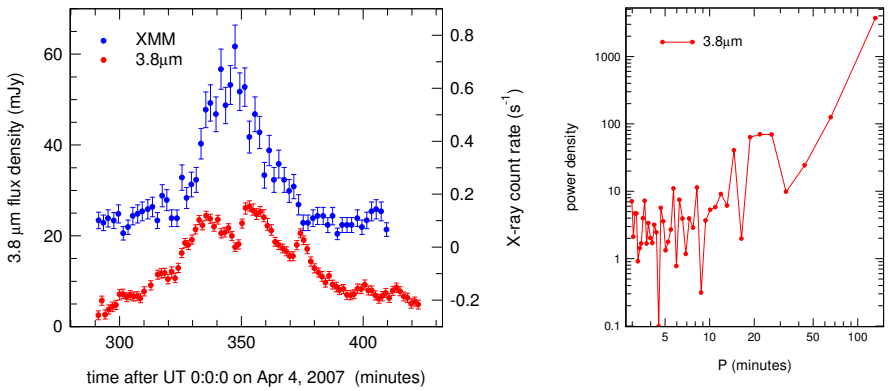

Figure 1.2: Left: SgrA* flare light curves in the NIR (red) and X-ray (blue) from April 4, 2007. Right: Periodogram of the NIR-flare light curve (from MPE).

These flares typically last for several hours and occur a few times per day [40]. Additionally they show brightness variations on smaller timescales

(on the order of 20 minutes), unlike the X-ray flares (see Figure 1.2). Simultaneous multi-wavelength observations of the Galactic Center and SgrA* were carried out from 2004 on. These observations provide the required information to constrain physical models for the origin of the flares. Some of these models will be presented in the following section.

1.2 Flare-models

The emission-process of the NIR-flares from the Galactic Center is still unclear. For this reason, various physical models have been developed trying to explain their origin and to find possible associations concerning the black hole. In the following, three common models are presented in brief.

1.2.1 Star-disk interactions

Nayakshin et al. [30] proposed a model for the origin of the flares from SgrA* in 2003. They argue that the flares are emitted by bow shocks around stars when they pass through an inactive disk around the central black hole. The disk may be a remnant of the past accretion and star formation activity in the Galactic Center and may have a temperature of about 100K and a size of at least 10^4 Schwarzschild radii. They expect a few star-disk crossings per day, in accordance with the observed rate of flaring events. The periodicity in the NIR-flares is thought to be a signature of hydrodynamical oscillations excited in the upper layers of the stars through collision with the disk.

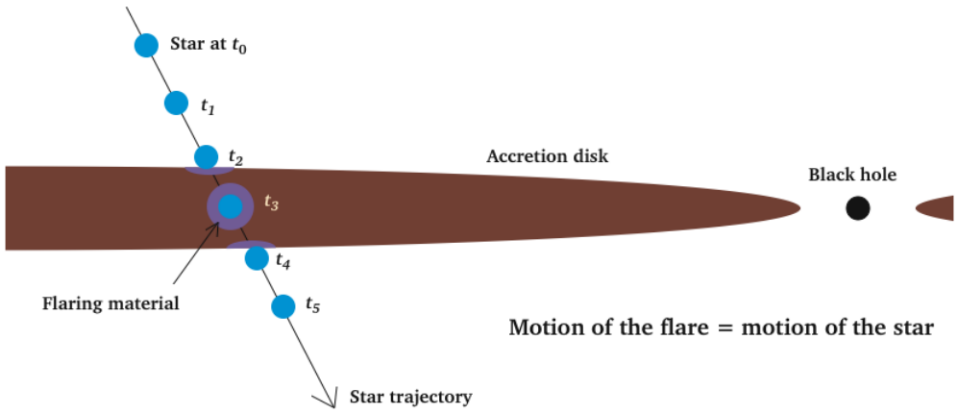

Figure 1.3: Schematic illustration of a star-disk interaction (from [34]).

However, this model seems unlikely, because the discrete periodicity around 20 minutes and the observed red spectrum of the flares is hard to reproduce.

1.2.2 Jet-model

Another approach to modeling the emission process of SgrA* was presented by Markoff et al. [24]. The basic idea is that the radio emission is produced by a supersonic, freely expanding conical jet. On either side of the accretion flow that feeds the jet, a magnetized, relativistic proton and electron plasma is ejected from a nozzle. The jet is interspersed with a tangled magnetic field dominating the internal gas pressure and producing a power law energy distribution of relativistic electrons.

In this model the origin of the flares is described by Markoff et al. via either an increased accretion rate due to clumps of higher density in the accretion flow, or sudden shock-acceleration of the particles due to magnetic reconnection events in the jet. The periodicity in the light curves could come from individual blobs of denser material being ejected at a pseudo-frequency.

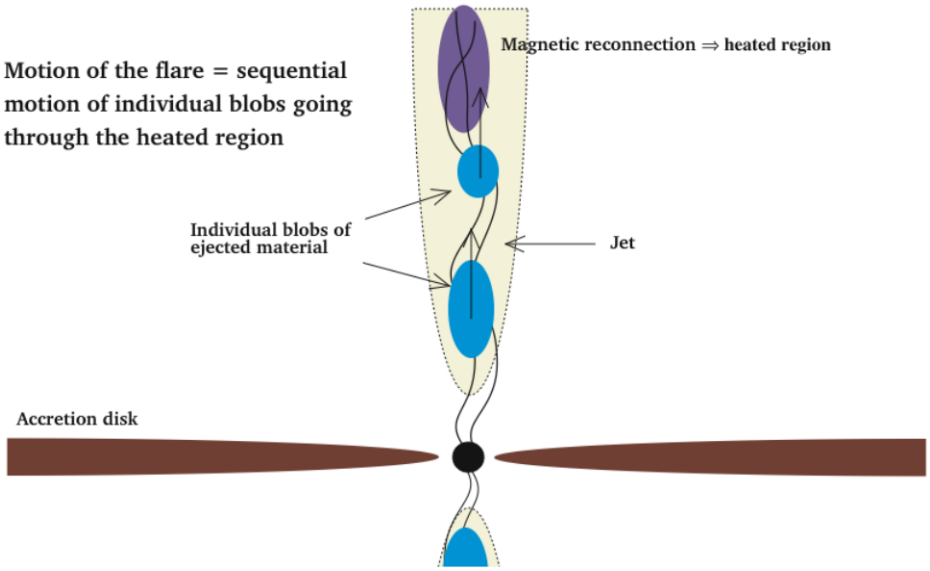

Figure 1.4: Schematic illustration of the jet-model (from [34]).

1.2.3 Orbiting hot spot model

However, many astronomers favor another interpretation for the observed flares. They consider the emission from matter on a close orbit around the central supermassive black hole. This is mainly based on the observed periodicities in the flare light curves that seem to match up with the appropriate orbital period timescales.

It is argued that such a *hot spot* originates from a magnetic reconnection in the highly magnetized plasma of the surrounding accretion disk, similar

to the mechanism responsible for the solar flares (Yuan et al. [43]). In a confined region of space electrons are accelerated to high energies, causing them to spiral around the magnetic field lines and emit synchrotron radiation. This hot spot follows the Keplerian rotation of the accretion flow and completes several orbits around the central black hole until it fades away due to synchrotron-cooling.

The periodic flux-variations in the observed light curves are produced by relativistic effects. That close to the black hole, the orbital motion approaches the speed of light and the curvature of spacetime is non-negligible. Thus, the hot spot's appearance depends on its orbital location and thereby changes periodically with time. This scenario opens up the opportunity to test the laws of general relativity. For example, one can immediately constrain the spin of the black hole knowing both the orbital radius and period of the hot spot ($a = 0.52 M_{\mathrm{SgrA}^\star}$ for the last stable orbit and an orbital period of roughly 17 minutes, as observed in the K-band flare from June 16, 2003 by Genzel et al. [18]).

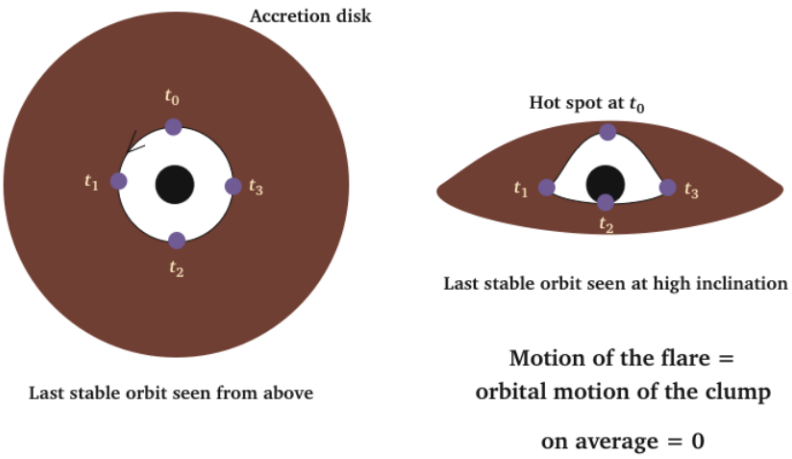

Figure 1.5: Schematic illustration of the orbiting hot spot model (from [34]).

A spatially resolved observation of such a scenario would have tremendous implications on our understanding of fundamental physics, since it provides a laboratory for many higher order general relativistic effects. Although the black hole in the Galactic Center happens to occupy the largest apparent size among all known black hole candidates (a Schwarzschild radius of about 10μas), it has not been possible to resolve it with present instruments yet.

In principle, radio-interferometry can reach such high resolutions, but due to scattering effects, images are blurred. With shorter wavelengths, the

scattering gets weaker. In the NIR one can neglect it, but the challenge in this regime is to build an interferometer that combines light rays from several big telescope-mirrors in a coherent way. This means the whole system has to be stable on scales of micrometers in order to see the desired interference patterns, or *fringes*, as they are called among interferometrists.

Currently there are various attempts to build such an instrument. The *Phase-Referenced Imaging and Micro-arcsecond Astrometry* (PRIMA) instrument for the Very Large Telescope in Chile is currently being developed by the *European Southern Observatory* (ESO). The objective of PRIMA is to enable simultaneous interferometric observations of two objects using two telescope-mirrors (one baseline).

The *Max Planck Institute for Extraterrestrial Physics* (MPE) aims at an even more ambitious goal. Their adaptive optics assisted instrument for precision narrow-angle astrometry and interferometric phase-referenced imaging, labeled GRAVITY [11], intends to combine the four 8-meter unit telescopes at the VLT interferometrically (see Figure 1.6). With its six baselines it is intended to resolve centroid-motions in two dimensions with a resolution of 10μas. However, the development of this instrument is still in an early stage and will probably take around five years from now to be completed.

Figure 1.6: The Very Large Telescope on mount Paranal in Chile. The white lines indicate light rays from each telescope that are combined in the laboratory (from ESO).

Chapter 2

Theoretical background

"*I want to know God's thoughts, the rest are details.*"

Albert Einstein (1879-1955)

In order to describe phenomena dealing with matter in the direct vicinity of extremely high mass densities like black holes, one has to employ the full machinery of general relativity. The most prominent among them are:

- Bending of light rays
- Frequency shift
- Relativistic beaming
- Perihelion shift
- Frame dragging

Beginning with some basic assumptions of general relativity, further aspects of black hole physics will be discussed below. This digression into theory will introduce all the physical quantities used in the simulations.

2.1 Foundations of general relativity

2.1.1 Equivalence principle

Einstein's most important assumption for the development of general relativity was the equivalence principle:

"*In a local free falling frame of reference all gravitational forces vanish and the laws of special relativity hold.*"

Stated from a more experimental point of view:

"*Gravitational mass equals inertial mass.*"

or equivalently:

"*There is no difference between gravitational and inertial forces.*"

While Newton's theory of gravitation sees this fact as a coincidence, Einstein postulated it as an axiom. Until today, all experiments trying to measure a difference between gravitational and inertial mass confirmed the equivalence principle with accuracies up to $4 \cdot 10^{-13}$ [28].

2.1.2 From flat to curved spacetime

Special relativity states that all inertial frames of reference are equal. Via Lorentz-transformation one can switch in between them by applying a linear transformation on the coordinates

$$x^\alpha \equiv (x^0, x^1, x^2, x^3) \equiv (ct, -x_1, -x_2, -x_3) \tag{2.1}$$

with a rotation-matrix Λ^α_β and a translation a^α

$$\tilde{x}^\alpha = \Lambda^\alpha_\beta x^\beta + a^\alpha \tag{2.2}$$

The second statement of special relativity assumes a constant velocity of light whatever the inertial frame of reference

$$c = \text{const.} \tag{2.3}$$

Any distance in spacetime is expressed through infinitesimal displacements of two *events* via

$$ds = \sqrt{c^2dt^2 - dx_1^2 - dx_2^2 - dx_3^2} \tag{2.4}$$

This can be expressed in an even shorter way by defining the so called *Minkowski-tensor*

$$ds^2 = \eta_{\alpha\beta} dx^\alpha dx^\beta \qquad \text{with} \qquad \eta_{\alpha\beta} = \begin{pmatrix} 1 & 0 & 0 & 0 \\ 0 & -1 & 0 & 0 \\ 0 & 0 & -1 & 0 \\ 0 & 0 & 0 & -1 \end{pmatrix} \tag{2.5}$$

In relativistic theory one often applies Einstein's summation convention, i.e. two identical indices in one upper and one lower position indicate a sum over all their possible values (here: 0,1,2,3). Because the speed of light is constant, the infinitesimal displacement in one inertial frame of reference has to be equal in any other inertial frame of reference:

$$d\tilde{s}^2 \stackrel{!}{=} ds^2 \tag{2.6}$$

This imposes conditions on the transformation matrix Λ^α_β in equation (2.2):

$$d\tilde{s}^2 = \eta_{\alpha\beta} d\tilde{x}^\alpha d\tilde{x}^\beta = \eta_{\alpha\beta}\Lambda^\alpha_\gamma \Lambda^\beta_\delta dx^\gamma dx^\delta = \eta_{\gamma\delta} dx^\gamma dx^\delta = ds^2 \tag{2.7}$$

$$\Lambda^\alpha_\gamma \Lambda^\beta_\delta \eta_{\alpha\beta} = \eta_{\gamma\delta} \tag{2.8}$$

This is a linear system of equations which completely determines Λ for a particular Lorentz-transformation. For instance, an x-boost from one inertial frame of reference at rest in the origin to another one with relative velocity $\mathbf{v} = (v, 0, 0)$, passing the origin at $t = 0$, yields

$$\Lambda^\alpha_\beta = \begin{pmatrix} \gamma & -\gamma\beta & 0 & 0 \\ -\gamma\beta & \gamma & 0 & 0 \\ 0 & 0 & 1 & 0 \\ 0 & 0 & 0 & 1 \end{pmatrix} \tag{2.9}$$

with

$$\gamma := \frac{1}{\sqrt{1-\beta^2}} \quad , \quad \beta := \frac{v}{c} \tag{2.10}$$

and consequently

$$\tilde{x}_1 = \gamma(x_1 - vt), \qquad \tilde{x}_2 = x_2, \qquad \tilde{x}_3 = x_3, \qquad \tilde{t} = \gamma(t - x_1 \frac{v}{c^2}) \tag{2.11}$$

With these basic principles one can derive all the essential formulae in special relativity, including Einstein's famous $E = mc^2$, time dilation and length contraction.

Now consider the case of accelerated motion. Accelerated frames always cause fictitious forces which you won't be able to eliminate, whichever inertial frame of reference you choose. A rotating frame of reference causes centrifugal forces, for instance. Therefore one has to consider the most general transformation of coordinates

$$x^\alpha(\tilde{x}^\nu) = x^\alpha(\tilde{x}^0, \tilde{x}^1, \tilde{x}^2, \tilde{x}^3) \tag{2.12}$$

with x^α being coordinates of an inertial frame of reference and $\tilde{x}^\nu$ those of an arbitrary one. For the infinitesimal displacement of two events in spacetime one obtains

$$ds^2 = \eta_{\alpha\beta} dx^\alpha dx^\beta = \eta_{\alpha\beta} \frac{\partial x^\alpha}{\partial \tilde{x}^\mu} \frac{\partial x^\beta}{\partial \tilde{x}^\nu} d\tilde{x}^\mu d\tilde{x}^\nu \equiv g_{\mu\nu}(\tilde{x}) d\tilde{x}^\mu d\tilde{x}^\nu \tag{2.13}$$

with

$$g_{\mu\nu}(\tilde{x}) := \eta_{\alpha\beta} \frac{\partial x^\alpha}{\partial \tilde{x}^\mu} \frac{\partial x^\beta}{\partial \tilde{x}^\nu} \tag{2.14}$$

called the *metric tensor* of the particular frame of reference. The important difference to the Minkowski-tensor is the dependence on the coordinates.

With the equivalence principle, the meaning of the metric tensor becomes evident. The coordinate transformations which define the metric tensor may eliminate all inertial (fictitious) forces. But as these are equivalent to gravitational forces, $g_{\mu\nu}$ is also connected to the gravitational potential. Moreover from equation (2.13) one can interpret $g_{\mu\nu}$ as a quantity that determines the shape or curvature of spacetime, since it is responsible for the length of any separation between two events. Actually this is the reason why it is called *metric* tensor.

2.1.3 Equations of motion

Test particle

Consider a local frame of reference in free fall, a satellite lab orbiting earth, for instance. The equivalence principle states that the laws of special relativity may be applied. This yields the following equation of motion for a test particle with coordinates ξ^α and proper time τ:

$$\frac{d^2\xi^\alpha}{d\tau^2} = 0 \tag{2.15}$$

The proper time is the time measured in the test particle's frame of reference and is computed via

$$d\tau^2 = \frac{ds^2}{c^2} = \frac{1}{c^2}\eta_{\alpha\beta}d\xi^\alpha d\xi^\beta \tag{2.16}$$

Integration of equation (2.15) yields a straight line in spacetime

$$\xi^\alpha = a^\alpha\tau + b^\alpha \tag{2.17}$$

where a^α and b^α are determined from the boundary conditions. If we now consider an arbitrary frame of reference with coordinates x^μ and metric $g_{\mu\nu}(x)$, the infinitesimal displacement $ds^2 = g_{\mu\nu}(x)dx^\mu dx^\nu$ can be transformed locally to the form of equation (2.16) at each coordinate x. That means for every point in spacetime there is a coordinate transformation $\xi^\alpha(x) = \xi^\alpha(x^0, x^1, x^2, x^3)$ between ξ^α and x^μ. Plugging this transformation into equation (2.15) yields:

$$\frac{d^2\xi^\alpha}{d\tau^2} = \frac{d}{d\tau}\left(\frac{\partial\xi^\alpha}{\partial x^\mu}\frac{dx^\mu}{d\tau}\right) = \frac{\partial\xi^\alpha}{\partial x^\mu}\frac{d^2x^\mu}{d\tau^2} + \frac{\partial^2\xi^\alpha}{\partial x^\mu\partial x^\nu}\frac{dx^\mu}{d\tau}\frac{dx^\nu}{d\tau} = 0 \tag{2.18}$$

Multiplication with $\frac{\partial x^\kappa}{\partial\xi^\alpha}$ and using $\frac{\partial\xi^\alpha}{\partial x^\mu}\frac{\partial x^\kappa}{\partial\xi^\alpha} = \delta^\kappa_\mu$ one can solve for $\frac{d^2x^\kappa}{d\tau^2}$:

$$\frac{d^2x^\kappa}{d\tau^2} = -\Gamma^\kappa_{\mu\nu}\frac{dx^\mu}{d\tau}\frac{dx^\nu}{d\tau} \tag{2.19}$$

where

$$\Gamma^{\kappa}_{\mu\nu} := \frac{\partial x^{\kappa}}{\partial \xi^{\alpha}} \frac{\partial^2 \xi^{\alpha}}{\partial x^{\mu} \partial x^{\nu}} \tag{2.20}$$

is referred to as *Christoffel symbol*. It can also be expressed through first derivatives of the metric tensor:

$$\Gamma^{\kappa}_{\lambda\mu} = \frac{g^{\kappa\nu}}{2} \left(\frac{\partial g_{\mu\nu}}{\partial x^{\lambda}} + \frac{\partial g_{\lambda\nu}}{\partial x^{\mu}} - \frac{\partial g_{\mu\lambda}}{\partial x^{\nu}} \right) \tag{2.21}$$

Equation (2.19) is the desired equation of motion for a test particle in a gravitational field. Because of equations (2.13) and (2.16) there is another condition for the 4-velocity $u^{\mu} := \frac{dx^{\mu}}{d\tau}$:

$$g_{\mu\nu} u^{\mu} u^{\nu} = c^2 \tag{2.22}$$

Photon

According to the equivalence principle, light moves on a straight line, when observed from a local inertial frame of reference. Hence, the motion of a photon can also be described by equations (2.15) or (2.17). But here, τ may not be identified with proper time, because for light we have $ds = d\tau = 0$ (*lightlike* distance). Instead, let us introduce a path parameter λ, such that

$$\frac{d^2 \xi^{\alpha}}{d\lambda^2} = 0 \tag{2.23}$$

One has to assume here, that the photon's wavelength is much smaller than the distance of a significant change in gravitational field strength. The same steps like above lead to the equation of motion for a photon:

$$\frac{d^2 x^{\kappa}}{d\lambda^2} = -\Gamma^{\kappa}_{\mu\nu} \frac{dx^{\mu}}{d\lambda} \frac{dx^{\nu}}{d\lambda} \tag{2.24}$$

Because of $d\tau = 0$ we additionally have:

$$g_{\mu\nu} \frac{dx^{\mu}}{d\lambda} \frac{dx^{\nu}}{d\lambda} = 0 \tag{2.25}$$

The solutions to equations (2.19) and (2.24) are called *geodesics*, they are the shortest possible connections between two events in curved spacetime. In particular, solutions to equation (2.24) are labeled *null geodesics*, referring to the fact that $ds = 0$.

2.1.4 Frequency shift

Because the advance of time differs from one frame of reference to another due to different local gravitational field strengths and relative motions, the

frequency of radiation is also influenced by gravitation. The time τ displayed on a clock in an arbitrary frame of reference is determined by

$$d\tau = \frac{ds_{\text{clock}}}{c} = \frac{1}{c}\left(\sqrt{g_{\mu\nu}(x)dx^\mu dx^\nu}\right)_{\text{clock}} \tag{2.26}$$

In case there is no gravitational field, we can choose an inertial frame of reference and use the Minkowski-tensor. For a constantly moving clock we use $dx^\alpha = (c, \mathbf{v})dt$ and get:

$$d\tau = \frac{1}{c}\left(\sqrt{\eta_{\alpha\beta}dx^\alpha dx^\beta}\right)_{\text{clock}} = \sqrt{1 - \frac{\mathbf{v}^2}{c^2}}\, dt = \gamma^{-1}dt \tag{2.27}$$

Here, the coordinate t is displayed by a clock resting in the inertial frame of reference. Clocks in relative motion to this frame run slower, which is known as *relativistic time dilation*.

Suppose a resting observer measures the time dt between two crests of the light wave emitted by a source in relative motion to him. The wavefront travels with the speed of light c, while the source moves with the relative velocity $v\cos\vartheta$ towards the observer. ϑ is the angle between the velocity vector $\mathbf{v}$ of length v and the line of sight between source and observer (it is 0 for approaching and π for receding sources). Since the second crest is emitted closer or farther from the observer than the first one by a distance of $v\cos\vartheta\, d\tau$ and time dilation stretches the emitted time interval by a factor of γ, he gets:

$$dt = \gamma\left(d\tau - \frac{v\cos\vartheta\, d\tau}{c}\right) = \frac{1 - \beta\cos\vartheta}{\sqrt{1-\beta^2}}d\tau \tag{2.28}$$

where $d\tau$ is the time between two crests, measured in the source's frame of reference. The corresponding frequencies are the reciprocal expressions ('o' for observer and 's' for source):

$$\frac{1}{\nu_o} = \frac{1 - \beta\cos\vartheta}{\sqrt{1-\beta^2}}\frac{1}{\nu_s} \tag{2.29}$$

This behavior is referred to as *relativistic Doppler effect*. The ratio of the two frequencies is a measure of the relative velocity and is denoted by *Doppler factor* z_D

$$z_D := \frac{\nu_o}{\nu_s} = \frac{\sqrt{1-\beta^2}}{1 - \beta\cos\vartheta} \tag{2.30}$$

Another special case is the one of a resting clock in a nonzero gravitational field. Here we have $dx^1 = dx^2 = dx^3 = 0$ and consequently

$$d\tau = \sqrt{g_{00}(x)}\, dt \tag{2.31}$$

If we consider a static gravitational potential, the metric tensor only depends on spatial coordinates denoted by the vector $\mathbf{r}$. Let $\mathbf{r}_s$ be the location of a resting source of monochromatic electromagnetic radiation and $\mathbf{r}_o$ the location of a resting observer. The clocks at these locations show the proper times

$$d\tau_s = \sqrt{g_{00}(\mathbf{r}_s)}\, dt \quad , \quad d\tau_o = \sqrt{g_{00}(\mathbf{r}_o)}\, dt \tag{2.32}$$

If $d\tau_s$ and $d\tau_o$ are chosen to be the time intervals between two successive maxima of the electromagnetic wave, the corresponding frequencies are

$$\nu_s = \frac{1}{d\tau_s} \quad , \quad \nu_o = \frac{1}{d\tau_o} \tag{2.33}$$

A commonly used expression to describe the frequency shift caused by gravitation is the so called *gravitational redshift parameter* z_G, defined as

$$z_G := \frac{\nu_o}{\nu_s} = \sqrt{\frac{g_{00}(\mathbf{r}_s)}{g_{00}(\mathbf{r}_o)}} \tag{2.34}$$

In general, frequency shifts caused by time dilation and gravitation occur simultaneously. For instance, a photon emitted by an approaching massless body appears blueshifted to the observer, a photon emitted by a resting massive body appears redshifted.

There is even a third effect leading to frequency shifts of radiation, namely the so called *cosmological redshift*. It is due to the expansion of the universe, described by a time dependent metric of the form

$$ds^2 = c^2 dt^2 - a(t)^2 \left(\frac{dr^2}{1 - kr^2} + r^2 \left(d\theta^2 + \sin^2 \theta \, d\phi^2 \right) \right) \tag{2.35}$$

It is an exact solution of the Einstein field equation and was found by Friedmann, Lemaître, Robertson and Walker. The *scale factor* $a(t)$ determines the distance between two points with fixed coordinates. The parameter k describes the particular geometry of space that provides both homogeneity and isotropy. There are three possibilities: flat ($k = 0$), spherical ($k = +1$) or hyperbolic ($k = -1$). The expansion causes a redshift of light observed in any direction. The *cosmological redshift parameter* z_C is defined as the ratio between the observed redshift of a certain wavelength and the emitted wavelength. It can also be expressed via the corresponding scale factors

$$z_C := \frac{\lambda_o - \lambda_s}{\lambda_s} = \frac{\lambda_o}{\lambda_s} - 1 = \frac{\nu_s}{\nu_o} - 1 \equiv \frac{a(t_o)}{a(t_s)} - 1 \tag{2.36}$$

Since the expansion proceeds slowly, significant redshift can only be observed in extragalactic distances. It does not play a role in Galactic astronomy.

2.1.5 Relativistic beaming

Not just the frequency, but also the intensity of radiation is affected by gravitation. Qualitatively this can be understood by relativistic aberration: Photons emitted by an approaching object that moves close to the speed of light will appear to be emitted in a cone around the direction of motion. When viewed along this direction, the object appears brighter. In a more quantitative manner this phenomenon is based on *Liouville's theorem in curved spacetime*:

> "*The phase space volume V occupied by a given set of N identical particles is independent of location along the world line of the set.*"

In short:

$$\frac{dV}{d\lambda} = 0 \tag{2.37}$$

with λ being the path parameter along the central geodesic of the swarm. More convenient for applications is the *number density in phase space* or *distribution function* in the neighborhood of one of these particles:

$$n := \frac{N}{V} \tag{2.38}$$

It depends on the location x^μ in spacetime and the 4-momentum p^μ of the particle in whose neighborhood the measurements are made. The conservation law along a particle's trajectory in phase space is called the *collisionless Boltzmann equation* or the *kinetic equation*:

$$\frac{dn(x^\mu(\lambda), p^\mu(\lambda))}{d\lambda} = 0 \tag{2.39}$$

When discussing photons one usually does not think in terms of the number density in phase space. Rather, one speaks of the *specific intensity* I_ν of radiation at a given frequency ν, flowing in a given direction $\mathbf{n}$, as measured in a specified local Lorentz frame. It is defined via the energy dE within a frequency interval $d\nu$ crossing an area dA in a time dt and a solid angle $d\Omega$:

$$I_\nu := \frac{dE}{dt\, dA\, d\nu\, d\Omega} \tag{2.40}$$

Let us therefore express the number density of photons in phase space in terms of the specific intensity. In a time dt, dN photons travel a distance $c\,dt$ through an area dA. Their spatial volume is thus $V_x = c\,dt\,dA$ and their momentum volume is $V_p = (p^0)^2 dp^0 d\Omega$ with $p^0 = E/c$. Hence, their number density is

$$n = \frac{dN}{V_x V_p} = \frac{c^2 dN}{dt\, dA\, E^2 dE\, d\Omega} \tag{2.41}$$

According to Planck's postulate, a photon's energy is proportional to its frequency by *Planck's constant* h:

$$E_{\text{photon}} = h\nu \quad , \quad dE = h\nu \, dN \tag{2.42}$$

Using this yields:

$$n = \frac{c^2 dN}{dt \, dA \, h^3\nu^2 d\nu \, d\Omega} = \frac{c^2 h\nu \, dN}{dt \, dA \, d\nu \, d\Omega \, h^4\nu^3} = \frac{c^2}{h^4}\left(\frac{I_\nu}{\nu^3}\right) \equiv \text{const.} \tag{2.43}$$

Thus, if two observers at different events in spacetime receive the same set of photons, they will see different frequencies ν and different intensities I_ν, but they will obtain identical values for the ratio I_ν/ν^3. This ratio is a so called *Lorentz invariant* in general relativity. From the relativistic Doppler effect we know that approaching light sources appear blueshifted while receding ones appear redshifted. In order to keep the ratio constant, the specific intensity has to increase and decrease respectively.

2.1.6 Einstein field equation

In order to describe spacetime around arbitrary mass distributions one has to solve one of Einstein's most famous formulae, his field equation. This equation states another fundamental law of nature, which was beautifully put in words by John Archibald Wheeler:

> "*Matter dictates spacetime how to curve, in turn, spacetime dictates matter how to move.*"

In the form of a mathematical equation it is expressed as

$$R_{\mu\nu} - \frac{R}{2} g_{\mu\nu} = -\frac{8\pi G}{c^4} T_{\mu\nu} \tag{2.44}$$

Instead of a detailed mathematical derivation, the main components of this equation will be outlined in brief in the following subsections.

Ricci tensor

The quantity $R_{\mu\nu}$ in equation (2.44) is known as the *Ricci tensor*. It is defined via the *Riemann curvature tensor* and the metric tensor:

$$R_{\mu\nu} = g^{\kappa\rho} R_{\kappa\mu\rho\nu} \tag{2.45}$$

The Riemann curvature tensor can be expressed as

$$R^{\rho}{}_{\mu\lambda\nu} = \frac{\partial \Gamma^{\rho}_{\mu\lambda}}{\partial x^\nu} - \frac{\partial \Gamma^{\rho}_{\mu\nu}}{\partial x^\lambda} + \Gamma^{\sigma}_{\mu\lambda}\Gamma^{\rho}_{\sigma\nu} - \Gamma^{\sigma}_{\mu\nu}\Gamma^{\rho}_{\sigma\lambda} \tag{2.46}$$

This tensor quantitatively describes the curvature of four-dimensional spacetime. If it is zero, spacetime is flat and can be described via Cartesian coordinates. However, this is no longer possible if any component of $R^{\rho}{}_{\mu\lambda\nu}$ is nonzero. Because of symmetry properties it has only twenty independent components. Contraction (i.e. summing over two equal indices) of the Riemann curvature tensor leads to the Ricci tensor:

$$R^{\rho}{}_{\mu\rho\nu} = R_{\mu\nu} \tag{2.47}$$

Another contraction leads to the *scalar curvature* R:

$$R^{\mu}{}_{\mu} = R \tag{2.48}$$

Stress-energy tensor

The stress-energy tensor $T_{\mu\nu}$ is a quantity that describes the density and flux of energy and momentum in spacetime, generalizing the stress tensor of Newtonian physics. It is the source of the gravitational field in general relativity, just as matter is the source of such a field in Newtonian gravity. In principle, all predominant forms of energy and momentum are contained within this tensor. These include kinetic and electromagnetic contributions as well as mass density and pressure, for instance.

One example for the stress-energy tensor is that of an ideal fluid. An ideal fluid is seen as a physical system, described through a mass density $\rho(\mathbf{r}, t)$, a velocity field $\mathbf{v}(\mathbf{r}, t)$ and an isotropic pressure $P(\mathbf{r}, t)$. Viscosity (inner friction) is not considered. Applying Newton's laws to these quantities yields the most important equations of hydrodynamics, namely Euler's equation and the continuity equation, which states the conservation of mass:

$$\rho \left(\frac{\partial \mathbf{v}}{\partial t} + (\mathbf{v} \cdot \nabla) \mathbf{v} \right) = -\nabla P \tag{2.49}$$

$$\frac{\partial \rho}{\partial t} + \nabla \cdot (\rho \mathbf{v}) = 0 \tag{2.50}$$

For a special relativistic treatment of these formulae one has to replace the velocity field $\mathbf{v}(\mathbf{r}, t)$ by the Lorentz vector field $u^{\alpha}(x)$ and calculate the Lorentz transformed mass density and pressure. The generalized version of the above equations then has to be covariant under Lorentz transformation and reduce to the original form for $v \ll c$. It then simply reads:

$$\partial_{\beta} T^{\alpha\beta} = 0 \tag{2.51}$$

with

$$T^{\alpha\beta} = \left(\rho + \frac{P}{c^2} \right) u^{\alpha} u^{\beta} - \eta^{\alpha\beta} P \tag{2.52}$$

In general relativity, the Minkowski coordinates x^α are then replaced by curvilinear coordinates x^μ:

$$T^{\mu\nu} = \left(\rho + \frac{P}{c^2}\right) u^\mu u^\nu - g^{\mu\nu} P \tag{2.53}$$

From equation (2.53) it is obvious, that $T^{\mu\nu}$ is symmetric. Additionally, $T^{\mu\nu}$ may contain yet other forms of energy, such as electromagnetic contributions.

Coming back to the Einstein field equation now, we can gain a little more insight into its structure. Since $R_{\mu\nu}$, $T_{\mu\nu}$ as well as $g_{\mu\nu}$ are symmetric tensors with hence ten independent components, the Einstein field equation actually consists of ten algebraic equations. But due to equation (2.51), only $10 - 4 = 6$ of them are effectively independent. This indeterminacy of $g_{\mu\nu}$ can be unraveled by imposing a gauge condition. If $g_{\mu\nu}(x)$ is a solution of (2.44), a coordinate transformation $x^\mu \to \tilde{x}^\mu$ provides another solution $g'_{\mu\nu}(\tilde{x})$. Since a coordinate transformation corresponds to four equations, the field equations may only fix six components.

The possibility to choose any coordinate transformation offers the freedom of gauge. A particular gauge may be used in order to ease the solution of a certain problem. This invariance of physical laws under arbitrary coordinate transformations is referred to as the *principle of covariance* in general relativity.

Another common form of the Einstein field equation can be obtained by contraction of equation (2.44):

$$R^\mu{}_\mu - \frac{R}{2}\delta^\mu_\mu = R - 4\frac{R}{2} = -R = -\frac{8\pi G}{c^4} T^\mu{}_\mu \equiv -\frac{8\pi G}{c^4} T \tag{2.54}$$

and by replacing the scalar curvature R by $8\pi GT/c^4$:

$$R_{\mu\nu} = -\frac{8\pi G}{c^4}\left(T_{\mu\nu} - \frac{T}{2} g_{\mu\nu}\right) \tag{2.55}$$

2.2 The static black hole

> "*Black holes are the most perfect macroscopic objects there are in the universe: the only elements in their construction are our concepts of space and time.*"
>
> Subrahmanyan Chandrasekhar (1910-1995)

Black holes are created when a massive object like the sun is compressed to a sphere with a radius of three kilometers, thereby creating such strong

spacetime curvatures that it can no longer communicate with the external universe. In particular no light may escape from its surface or below it.

However, our sun won't evolve into a black hole, because its self gravitation will be too low to overcome its electron degeneracy pressure in the white dwarf stage. Nevertheless, very massive stars may form neutron stars or even black holes if they evolve a nonrotating mass of more than 1.44 solar masses in the degenerate state. This mass limit is designated as *Chandrasekhar limit* in recognition of its discoverer. There are also other possible formation scenarios:

- Accretion of matter from a companion in a binary system
- Merging of a whole star cluster into a supermassive black hole
- Perturbations in the initial density distribution of the expanding universe (*primordial black holes*)

But what is the *surface* of a black hole in particular and how is its environment influenced by it? In the following subsections these issues will be investigated further.

2.2.1 Schwarzschild metric

Consider a static spherical massive body with radius r_0 and mass M. If we want to know the metric surrounding it, we have to solve the Einstein field equation in that region. But before doing so, a preliminary design of the metric tensor can be made by exploiting symmetry and boundary conditions. Because of spherical symmetry, spherical coordinates $x^\mu = (ct, -r, -\theta, -\phi)$ with

$$dx^\mu = (cdt, -dr, -rd\theta, -r\sin\theta d\phi) \tag{2.56}$$

make the calculations easiest. In the limit $r \to \infty$ the metric should reduce to the Minkowski-metric of empty space:

$$ds^2 = \eta_{\mu\nu} dx^\mu dx^\nu = c^2dt^2 - dr^2 - r^2\left(d\theta^2 + \sin^2\theta\, d\phi^2\right) \tag{2.57}$$

In the closer region of the object's gravitational field additional coefficients appear, denoted by A, B and C:

$$ds^2 = B(r)c^2dt^2 - A(r)dr^2 - C(r)r^2\left(d\theta^2 + \sin^2\theta\, d\phi^2\right) \tag{2.58}$$

Due to the assumed isotropy and time independence, these coefficients cannot depend on θ, ϕ or t. Linear terms in $d\theta$ or $d\phi$ cannot exist, since they would also violate isotropy. A possible coefficient of the form $D(r)drdt$ may be eliminated by introducing a new time variable $t \to t + \Psi(r)$, which does not change the physical properties of the metric because of gauge freedom. The same holds for the radial coordinate r, so $C(r)$ may as well be set to 1.

This general ansatz for an isotropic and statical metric is a *standard form* for various problems. From the boundary condition (2.57) the two remaining coefficients have to fulfill

$$A(r), B(r) \overset{r\to\infty}{\longrightarrow} 1 \tag{2.59}$$

Unlike the angular coordinates θ and ϕ, which have the same meaning as in Minkowski spacetime, t and r are the coordinates displayed by a clock and a ruler in infinite distance.

The metric tensor can now be written as:

$$g_{\mu\nu} = \begin{pmatrix} B(r) & 0 & 0 & 0 \\ 0 & -A(r) & 0 & 0 \\ 0 & 0 & -r^2 & 0 \\ 0 & 0 & 0 & -r^2\sin^2\theta \end{pmatrix} \tag{2.60}$$

With it we can solve the Einstein field equation outside the massive body and get expressions for A and B. Since the stress-energy tensor is zero in the region under consideration, the field equation (2.55) reduces to the so called *vacuum field equation*

$$R_{\mu\nu} = 0 \qquad (r \geq r_0) \tag{2.61}$$

No source field explicitly appears in it, but the above assumptions for the matter distribution already influenced the shape of the metric tensor.

The proceeding is straight forward. The Ricci tensor is defined via Christoffel symbols, which can be seen from equation (2.46):

$$R_{\mu\nu} = \frac{\partial\Gamma^\rho_{\mu\rho}}{\partial x^\nu} - \frac{\partial\Gamma^\rho_{\mu\nu}}{\partial x^\rho} + \Gamma^\sigma_{\mu\rho}\Gamma^\rho_{\sigma\nu} - \Gamma^\sigma_{\mu\nu}\Gamma^\rho_{\sigma\rho} \tag{2.62}$$

These can then be calculated from the metric tensor (equation (2.21)), given by the ansatz (2.60). After some cumbersome calculations one finally ends up with:

$$R_{00} = -\frac{B''}{2A} + \frac{B'}{4A}\left(\frac{A'}{A} + \frac{B'}{B}\right) - \frac{B'}{rA} \tag{2.63}$$

$$R_{11} = \frac{B''}{2B} - \frac{B'}{4B}\left(\frac{A'}{A} + \frac{B'}{B}\right) - \frac{A'}{rA} \tag{2.64}$$

$$R_{22} = -1 - \frac{r}{2A}\left(\frac{A'}{A} - \frac{B'}{B}\right) + \frac{1}{A} \tag{2.65}$$

$$R_{33} = R_{22}\sin^2\theta \tag{2.66}$$

$$R_{\mu\nu} = 0 \quad \text{, for } \mu \neq \nu \tag{2.67}$$

where primed quantities denote derivatives with respect to r. Hence, the vacuum field equation is trivially satisfied for $\mu \neq \nu$ and the remaining independent equations are:

$$R_{00} = 0 \quad , \quad R_{11} = 0 \quad , \quad R_{22} = 0 \tag{2.68}$$

Solving these for A and B yields:

$$A(r) = \frac{1}{1 - R_s/r} \quad , \quad B(r) = 1 - \frac{R_s}{r} \tag{2.69}$$

with R_s being a constant of integration. Its magnitude can be determined by comparing B with the Newtonian limit of the metric's first component, which holds for weak gravitational field strengths:

$$B(r) = g_{00} \approx 1 - \frac{2GM}{rc^2} \qquad \left(\frac{GM}{rc^2} \ll 1\right) \tag{2.70}$$

$$\Rightarrow R_s = \frac{2GM}{c^2} \tag{2.71}$$

It is called *Schwarzschild radius*. Just like the *Schwarzschild metric*

$$ds^2 = \left(1 - \frac{R_s}{r}\right) c^2 dt^2 - \left(1 - \frac{R_s}{r}\right)^{-1} dr^2 - r^2 \left(d\theta^2 + \sin^2\theta \, d\phi^2\right) \tag{2.72}$$

it is named after the German physicist and astronomer *Karl Schwarzschild*. Since a resting clock in r displays the time interval

$$d\tau = \sqrt{1 - \frac{R_s}{r}} \, dt \tag{2.73}$$

the time interval dt (measured by a remote observer) becomes infinite at $r = R_s$. This means, a photon emitted from there sustains an infinitely large redshift ($z_G = 0$) and thus is not observable. It also implies that t is no adequate time coordinate for events in the region $r \leq R_s$. An object with radius $r_0 \leq R_s$ is denoted as *black hole*, because no photon may emanate into the outer domain $r > R_s$. The Schwarzschild radius defines the so called *event horizon* of a nonrotating black hole, referring to the fact that any events in spacetime are causally separated by the surface with radius R_s.

The Schwarzschild metric becomes singular at the event horizon, but that does not necessarily imply a singularity of spacetime. A suitable choice of new coordinates may eliminate this singularity (for instance *Eddington-Finkelstein* coordinates). In such a coordinate system the Schwarzschild radius is no designated region anymore; for this reason that kind of singularity is called a *coordinate singularity*.

In contrast to this is the case $r = 0$. The singularity at this point corresponds to a point mass with $r_0 \to 0$ and hence leads to a real physical infinity.

2.2.2 Orbital motion

Having determined the gravitational field of a spherical symmetric object, we can now study the relativistic generalization of the classical Kepler problem, i.e. the movement of a test particle in a central symmetric, static potential well. In general relativity the movement of photons may also be included, since they are deflected by gravitational fields as well.

The starting point is the equation of motion for a test particle (2.19):

$$\frac{d^2x^\kappa}{d\tau^2} = -\Gamma^\kappa_{\mu\nu}\frac{dx^\mu}{d\tau}\frac{dx^\nu}{d\tau}$$

For a photon, τ has to be replaced by the path parameter λ (equation (2.24)). Once again the Christoffel symbols can be calculated from the Schwarzschild metric. The four components of the equation of motion then look like this:

$$\frac{d^2t}{d\tau^2} = -\frac{B'}{B}\frac{dt}{d\tau}\frac{dr}{d\tau} \tag{2.74}$$

$$\frac{d^2r}{d\tau^2} = -\frac{B'c^2}{2A}\left(\frac{dt}{d\tau}\right)^2 - \frac{A'}{2A}\left(\frac{dr}{d\tau}\right)^2 + \frac{r}{A}\left(\frac{d\theta}{d\tau}\right)^2 + \frac{r\sin^2\theta}{A}\left(\frac{d\phi}{d\tau}\right)^2 \tag{2.75}$$

$$\frac{d^2\theta}{d\tau^2} = -\frac{2}{r}\frac{dr}{d\tau}\frac{d\theta}{d\tau} + \sin\theta\cos\theta\left(\frac{d\phi}{d\tau}\right)^2 \tag{2.76}$$

$$\frac{d^2\phi}{d\tau^2} = -\frac{2}{r}\frac{dr}{d\tau}\frac{d\phi}{d\tau} - 2\cot\theta\frac{d\theta}{d\tau}\frac{d\phi}{d\tau} \tag{2.77}$$

With A and B given by (2.69), we further get:

$$c\frac{dt}{d\tau}\left(1-\frac{R_s}{r}\right) = \text{const.} =: \varepsilon \tag{2.78}$$

$$\frac{\varepsilon^2-\kappa}{2} = \frac{1}{2}\left(\frac{dr}{d\tau}\right)^2 - \frac{R_s\kappa}{2r} + \frac{\ell^2}{2r^2} - \frac{R_s\ell^2}{2r^3} \tag{2.79}$$

$$\theta = \frac{\pi}{2} \tag{2.80}$$

$$r^2\frac{d\phi}{d\tau} = \text{const.} =: \ell \tag{2.81}$$

where ε, ℓ and κ are constants of integration. In (2.80) θ is chosen to be $\pi/2$ without loss of generality, since the problem is invariant under arbitrary rotations in space. Equation (2.81) suggests that ℓ is the angular momentum per mass and hence can be interpreted as the angular momentum conservation law. Analogously, conservation of energy per mass is stated by (2.78). κ is determined by the normalization condition for the four-velocity ((2.22) for test particles and (2.25) for photons respectively):

$$\kappa = \begin{cases} c^2 & \text{, if } m \neq 0 \\ 0 & \text{, if } m = 0 \end{cases} \tag{2.82}$$

Lastly, equation (2.79) can be rewritten in the form

$$\frac{1}{2}\left(\frac{dr}{d\tau}\right)^2 + V_{\text{eff}}(r) = \frac{\varepsilon^2 - \kappa}{2} \tag{2.83}$$

with the *effective Potential*

$$V_{\text{eff}}(r) = \begin{cases} -\dfrac{GM}{r} + \dfrac{\ell^2}{2r^2} - \dfrac{GM\ell^2}{c^2 r^3} & \text{, if } m \neq 0 \\ \dfrac{\ell^2}{2r^2} - \dfrac{GM\ell^2}{c^2 r^3} & \text{, if } m = 0 \end{cases} \tag{2.84}$$

The term proportional to $1/r$ corresponds to the attractive Newtonian potential known from classical mechanics, it is not present for photons. The expression scaling with $1/r^2$ is the classical centrifugal barrier, preventing two point masses with nonzero angular momentum from colliding. A new feature in general relativity is the term proportional to $1/r^3$. It dominates at small radii and thus nearby bodies are attracted stronger than in classical mechanics.

The formal solution to the radial equation (2.83) is given by the integral

$$\tau = \pm \int \frac{dr}{\sqrt{\varepsilon^2 - \kappa - 2V_{\text{eff}}(r)}} \tag{2.85}$$

Due to the relativistic term in $V_{\text{eff}}(r)$, it is an elliptic integral which cannot be solved by elementary functions. However, the characteristics of the solutions can be elucidated graphically by plotting $V_{\text{eff}}(r)$ for different values of ℓ:

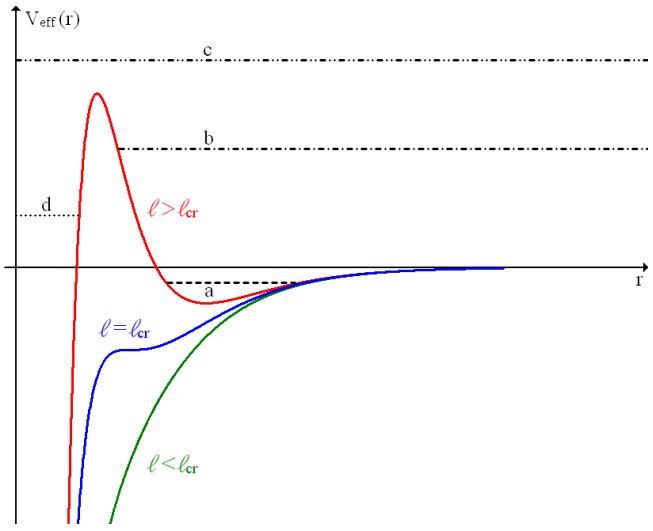

Figure 2.1: Effective potential for test particles with different specific angular momenta in the Schwarzschild metric.

The energy of a moving particle is constant and can be illustrated by a horizontal line. The intersections of this line with the effective potential determine the turning points (see Figure 2.1). There are four different possible trajectories for test particles:

a) Motion in a bound region in space between $r_{\min}$ and $r_{\max}$, analog to the elliptic motion in Newtonian theory. The trajectory is not a conic section and, in general, not closed. This fact is responsible for the so called *perihelion shift* of orbits.

b) A particle from infinity approaches the central body, reaches $r_{\min}$ and moves back to infinity. This trajectory is an analogue of hyperbolic motion in the classical case.

c) The particle falls into the central object, because its energy is higher than the maximum of the effective potential. This type of motion is impossible in Newtonian mechanics and denoted as *gravitational capture*.

d) In the neighborhood of the central body a particle may first recede from the center, reach $r_{\max}$ and then fall back into the center.

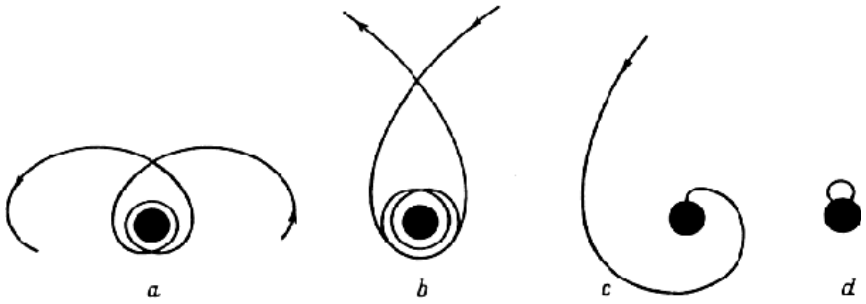

Figure 2.2: Trajectories of test particles in the Schwarzschild metric (from [31]).

For photons, case a) does not exist, because there is no minimum in the effective potential. It does not change qualitatively for different angular momenta due to the appearance of the factor ℓ^2 in every summand (see Figure 2.3).

Circular orbits

A special case of the motion of a test particle in a bound orbit is the circular orbit. It has a constant radius:

$$\frac{dr}{d\tau} = 0 \tag{2.86}$$

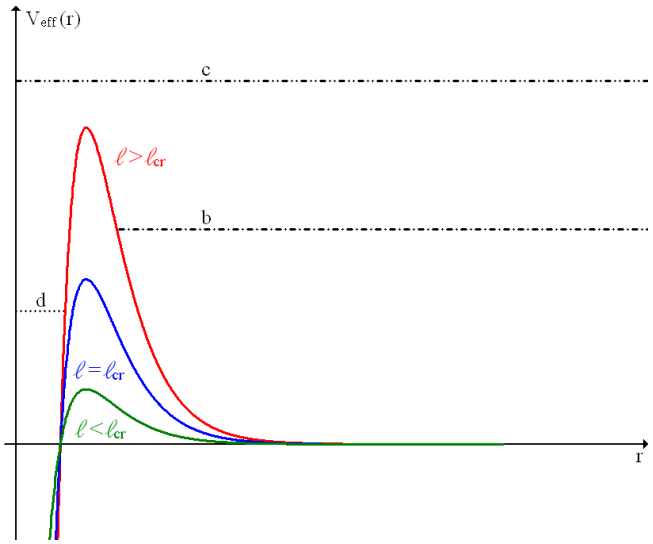

Figure 2.3: Effective potential for photons with different specific angular momenta in the Schwarzschild metric.

- i.e. the horizontal line in the plot degenerates to a point in the minimum of $V_{\text{eff}}(r)$. Although this is also the case for the maximum of $V_{\text{eff}}(r)$, here the solutions are unstable, since small perturbations lead to exponentially growing or shrinking orbits. The criterion for stationary points of the potential reads:

$$\frac{dV_{\text{eff}}(r)}{dr} = \frac{GM}{r^2} - \frac{\ell^2}{r^3} + \frac{3GM\ell^2}{c^2 r^4} = 0 \tag{2.87}$$

with the solutions

$$r_{1,2} = \frac{\ell^2}{c^2 R_s} \pm \frac{\ell}{c}\sqrt{\frac{\ell^2}{c^2 R_s^2} - 3} \tag{2.88}$$

In order to obtain two different real solutions, the specific angular momentum must satisfy

$$\ell > \sqrt{3} R_s c =: \ell_{\text{cr}} \tag{2.89}$$

In this case, r_1 and r_2 are the radii of maximum and minimum effective potential, respectively. For $\ell \to \ell_{\text{cr}}$ the centrifugal barrier becomes smaller until maximum and minimum of $V_{\text{eff}}(r)$ coincide at $\ell = \ell_{\text{cr}}$. For $\ell < \ell_{\text{cr}}$ the effective potential decreases monotonically towards the center and the particle is gravitationally captured, regardless of its energy.

Hence, stable circular orbits are only possible for test particles with $\ell \geq \ell_{\text{cr}}$ and thus only exist for

$$r \geq 3R_s \tag{2.90}$$

The orbit with $r = 3R_s$ is referred to as the *last stable orbit* (LSO). The test particle travels on it with half the speed of light. Furthermore it is of

interest to note that the orbital period T_{circ} of this motion (as measured by a remote observer) is correlated with the radius of the orbit exactly by Kepler's third law:

$$T_{\text{circ}} = \frac{2\pi}{\sqrt{GM}}\, r^{\frac{3}{2}} \tag{2.91}$$

which can be easily derived from equations (2.78), (2.79), (2.81) and (2.88). In particular, the orbital period of the last stable orbit is:

$$T_{\text{LSO}} = \frac{6\sqrt{6}\pi}{c}\, R_s \tag{2.92}$$

Photons may also move on circular orbits, if their energy equals the maximum of the effective potential. This is the case at the so called *photon sphere* with the radius

$$r_{\text{ps}} = \frac{3}{2} R_s \tag{2.93}$$

However, these orbits are unstable and small perturbations finally lead to either gravitational capture or deflection to infinity. The latter causes images of light-emitting objects orbiting massive bodies to appear more than once in different places. One speaks of *secondary* or even *tertiary* images of one and the same object. In principle, infinitely many images should appear around the central body, but due to photons being ejected from the circular orbit into arbitrary directions, the probability for observing photons that have traveled more than three revolutions is practically zero.

2.3 The rotating black hole

The gravitational collapse of a realistic star produces a black hole somewhat different from the very special case of a Schwarzschild black hole. This is because the star may be nonspherical and have a net intrinsic angular momentum and charge. Perturbation-theory calculations predict a final black hole with an external field determined entirely by the mass M, the charge Q and the intrinsic angular momentum S (spin) of the collapsing star. In the early 70's, Stephen Hawking, Werner Israel and Brandon Carter could strongly support this fact to be valid for the final black hole as well [26]. The famous theoretician John Wheeler expressed this insight in a more casual way:

"*Black holes have no hair.*"

To put it another way, all other information about the matter which formed the black hole or is falling into it, disappears behind the black hole event horizon and is therefore permanently inaccessible to external observers.

2.3.1 Kerr metric

Solving the Einstein field equation subject to the constraints imprinted by M, Q and S is pretty complex and won't be illustrated here. The solution turns out to be the so called *Kerr-Newman metric*, first found by Ezra Newman et al. in 1965. In astrophysics, the total electric charge of a body can typically be treated as small and accordingly be neglected. Thus, for our purpose it is enough to study the case $Q = 0$, which reduces the Kerr-Newman metric to the *Kerr metric*, named after the mathematician Roy Kerr, who found it in 1963 [22].

Written in the t, r, θ, ϕ coordinates of Boyer and Lindquist [4], which are generalized Schwarzschild coordinates, it reads:

$$ds^2 = \left(1 - \frac{R_s r}{\Sigma}\right) c^2 dt^2 + \frac{2R_s rac \sin^2\theta}{\Sigma}\, dt d\phi - \frac{\Sigma}{\Delta}\, dr^2 - \Sigma\, d\theta^2 - \frac{A \sin^2\theta}{\Sigma}\, d\phi^2 \tag{2.94}$$

with

$$\begin{gathered} \Sigma := r^2 + a^2 \cos^2\theta \quad , \quad \Delta := r^2 - R_s r + a^2 \\ A := \left(r^2 + a^2\right)^2 - a^2 \Delta \sin^2\theta \end{gathered} \tag{2.95}$$

The quantity a is called the *spin-parameter* of the black hole, defined as

$$a := \frac{S}{cM} \tag{2.96}$$

It can be shown that the Kerr metric has a horizon and therefore describes a black hole, if and only if

$$a^2 < \frac{G^2 M^2}{c^4} = \left(\frac{R_s}{2}\right)^2 \tag{2.97}$$

It seems likely that in any collapsing body violating this constraint, centrifugal forces will halt the collapse before a black hole can be formed, but this could not be proven yet.

The metric coefficients in (2.94) are independent of t and ϕ, thus the spacetime geometry is time-independent (*stationary*) and axially symmetric in the chosen reference frame. Due to the non-diagonal element g_{03} in the metric tensor, local coordinate frames are tilted with respect to different r and θ. This so called *frame dragging* is caused by the black hole's spin and produces a precession of gyroscopes relative to distant stars. The dragging becomes more and more extreme the closer one approaches the horizon of the rotating black hole, which is located at

$$\Delta = 0 \qquad \Rightarrow \qquad r = r_{\mathrm{h}} := \frac{R_s}{2} + \sqrt{\left(\frac{R_s}{2}\right)^2 - a^2} \tag{2.98}$$

and is smaller than the Schwarzschild horizon. Before the horizon is reached though, at a surface described by

$$\frac{R_s r}{\Sigma} = 1 \qquad \Rightarrow \qquad r = r_{\mathrm{sl}} := \frac{R_s}{2} + \sqrt{\left(\frac{R_s}{2}\right)^2 - a^2 \cos^2\theta} \tag{2.99}$$

the dragging becomes so extreme that no observer can possibly remain at rest there, relative to the distant stars. The world line of an observer with constant r, θ and ϕ changes from timelike at $r > r_{\mathrm{sl}}$ to spacelike at $r < r_{\mathrm{sl}}$, since g_{00} changes sign at r_{sl}. That means, all observers within r_{sl} must orbit the black hole in the same direction in which it rotates. This critical surface is called the *static limit* and coincides with the horizon only at the poles of the rotating black hole. The region of spacetime between the horizon and the static limit is referred to as *ergosphere* (see Figure 2.4).

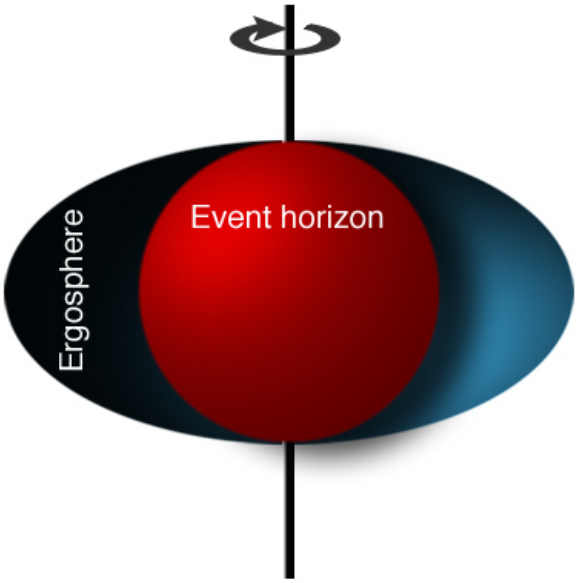

Figure 2.4: Event horizon and ergosphere of a Kerr black hole (from Wikipedia).

2.3.2 Orbital motion

In general, the motion of test particles and photons along geodesics in the gravitational field of a rotating black hole is fairly complicated, because the field has no spherical symmetry. However, exploitation of axial symmetry

provides three integrals of motion [31]:

$$\varepsilon = \left(1 - \frac{2Mr}{\Sigma}\right)\frac{dt}{d\tau} + \frac{2Mra\sin^2\theta}{\Sigma}\frac{d\phi}{d\tau} \tag{2.100}$$

$$\ell_z = -\frac{2Mra\sin^2\theta}{\Sigma}\frac{dt}{d\tau} + \frac{A\sin^2\theta}{\Sigma}\frac{d\phi}{d\tau} \tag{2.101}$$

$$\varkappa = a^2\cos^2\theta\left(\kappa - \varepsilon^2\right) + \ell_z^2\cot^2\theta + \Sigma^2\left(\frac{d\theta}{d\tau}\right)^2 \tag{2.102}$$

where ε can be again identified with the specific energy and ℓ_z the specific angular momentum, projected onto the rotation axis of the black hole. $\varkappa$ is a further constant of motion found by Brandon Carter in 1968 [7]. The definition of κ is the same as in (2.82). Notice, that the above equations are written in *geometrized units* with $G = c = 1$ (see Appendix B). For the sake of clarity it is better to use this unit system further on.

One can now express the four equations of motion through these conserved quantities:

$$\Sigma\frac{dt}{d\tau} = a\left(\ell_z - a\varepsilon\sin^2\theta\right) + \frac{r^2+a^2}{\Delta}\left[\varepsilon\left(r^2+a^2\right) - \ell_z a\right] \tag{2.103}$$

$$\Sigma\frac{dr}{d\tau} = \pm\sqrt{\left[\varepsilon\left(r^2+a^2\right) - \ell_z a\right]^2 - \Delta\left[\kappa r^2 + \left(\ell_z - a\varepsilon\right)^2 + \varkappa\right]} \tag{2.104}$$

$$\Sigma\frac{d\theta}{d\tau} = \pm\sqrt{\varkappa - \cos^2\theta\left[a^2\left(\kappa - \varepsilon^2\right) + \frac{\ell_z^2}{\sin^2\theta}\right]} \tag{2.105}$$

$$\Sigma\frac{d\phi}{d\tau} = \frac{\ell_z}{\sin^2\theta} - a\varepsilon + \frac{a}{\Delta}\left[\varepsilon\left(r^2+a^2\right) - \ell_z a\right] \tag{2.106}$$

Investigation of the radial equation (2.104) yields a criterion for characterizing the type of motion. In order to keep a positive sign beneath the square root, for $\varepsilon^2 < 1$ the radial coordinate r has to be finite. Only if $\varepsilon^2 > 1$ can the motion be infinite.

For a more detailed analysis of orbits it is convenient to work with an effective potential, as done before in the nonrotating case. Let us rewrite (2.104) as

$$\Sigma\frac{dr}{d\tau} = \pm\sqrt{\alpha\varepsilon^2 - 2\beta\varepsilon + \gamma} \tag{2.107}$$

with

$$\begin{gathered}\alpha := r^4 + a^2\left(r^2 + 2Mr\right) \quad , \quad \beta := 2aM\ell_z r \\ \gamma := \ell_z^2 a^2 - \left(\kappa r^2 + \ell_z^2 + \varkappa\right)\Delta\end{gathered} \tag{2.108}$$

The radial turning points occur when $dr/d\tau = 0$ and can be determined by the condition

$$\varepsilon = \frac{\beta \pm \sqrt{\beta^2 - \alpha\gamma}}{\alpha} =: V_{\text{eff}}^{\pm}(r) \tag{2.109}$$

which defines an *effective Potential*. The motion of a particle with specific energy ε is possible only in the regions with either $\varepsilon \geq V_{\text{eff}}^{+}$ or $\varepsilon \leq V_{\text{eff}}^{-}$. Apparently, the specific energy can be negative as well. It can be shown that orbits with negative ε are possible within the ergosphere for any $\theta \neq 0, \pi$. These orbits grant the possibility to devise processes that extract rotational energy from the black hole. Such processes were discovered by Roger Penrose in 1969.

For a rotating black hole the variety of trajectories becomes wider and their classification is much more involved than in the Schwarzschild case. Again there are bound as well as unbound motions resulting in either stable movements, gravitational capture (see Figure 2.5) or rejection to infinity. But due to the breakdown of spherical symmetry, orbits are not necessarily confined to a plane anymore. Additionally one has to distinguish between *co-rotating* and *counter-rotating* orbits, meaning the sense of rotation with respect to the black hole spin.

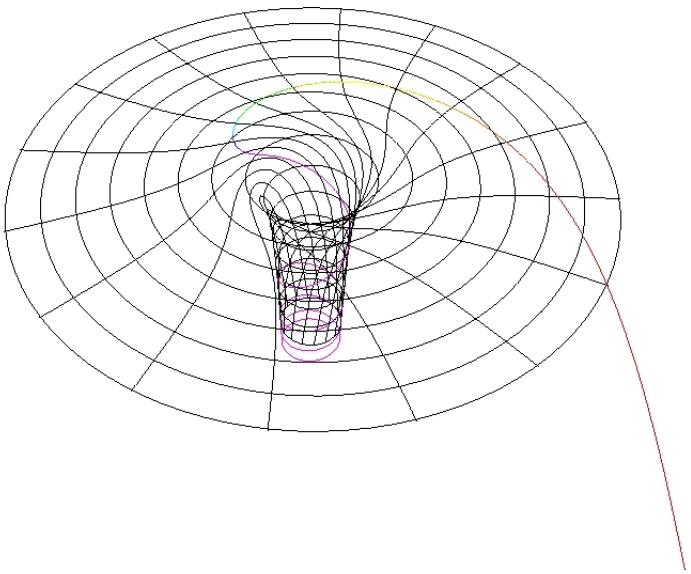

Figure 2.5: Trajectory of a particle, dragged along by the spacetime around a clockwise rotating Kerr black hole. Due to frame dragging the geodesic is forced to follow the rotation of the black hole at a certain distance to it.

Circular orbits

Let us now focus on circular motion of massive particles ($\kappa = 1$) in the equatorial plane. To this end we have to consider the special case of $\theta = \pi/2$ and find the extrema of $V_{\text{eff}}^{\pm}(r)$. From this one obtains the expressions for the specific energy and angular momentum as functions of the radius of the

circular motion:

$$\varepsilon_{\rm circ} = \frac{r^2 - 2Mr + a\sqrt{Mr}}{r\left(r^2 - 3Mr + 2a\sqrt{Mr}\right)^{1/2}} \tag{2.110}$$

$$\ell_{\rm circ} = \pm\frac{\sqrt{Mr}\left(r^2 - 2a\sqrt{Mr} + a^2\right)}{r\left(r^2 - 3Mr + 2a\sqrt{Mr}\right)^{1/2}} \tag{2.111}$$

The upper sign corresponds to *co-rotating* orbits ($\ell_z, a > 0$) and the lower sign corresponds to *counter-rotating* orbits ($\ell_z, a < 0$).

The angular frequency of a test particle on the circular orbit as seen by a distant observer is computed via equations (2.103) and (2.106):

$$\omega_{\rm circ} = \frac{d\phi}{dt} = \frac{d\phi}{d\tau}\frac{d\tau}{dt} = \pm\left(\frac{r^{3/2}}{\sqrt{M}} + a\right)^{-1} \tag{2.112}$$

From here one can easily derive the generalization of Kepler's third law, which relates the orbital period with the orbital radius of particles around rotating bodies:

$$T_{\rm circ} = \left|\frac{2\pi}{\omega_{\rm circ}}\right| = 2\pi\left(\frac{r^{3/2}}{\sqrt{M}} + a\right) \tag{2.113}$$

Note that the denominator in the expressions for $\varepsilon_{\rm circ}$ and $\ell_{\rm circ}$ is real only for those values of r meeting the condition

$$r^2 - 3Mr + 2a\sqrt{Mr} > 0 \tag{2.114}$$

This sets a lower limit to the radius of the circular orbit which describes the *photon sphere* for rotating black holes:

$$r_{\rm ps} = 2M\left\{1 + \cos\left[\frac{2}{3}\arccos\left(-\frac{a}{M}\right)\right]\right\} \tag{2.115}$$

It can only be occupied by particles as fast as light, i.e. photons, and it is unstable. Massive particles only move on circular orbits with $r > r_{\rm ps}$. These are unstable for radii smaller than the last stable orbit of the Kerr metric, given by

$$r_{\rm LSO} = M\left[3 + Z_2 \mp \sqrt{(3 - Z_1)(3 + Z_1 + 2Z_2)}\right] \tag{2.116}$$

with

$$Z_1 := 1 + \left(1 - \frac{a^2}{M^2}\right)^{1/3}\left[\left(1 + \frac{a}{M}\right)^{1/3} + \left(1 - \frac{a}{M}\right)^{1/3}\right] \tag{2.117}$$

$$Z_2 := \sqrt{3\frac{a^2}{M^2} + {Z_1}^2} \tag{2.118}$$

Obviously, particles co-rotating with a spinning black hole may get closer to it than particles on counter-rotating orbits or particles orbiting static black holes without being captured. The absolute velocity v of the orbiting particle can be calculated in the *locally nonrotating frame* (LNRF), a reference frame in some sense "rotating with the geometry" of Kerr-spacetime [3]. Only this choice of coordinate system gives a meaningful definition of the ordinary local velocity. One finds:

$$v = \frac{M^{1/2}\left(r^2 - 2aM^{1/2}r^{1/2} + a^2\right)}{\Delta^{1/2}\left(r^{3/2} + aM^{1/2}\right)} \tag{2.119}$$

As a summary, Figure 2.6 displays all the characteristic radii derived above. In the limiting case of $a = M$ the last stable orbit coincides with the photon sphere and the horizon. Note also that the last stable orbit does not enter the ergosphere until $a \approx 0.94M$.

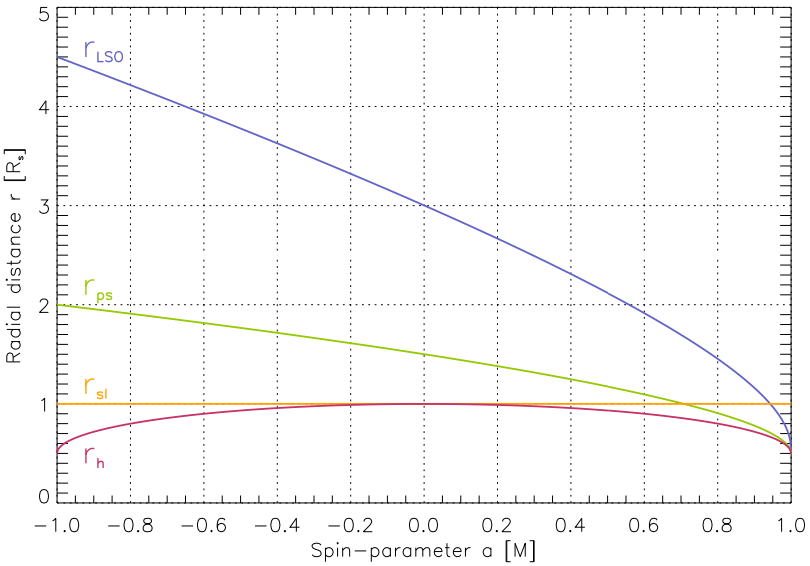

Figure 2.6: Characteristic radii in the Kerr metric for all possible values of a. Shown are the last stable orbit (blue), the photon sphere (green), the static limit in the equatorial plane (yellow) and the horizon (red).

It is interesting to see how equation (2.113) deviates from the third classical Kepler law (2.91). In Figure 2.7 and Figure 2.8 this is illustrated by three-dimensional plots showing the dependency of the orbital period of a co-rotating test particle on its orbital radius and the spin-parameter in the case of SgrA*. In Figure 2.7 the orbital radius is expressed in Schwarzschild radii, whereas in Figure 2.8 it is displayed in units of the last stable orbit. The latter representation accentuates the influence of the black hole spin more strongly.

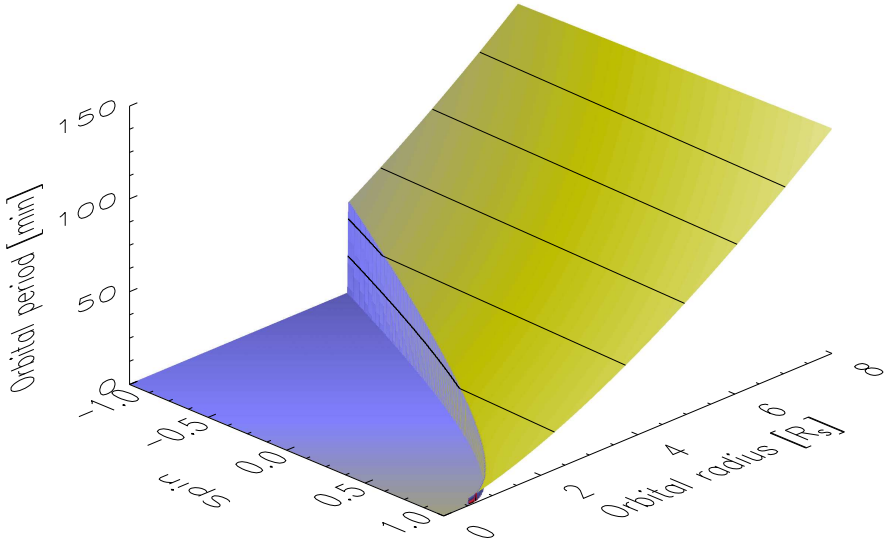

Figure 2.7: Dependency of the orbital period T_{circ} in minutes on the spin-parameter $a[M_{\text{SgrA}^*}]$ and the orbital radius r in units of $R_s = 2M_{\text{SgrA}^*}$. Unstable orbits are assigned $T_{\text{circ}} = 0$. For every multiple of 20min a contour line is drawn.

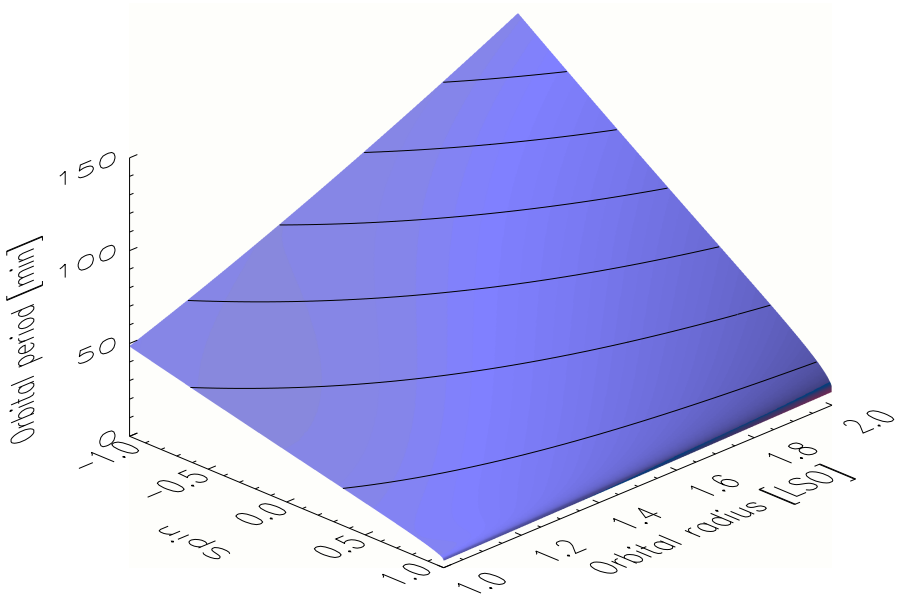

Figure 2.8: Dependency of the orbital period T_{circ} in minutes on the spin-parameter $a[M_{\text{SgrA}^*}]$ and the orbital radius r in units of the last stable orbit radius. For every multiple of 20min a contour line is drawn.

Chapter 3

Visualization

In this chapter the method of four-dimensional ray tracing in nontrivial spacetimes will be outlined in brief. First, the basic concept is discussed with the help of simple examples. Further to this the special cases of Schwarzschild- and Kerr-geometry will be investigated more closely.

3.1 Concept

An image from our surroundings is generated as light hits our retina. It can be retained on a screen capable of recording the visible information, like a photographic film or a CCD-chip. This light may either emanate directly from a light source (primary rays), or indirectly from a reflecting object (secondary rays, or *shadow rays*).

However, only a diminutive fraction of this light, generally emitted into any direction, reaches the eye or the camera of the observer. A technique simulating this natural process would be enormously inefficient, since most of the light rays would unnecessarily be traced. Instead, light rays are traced back from the eye of the observer or the camera to the place of their emission. This procedure is called *ray tracing concept* (see Figure 3.1).

3.1.1 Conventional ray tracing

Conventional three-dimensional ray tracing assumes a static scene, straight light rays and neglects their finite propagation speed. An image is created by generating a light ray for each pixel.

This primary ray is then checked to see if it hits either a light source or an object. In the latter case the object has to be inspected to determine whether it is illuminated from a light source or a further reflecting object. In order to do this, a secondary ray is created to test for sections with all other objects. The direction of the secondary ray is determined by geometric and physical criteria like angle of incidence, surface integrity and reflexion

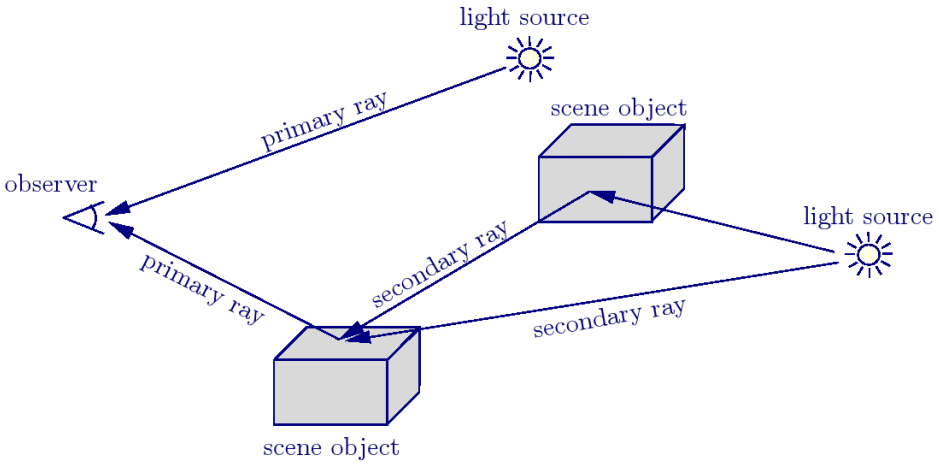

Figure 3.1: Concept of ray tracing: light rays are traced back from the observer to the scene until they hit an object or leave the considered region. Additionally, secondary rays, or so called *shadow rays* are traced (from [29]).

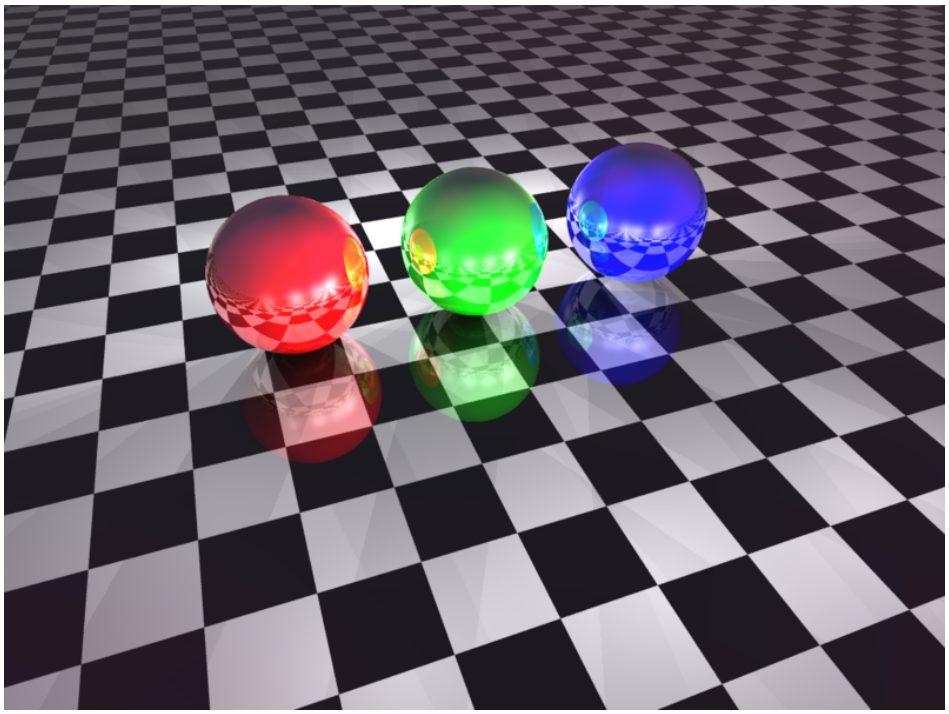

Figure 3.2: Ray traced image of three spheres that reflect off the floor and each other (from Wikipedia).

properties respectively. As an example, Figure 3.2 displays an arrangement of three spheres on a checkered, reflecting floor. The spheres also cause reflections on each other.

3.1.2 Ray tracing in special relativity

The extension to four-dimensional ray tracing also takes into account the finite speed of light and the temporal evolution of the scene. Therefore, both the camera and every single object may move in space with velocities up to c. In this case every ray has to be Lorentz-transformed into the inertial reference frame of the moving object at the place of incidence. In addition to these pure geometrical issues, frequency shifts due to the relativistic Doppler effect and intensity variations via relativistic beaming have to be implemented.

Consider for instance a set of 16 balls, aligned in a row on the y-axis and at rest in the reference frame S. Another ball (reference frame S') moves with $v = 0.9c$ above this row in the positive y-direction. The observer (reference frame S") moves along the x-axis with the same speed towards the row. At a certain time, he takes an image of this scene with a panorama camera. Figure 3.3 displays the setup of the scene and the resulting image (without taking into account frequency shifts and intensity variations).

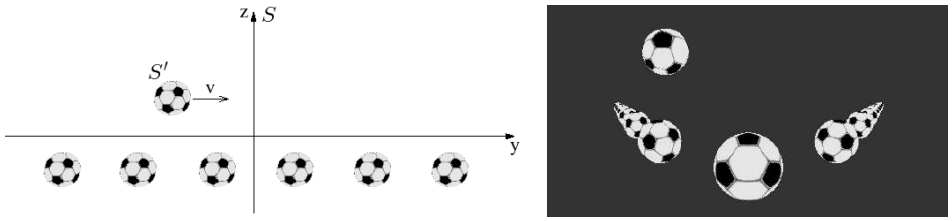

Figure 3.3: Ray tracing in special relativity. Left: Setup of a special relativistic scene. Right: An observer approaching along the x-axis with 90 percent the speed of light observes this image (from [29]).

Notice that the balls appear to be rotated in the image. This effect is due to different propagation times of light rays originating from the side and the front of the object.

3.1.3 Ray tracing in general relativity

The concept of four-dimensional ray tracing can further be extended to curved spacetimes. In that case light rays are bent, they follow null geodesics and have to be computed from the geodesic equations. To this end a traverse is numerically calculated by an integrator with a certain accuracy and then intersected with the objects of the scene. This is a very intricate procedure, since every segment of the light ray has to be intersected with every object.

Fortunately, the fact that different null geodesics do not affect each other allows for parallelizing the code, i.e. subdividing the field of view into smaller partitions to be computed and connected later on.

Three limits on the integration of the geodesic equations are specified. Firstly, a maximum amount of points tolerated for the entire geodesic has to be fixed. The second limit is a *bounding box*, assigning a finite domain for the computation of geodesics. A geodesic leaving this *bounding box* is not taken care of anymore. Lastly, the third limit is set by the spacetime itself, which defines the observable light trajectories. In the Schwarzschild metric, one limit is given by the event horizon, for example.

A further difficulty is the description of objects in curved spacetime. The freedom to choose arbitrary coordinates for a spacetime brings about different appearances of the objects. One has to decide on such a coordinate system that visualizes the objects correctly. Another aspect is the deformation of extended bodies due to tidal forces, which must not be confused with the effect of light bending.

When all the components of a scene are defined, they make up a *device*. It contains all the elements necessary for the construction of the image:

- A metric describing the spacetime
- An integrator for the null geodesics
- A ray generator
- An observer camera
- A local reference frame of the observer
- A projector for the image synthesis
- A light source manager
- The objects

In practice, the visualization of a general relativistic scene is computationally quite intensive. A geodesic with a minimum of a thousand points has to be calculated for every single pixel. The generated polyline then has to be intersected segment-wise with every object. For an image of 1000 $\times$ 1000 pixels and a single object this already yields one billion intersections, taking roughly 50 minutes of computing time for a single-CPU machine. Rendering a movie sequence of merely one second (about 25 frames) takes 25 hours. Thus it is inevitable to parallelize the image computation to run on multiple CPU's.

An impressive application for a general relativistic scene is a differentially rotating dust torus around a static black hole. Properties of such a disk are calculated in *smoothed particle hydrodynamics*. Figure 3.4 shows

such a configuration. Light bending and Doppler effects are clearly visible. The clumps in the accretion disk are high density concentrations of hot matter.

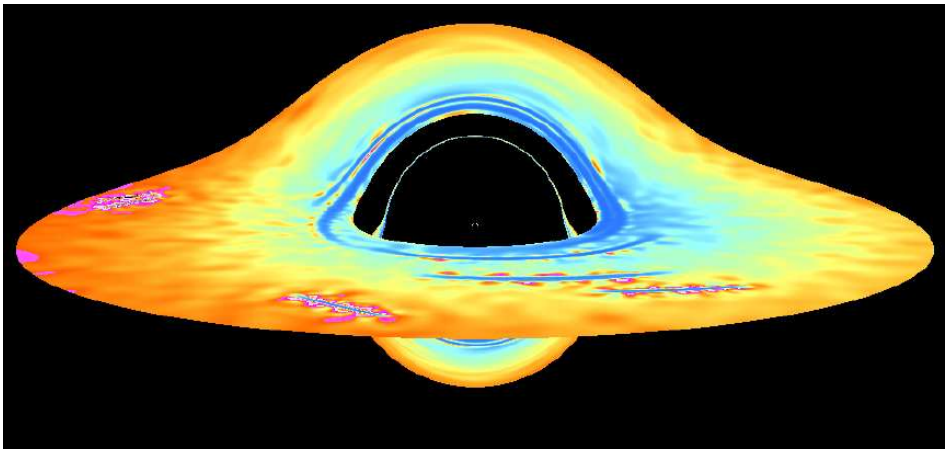

Figure 3.4: Ray tracing in general relativity. A clockwise differentially rotating accretion disc around a static black hole, seen from 10 degrees above the equatorial plane (from [29]).

3.2 Visualization of an orbiting hot spot

3.2.1 Setup

We now focus on the favored scenario for the origin of the flares from Sagittarius A*, namely the orbiting hot spot model. We consider a very simplified configuration with a nonrotating sphere (radius $0.25R_s$) on a circular orbit in the equatorial plane around a static or rotating black hole. Its surface is homogeneous and emits light isotropically. Tidal forces and gravitational influences of the sphere on the spacetime are neglected. Figure 3.5 displays a sequence of eight ray traced images of such a scenario, without accounting for Doppler- and beaming-effects. The observing camera is a pinhole camera, situated $60R_s$ away from a black hole of mass M, 30 degrees above the equatorial plane.

The visualization was carried out by *GeoViS*, a four-dimensional ray tracing software designed by *Thomas Müller* at the department for theoretical astrophysics in Tübingen, Germany [29].

One can clearly see a distortion of the sphere, especially as it passes the rear part of the orbit. Furthermore, multiple images of the object appear at different locations of the image. A *secondary* image, corresponding to light rays that orbit the black hole once, can be seen in every frame. Occasionally, even a *tertiary* image appears. It is very faint, because only few photons

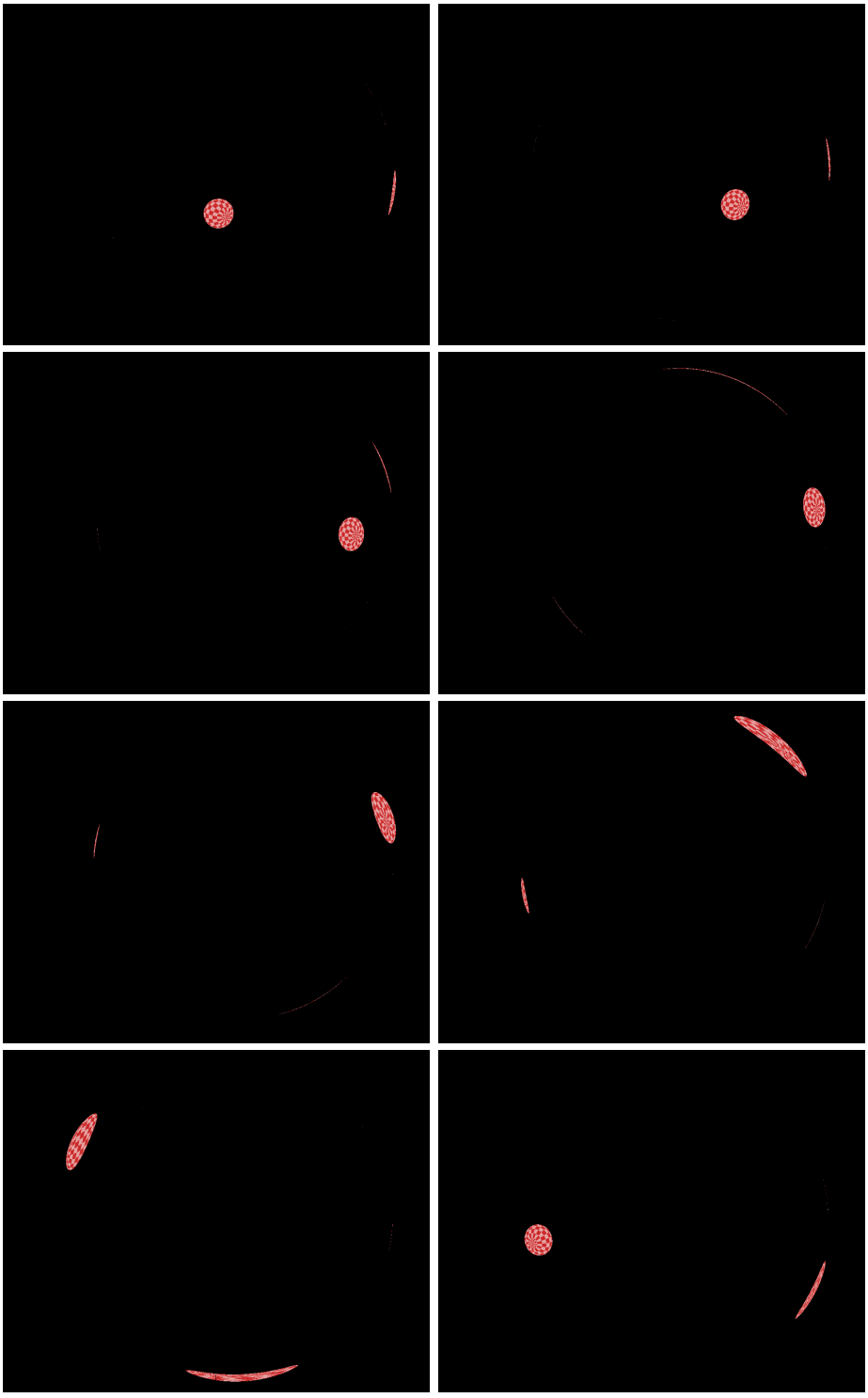

Figure 3.5: Ray traced images of a sphere orbiting a Kerr black hole ($a = 0.52M$) on the LSO in 70° inclination. Only the effects of light bending are shown.

complete two orbits and then reach the observer. The location of the additional images is not only determined by the location of the source, but also by the travel times of the light rays. An illustration is given in Figure 3.6.

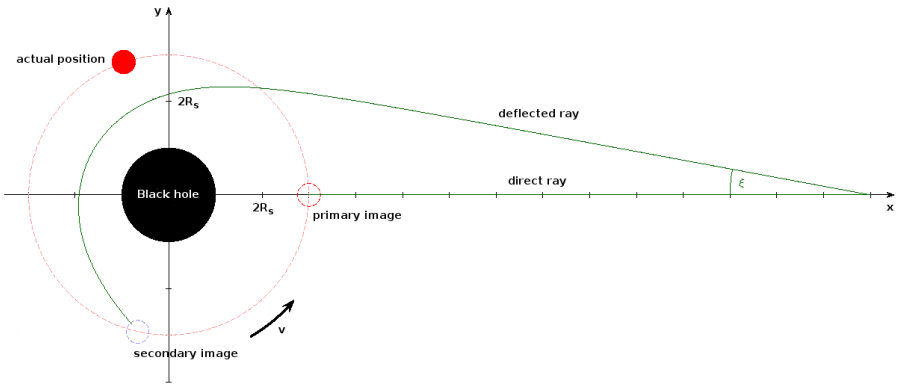

Figure 3.6: Real and apparent locations of the sphere at the observer's coordinates t_o and r_o. While the light rays from the source travel to the observer, the source continues moving. The secondary image of the sphere stems from even earlier times and appears at an angle ξ (from [29]).

3.2.2 Data output

The ray tracing simulations do not provide only geometrical information on the moving sphere; the computation of frequency shifts as well as emission times of the observed light rays is also supported.

In order to distinguish multiple images of the source it is useful to have the emission time of each light ray that reaches the observer. Therefore, each pixel contains a real number T. It specifies the date in coordinate time, when the light ray was emitted. Thus, higher-order images have earlier emission times than primary images. Knowing T for every pixel allows to transform the intrinsic brightness evolution of the source from proper time to coordinate time, including the light travel times to the observer.

In addition to this the simulations provide maps of frequency shifts with one real number D per pixel, giving the ratio of the emitted frequencies in the observer's and the source's frame of reference:

$$D = \frac{\nu_o}{\nu_s} \tag{3.1}$$

These frequency shifts depend both on the motion of the source and the geometry of spacetime.

For a particular configuration, one whole orbit is divided into a sequence of equally separated frames. Frame rate and field of view of each configuration have to be adjusted properly to achieve a reasonable temporal and spatial resolution.

3.2.3 Simulation parameters

The occurrence of an orbiting hot spot in the vicinity of the supermassive black hole in the Galactic Center may appear in one of many possible configurations. In order to establish comparison with observed data, it is convenient to set up a grid of several parameters that characterize the model best. In this work these are:

- Radius of the orbit ($r_\mathrm{o}/r_\mathrm{LSO} = 1.0,\ 1.2,\ 1.5,\ 2.0$)
- Inclination of the orbit ($i = 20°, 50°, 70°, 90°$)
- Spin of the black hole ($a/M = 0,\ 0.52,\ 0.7,\ 0.998$)

For each parameter the values in brackets have been decided on. All possible combinations of these yield a grid of $4 \cdot 4 \cdot 4 = 64$ different setups to be simulated. They were carried out by *Thomas Müller* on a computer cluster at the *Institut für Visualisierung und Interaktive Systeme* (VIS) in Stuttgart (for $a = 0.998M$, only a few simulations were carried out).

Chapter 4

The code

The raw data produced by the ray tracing code is the basis for all the simulations described in this work. Here, the main components of the code will be illustrated to elucidate how the output is assembled. Furthermore, the implementation of a hot spot model will be motivated on the basis of various physical assumptions.

4.1 Subroutines

The code consists of four major subroutines which are stored in different include-files and can be run independently from each other. They are all written in *Yorick*, an interpreted programming language for scientific simulations. It is an open-source software, which is available at *http://yorick.sourceforge.net*. Originally, these subroutines were coded by *Thibaut Paumard* at the MPE. However, in the course of this work they have been modified and extended.

4.1.1 Simulation initializer

In order to start a new simulation run it is necessary to specify its detailed properties. First of all, a name for the particular run must be assigned to distinguish between different models. Then, one of the grid-configurations has to be loaded and its parameters passed on to calculate the orbital parameters. All the specific parameters of the different flare models and the observing instrument can be declared and varied here. They will be introduced in the following subsections.

It is also possible to define the quality of the simulation by specifying the number of frames to be computed and the time steps between them. The quality is limited by the number of frames delivered by the ray tracing code. All important variables declared in the initializer can be stored in a text file. This is important for comparison of different models later on.

Finally, the data-processing subroutines are called. It is also possible to loop over many different grid-configurations.

4.1.2 Image integrator

The image integrator is responsible for creating physically motivated realistic images from the raw frames. Its main purpose is to co-add (integrate) all the frames of one orbit and assign different apparent brightnesses to different orbital locations of the hot spot. This procedure allows the assignment of an arbitrary brightness distribution to the whole orbit of the spot, which may include a shearing arc or an accretion disk as described in section 4.2.

It is implemented as follows: The apparent flux density S of the blob and its multiple images in a particular frame depends both on the emission times T of the received light rays and the frequency shifts D caused by gravitational redshift and Doppler effects. It can be expressed via the specific intensity I_ν or the specific flux density S_ν:

$$S = S(T, D) \equiv \int S_\nu(T, D)\, d\nu \equiv \iint I_\nu(T, D)\, d\nu\, d\Omega \tag{4.1}$$

Suppose the sphere emits radiation with a power law spectral energy distribution (SED). Let the specific flux density in the sphere's reference frame behave as

$$\nu_s S_{\nu_s} = k\, {\nu_s}^\alpha \tag{4.2}$$

with $k \equiv k(T)$ being a constant of proportionality and α the *spectral index* of the SED. We can now apply Liouville's theorem (section 2.1.5) and use the expression for the Lorentz invariant to obtain the specific flux density a remote observer would measure ('s' for source and 'o' for observer):

$$\frac{S_{\nu_s}}{{\nu_s}^3} = \frac{S_{\nu_o}}{{\nu_o}^3} \equiv \text{const.} \tag{4.3}$$

Instead of specific intensities we can also use specific flux densities, since we assume a constant solid angle Ω in the observation. For the SED measured in the observer's frame of reference we get:

$$\nu_o S_{\nu_o} = \nu_o D^3 S_{\nu_s} = \nu_o D^3 k\, {\nu_s}^{\alpha-1} = \nu_o D^3 k \left(\frac{\nu_o}{D}\right)^{\alpha-1} = D^{4-\alpha} k\, {\nu_o}^\alpha \tag{4.4}$$

yielding the same power law as in (4.2) with an additional factor of $D^{4-\alpha}$. Finally we integrate over all frequencies within the observing band of the telescope and get the apparent flux density S_o:

$$S_o = \int_{\nu_1}^{\nu_2} D^{4-\alpha} k\, {\nu_o}^{\alpha-1}\, d\nu_o = \begin{cases} k\, D^{4-\alpha}({\nu_2}^\alpha - {\nu_1}^\alpha)/\alpha & \text{, if } \alpha \neq 0 \\ k\, D^4\, ln(\nu_2/\nu_1) & \text{, if } \alpha = 0 \end{cases} \tag{4.5}$$

The temporal evolution of the sphere's intrinsic brightness is completely determined by $k = k(T)$. It is one of the most important model-parameters to be varied within the simulations. Once it is assigned to the sphere, the resulting apparent flux density as seen by a remote observer can be calculated via (4.5) for every pixel in each frame.

One frame consists of a 1000×1000 pixel map for the values of T and D. A pixel with $T = 0$ is interpreted as a pixel with zero brightness. Since the pixels of higher order images show earlier emission times than lower order images, their brightness evolution lags behind.

We now have a sphere, emitting light with a power spectrum with spectral index α, revolving the black hole once. Of course, we can add more orbits to that motion by simply adding the orbital period to the emission time as soon as one orbit is closed and using the same frames again:

$$T_n(i) = n \cdot T_{\text{circ}} + T(i) \quad , n \in \mathbb{N} \tag{4.6}$$

n denotes the number of completed orbits, i the frame number and $T_n(i)$ the time of emission in the $(n+1)$'th orbit at frame i.

Eventually, we also may want other parts of the orbit to be illuminated. The compact sphere may not represent a realistic enough model due to gravitational shear or diffusion. In such a scenario material will spread out from the sphere and distribute along the orbit to build up an *arc*. This can be simulated by simply adding up all the frames of one whole orbit and assigning them a suitable brightness distribution. This is done for all of the images computed above in the following way: every pixel that has nonzero values for T in a frame j within one orbital period around a particular frame i is assigned the time of emission value

$$T_n^{\text{arc}}(i, j) = T_n(i) \tag{4.7}$$

of the central frame i. This enables us to synchronize the brightness evolution of the whole arc, spread out over the entire orbit.

Once again we assign a suitable brightness distribution to the arc. Therefore every pixel with $T \neq 0$ gets a value for its apparent flux density according to equation (4.5), except this time we can specify another spectral index α and another function k for the temporal evolution of the brightness. But not only the temporal but also the spatial distribution of the arc may be determined. The image integrator loops over all the frames i for the primary image computation elucidated above. The secondary image computation including the arc is done in a sub-loop for every image i, looping over the same total number of frames with index j. Within this loop the brightness distribution of the arc can depend both on the time of emission of the central frame $T_n(i)$ and $T_n(j)$ of the particular frame j to be computed. Hence,

$$k^{\text{arc}} = k^{\text{arc}}\left(T_n(i), T_n(j)\right) \tag{4.8}$$

For the sake of clarity the index n will be omitted in the following.

Figure 4.1 shows an example of an image produced with the technique discussed above. One can see how the arc is composed out of many different frames of the sphere with changing brightness. The integrated frames also produce the arc in the secondary image.

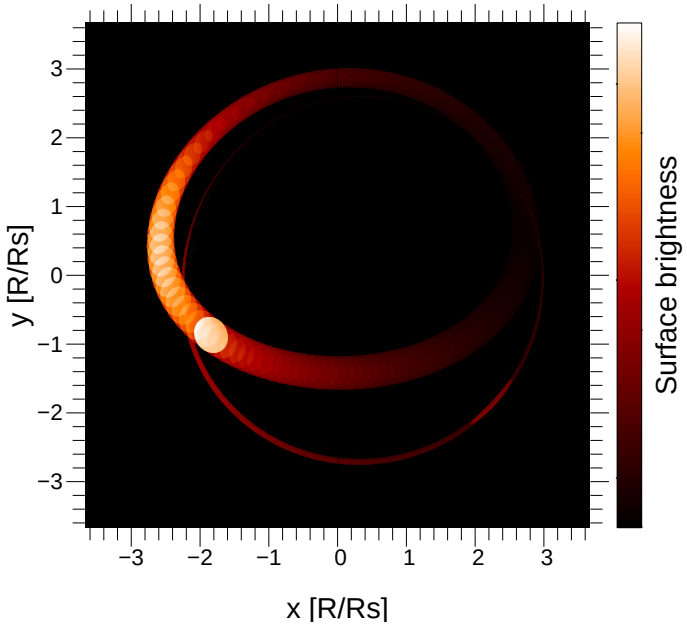

Figure 4.1: An integrated image of a radiating sphere with extended arc, following a Gaussian brightness distribution.

4.1.3 Photometry and astrometry calculator

Having computed a sequence of images for several orbits of a radiating sphere changing shape and brightness with time, we're now able to simulate an observation of this setup that could be carried out by present or future telescopes.

Light curve

As yet, the only dynamical information available from the flares of the Galactic Center are light curves (photometry and polarimetry). Therefore it is appropriate to create light curves from the simulated images to be compared with the experimental data. Since a light curve is nothing else than the temporal evolution of the integrated flux density (luminosity) of a certain area on sky, we can calculate it by summing over all the pixels in the field of view

and normalizing by the field of view's area A_{fov}:

$$\overline{S_o} = \frac{1}{A_{\text{fov}}} \sum_{\text{pix}} S_o\,(x, y) \tag{4.9}$$

Here, x and y are the pixel-coordinates within the field of view. The origin is placed in its center.

Centroid

One goal of current developments in astronomy is to combine multiple telescopes interferometrically and thereby reach very high spatial resolutions (see introduction). Although it won't be soon possible to totally resolve the light sources orbiting the black hole, movements of the centroid of the emission might be observable [35]. It can easily be computed from the simulated data:

$$\overrightarrow{C} = \frac{1}{\sum\limits_{\text{pix}} S_o\,(x, y)} \begin{pmatrix} \sum\limits_{\text{pix}} S_o\,(x, y) \cdot x \\ \sum\limits_{\text{pix}} S_o\,(x, y) \cdot y \end{pmatrix} \tag{4.10}$$

Flux integration

Not only the spatial, but also the temporal resolution of a telescope is limited. It has to collect a significant amount of flux until it can produce an image. It is therefore necessary to integrate the received flux over an appropriate *integration time*. The code simulates this by averaging a number of consecutive frames.

Furthermore one has to consider a *blind time* between successive integrations. This is because the observation of an image always requires calibration time. For the integrated light curve and centroid we then get:

$$< \overline{S_o} > (l) = \frac{1}{\Delta i} \sum_{i=j_l}^{j_l+\Delta i-1} \overline{S_o}(i) \tag{4.11}$$

$$< \overrightarrow{C} > (l) = \frac{1}{\Delta i} \sum_{i=j_l}^{j_l+\Delta i-1} \overrightarrow{C}(i) \tag{4.12}$$

where i is the frame number, Δi the number of frames to be integrated over and j_l an iteration constraint defined as

$$j_l := 1 + (l-1)(\Delta i + \Delta b) \quad , \quad l \in \left[1, 2, ..., l_{\max}\right] \tag{4.13}$$

Δb is the blind time counted in frames and $l_{\max}$ the total number of integrations for a total of N frames. It can be expressed as

$$l_{\max} = \lfloor \frac{N}{\Delta i + \Delta b} \rfloor \tag{4.14}$$

Noise

For the simulation of a realistic observation we still have ignored external influences on the light rays when they travel towards the observer. Already the interstellar medium in the line of sight to the source reddens and extenuates the radiation. In addition, light rays are deflected slightly due to atmospheric turbulences when they cross the earth's atmosphere. This effect is called *seeing* and can be corrected to great extent by an *adaptive optics* system using deformable mirrors. Finally, the telescope itself is an imperfect device and adulterates the captured signal in many places. For example, this is the case at the detector, which produces intrinsic noise.

Hence, there are plenty of disturbing influences on the wavefronts that add up in a very complicated manner. But since most of these fluctuations are randomly distributed, it is easy to reproduce them. The simplest way to do that is to add a normally (Gaussian) distributed noise to each data point:

$$< \tilde{\overline{S_o}} > = < \overline{S_o} > + \sigma_S \cdot \mathcal{R}_{\text{Gauss}} \tag{4.15}$$

$$< \tilde{\overrightarrow{C}} > = < \overrightarrow{C} > + \begin{pmatrix} \sigma_{C_x} \cdot \mathcal{R}_{\text{Gauss}} \\ \sigma_{C_y} \cdot \mathcal{R}_{\text{Gauss}} \end{pmatrix} \tag{4.16}$$

$\mathcal{R}_{\text{Gauss}}$ is a normally distributed random number with a mean of zero and standard deviation of one. Multiplication with the uncertainties σ_S and $\sigma_{C_x}, \sigma_{C_y}$ of the light curve and the components of the centroid respectively, scales the standard deviation to the corresponding values. Their magnitude can be taken from existing observational data.

4.1.4 Movie generator

All of the produced data can be visualized in a small video clip in *mpeg*-format. The simulated frames are colorized using a proper color palette that indicates the apparent flux density of every pixel. Arranging the images one after another with appropriate spacing creates a smooth movie. Additionally, a real time drawing of the light curve and the centroid track is implemented, so one can immediately observe the influences from the model on the observational data.

4.2 Model implementation

At this point we begin to specify particular properties of the matter in the close black hole orbit. The hot spot scenario has plenty degrees of freedom of which many will be fixed by further assumptions. Especially the electron heating process via magnetic reconnection is a complex phenomenon. Strong simplifications will be used to describe such an event. Moreover one has to consider shear or diffusion, which can be caused by different effects.

4.2.1 Blob-arc-model

The major constraints for modeling the flares from SgrA* are the observed light curves. In first order approximation they all appear quite symmetric, showing a smooth rise followed by a smooth decay, in total lasting for a timescale of roughly one hour. On top of these fairly bright flares one can distinguish smaller variations on a typical timescale of about 20 minutes, in our model corresponding to the orbital period of a hot spot.

We will now proceed on the assumption that the shorter variations are due to a compact source (sphere/blob) on a circular orbit around the black hole, periodically brightened and dimmed through relativistic effects depending on the orbital phase. Furthermore we add an arc, spreading from the sphere due to shear or diffusion. We assume the broad shape of the flare light curve is caused by a heating process of the sphere. It is heated or excited in the vicinity of the black hole and then spreads along the orbit and cools again.

For the intrinsic brightness evolution of the sphere we use two Gaussians, one for the rise part and one for the decay part:

$$k^{\mathrm{s}} = \begin{cases} k^{\mathrm{s}}_{\mathrm{peak}}\, exp\left(-\frac{1}{2}\left(\frac{T(i)-T^{\mathrm{s}}_{\mathrm{peak}}}{\sigma^{\mathrm{s}}_{\mathrm{rise}}}\right)^2\right) & \text{, if } T(i) < T^{\mathrm{s}}_{\mathrm{peak}} \\ k^{\mathrm{s}}_{\mathrm{peak}}\, exp\left(-\frac{1}{2}\left(\frac{T(i)-T^{\mathrm{s}}_{\mathrm{peak}}}{\sigma^{\mathrm{s}}_{\mathrm{decay}}}\right)^2\right) & \text{, if } T(i) > T^{\mathrm{s}}_{\mathrm{peak}} \end{cases} \tag{4.17}$$

The width of each Gaussian can be adjusted by $\sigma^{\mathrm{s}}_{\mathrm{rise}}$ and $\sigma^{\mathrm{s}}_{\mathrm{decay}}$, the peak brightness and the corresponding peak time of the light curve by $k^{\mathrm{s}}_{\mathrm{peak}}$ and $T^{\mathrm{s}}_{\mathrm{peak}}$, respectively.

For the arc we additionally have to consider the spreading, which can be described by another Gaussian Q, also depending on the arc-frame j:

$$k^{\mathrm{a}} = \begin{cases} k^{\mathrm{a}}_{\mathrm{peak}}\, exp\left(-\frac{1}{2}\left(\frac{T(i)-T^{\mathrm{a}}_{\mathrm{peak}}}{\sigma^{\mathrm{a}}_{\mathrm{rise}}}\right)^2\right) Q(i,j) & \text{, if } T(i) < T^{\mathrm{a}}_{\mathrm{peak}} \\ k^{\mathrm{a}}_{\mathrm{peak}}\, exp\left(-\frac{1}{2}\left(\frac{T(i)-T^{\mathrm{a}}_{\mathrm{peak}}}{\sigma^{\mathrm{a}}_{\mathrm{decay}}}\right)^2\right) Q(i,j) & \text{, if } T(i) > T^{\mathrm{a}}_{\mathrm{peak}} \end{cases} \tag{4.18}$$

with

$$Q(i,j) := exp\left(-\frac{1}{2}\left(\frac{T(j)-T(i)}{\Delta}\right)^2\right), \tag{4.19}$$

$$\Delta := \frac{T_{\mathrm{circ}}}{2}\frac{T(i)}{\tau_{\mathrm{shear}}} \tag{4.20}$$

Thus, the arc has a similar brightness evolution as the sphere, described by $\sigma^{\mathrm{a}}_{\mathrm{rise}}$, $\sigma^{\mathrm{a}}_{\mathrm{decay}}$, $k^{\mathrm{a}}_{\mathrm{peak}}$ and $T^{\mathrm{a}}_{\mathrm{peak}}$. Additionally, its extension is described by Δ, the width of Q. It is linearly changing with time being zero at $T(i) = 0$ and half an orbital period at $T(i) = \tau_{\mathrm{shear}}$. Hence, τ_{shear} is the characteristic shear time of the arc that determines the smearing of the entire orbit on a one sigma level. Depending on the shear mechanism, τ_{shear} is in different parts influenced by the orbital parameters of the hot spot, the properties of the plasma, the magnetic field and possibly even more quantities. Two special cases for the shear mechanism are illustrated below.

Figure 4.2 illustrates the spatial and temporal brightness distribution of a blob with a spreading arc. The elevation of the plotted surface represents the intrinsic flux density of the two sources.

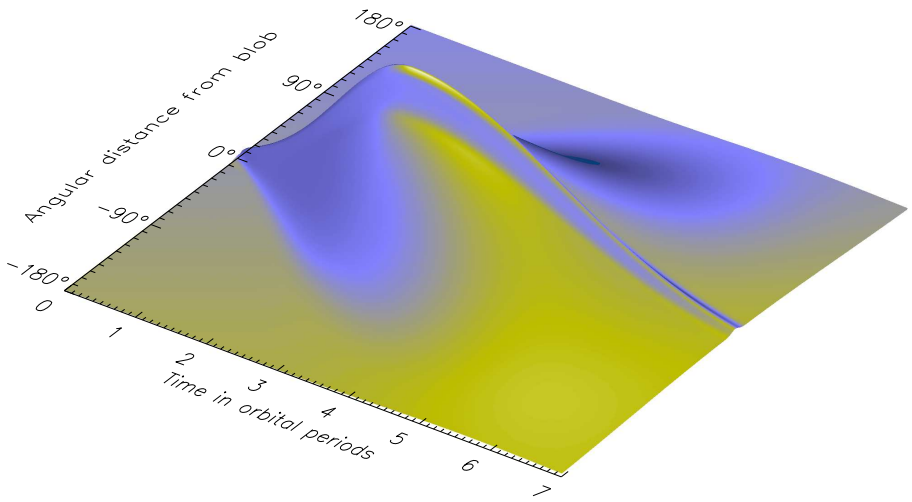

Figure 4.2: Temporal and spatial intrinsic brightness distribution of a blob-arc-model. Model-parameters: $\sigma^{\mathrm{s}}_{\mathrm{rise}} = \sigma^{\mathrm{a}}_{\mathrm{rise}} = 1.1T_{\mathrm{circ}}$, $\sigma^{\mathrm{s}}_{\mathrm{decay}} = \sigma^{\mathrm{a}}_{\mathrm{decay}} = 2.1T_{\mathrm{circ}}$, $k^{\mathrm{s}}_{\mathrm{peak}}/k^{\mathrm{a}}_{\mathrm{peak}} = 1.3$, $T^{\mathrm{s}}_{\mathrm{peak}} = T^{\mathrm{a}}_{\mathrm{peak}} = 2.5T_{\mathrm{circ}}$, $\tau_{\mathrm{shear}} = 1.7T_{\mathrm{circ}}$

4.2.2 Accretion disk

Although there is yet no evidence for a persistent accretion disk around the Galactic black hole, comparison with other galactic nuclei suggests its occurrence. This accretion disk may be fed by infalling clumps of matter once in a while, giving rise to luminous flare events. In our simulation, it can be approximated by a homogeneously radiating ring, spread over the

entire blob-orbit. Its intrinsic brightness can be described by

$$k^{\mathrm{d}} = \begin{cases} k^{\mathrm{d}}_{\mathrm{peak}}\, exp\left(-\frac{1}{2}\left(\frac{T(i)-T^{\mathrm{d}}_{\mathrm{peak}}}{\sigma^{\mathrm{d}}_{\mathrm{rise}}}\right)^2\right) Q(i,j) & \text{, if } T(i) < T^{\mathrm{d}}_{\mathrm{peak}} \\ k^{\mathrm{d}}_{\mathrm{peak}}\, exp\left(-\frac{1}{2}\left(\frac{T(i)-T^{\mathrm{d}}_{\mathrm{peak}}}{\sigma^{\mathrm{d}}_{\mathrm{decay}}}\right)^2\right) Q(i,j) & \text{, if } T(i) > T^{\mathrm{d}}_{\mathrm{peak}} \end{cases} \tag{4.21}$$

with

$$Q(i,j) \equiv \text{const.} \equiv 1 \tag{4.22}$$

Similar to the arc, its temporal brightness evolution can be specified by the parameters $\sigma^{\mathrm{d}}_{\mathrm{rise}}$, $\sigma^{\mathrm{d}}_{\mathrm{decay}}$, $k^{\mathrm{d}}_{\mathrm{peak}}$ and $T^{\mathrm{d}}_{\mathrm{peak}}$. However, the disk's spatial extension is uniform and not changing with time, so it only modulates the contrast of blob and arc.

4.2.3 Gravitational shear

Consider a spherical clump of matter of radius r_{s} without any bonding forces among its constituents, its center revolving a black hole on a stable circular orbit of radius r. Gravitational shear is due to different orbital periods at different radii, so that an extended object in orbit experiences tidal forces. The object's outermost part at $r_{\mathrm{o}} = r + r_{\mathrm{s}}$ has a longer revolving time than its innermost part at $r_{\mathrm{i}} = r - r_{\mathrm{s}}$, which leads to a spreading of the loose matter. A characteristic shear-timescale τ_{shear} is reached when the innermost part "overtakes" the outermost part and thus has completed one more orbit. In terms of the phase angles $\phi_{\mathrm{o}}(t)$ and $\phi_{\mathrm{i}}(t)$ this means:

$$\phi_{\mathrm{i}}(\tau_{\mathrm{shear}}) = \phi_{\mathrm{o}}(\tau_{\mathrm{shear}}) + 2\pi \tag{4.23}$$

and expressed through angular velocities:

$$\omega_{\mathrm{i}}\, \tau_{\mathrm{shear}} = \omega_{\mathrm{o}} \tau_{\mathrm{shear}} + 2\pi \quad \Rightarrow \quad \tau_{\mathrm{shear}} = \frac{2\pi}{\omega_{\mathrm{i}} - \omega_{\mathrm{o}}} \tag{4.24}$$

With equation (2.112) the gravitational shear time τ_{shear} becomes:

$$\tau_{\mathrm{shear}} = \frac{2\pi}{\sqrt{M}} \frac{\left[(r+r_{\mathrm{s}})^{3/2} + a\sqrt{M}\right]\left[(r-r_{\mathrm{s}})^{3/2} + a\sqrt{M}\right]}{(r+r_{\mathrm{s}})^{3/2} - (r-r_{\mathrm{s}})^{3/2}} \tag{4.25}$$

It depends on the orbital radius r, the spin-parameter a and the radius r_{s} of the object (the black hole mass M is constant). Table 4.1 lists the gravitational shear times for all possible grid configurations. Obviously they grow with increasing orbital radius and decreasing black hole spin and range from 8 minutes to more than 10 hours in the case of SgrA*. Table 4.2 contains the corresponding orbital periods of each setup. A graphical representation of Table 4.1 is given in Figure 4.3 and Figure 4.4.

τ_{shear} [min]	$a[M_{\text{SgrA}^\star}]$ 0	0.52	0.7	0.998
$r[r_{\text{LSO}}]$ 1.0	108	48	32	6
1.2	171	74	48	8
1.5	299	127	80	11
2.0	616	256	159	18

τ_{shear} [T_{circ}]	$a[M_{\text{SgrA}^\star}]$ 0	0.52	0.7	0.998
$r[r_{\text{LSO}}]$ 1.0	4.0	2.9	2.5	1.4
1.2	4.8	3.4	2.9	1.5
1.5	6.0	4.3	3.6	1.7
2.0	8.0	5.6	4.7	2.0

Table 4.1: Gravitational shear times τ_{shear} in minutes (left) and in terms of the orbital period (right) for an object radius of $0.25R_s$ for different orbital radii and black hole spins.

T_{circ} [min]	$a[M_{\text{SgrA}^\star}]$ 0	0.52	0.7	0.998
$r[r_{\text{LSO}}]$ 1.0	27.3	16.7	12.9	4.4
1.2	35.9	21.6	16.6	5.2
1.5	50.1	29.9	22.6	6.5
2.0	77.2	45.4	34.1	9.1

Table 4.2: Orbital periods T_{circ} of the blob-center in minutes (coordinate time) for different orbital radii and black hole spins.

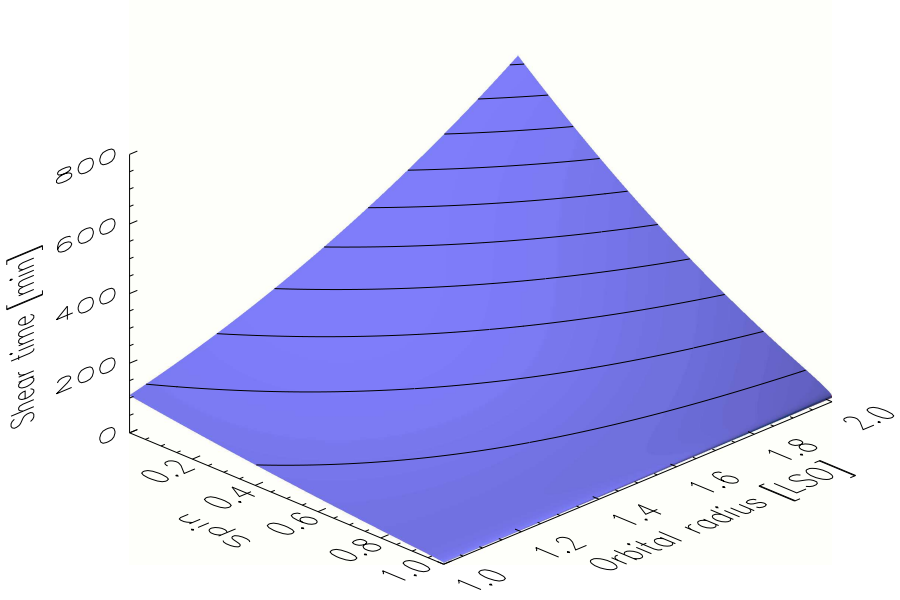

Figure 4.3: Dependency of the gravitational shear time τ_{shear} on the spin-parameter $a[M_{\text{SgrA}^\star}]$ and the orbital radius r in units of the last stable orbit radius. For every multiple of 60min a contour line is drawn.

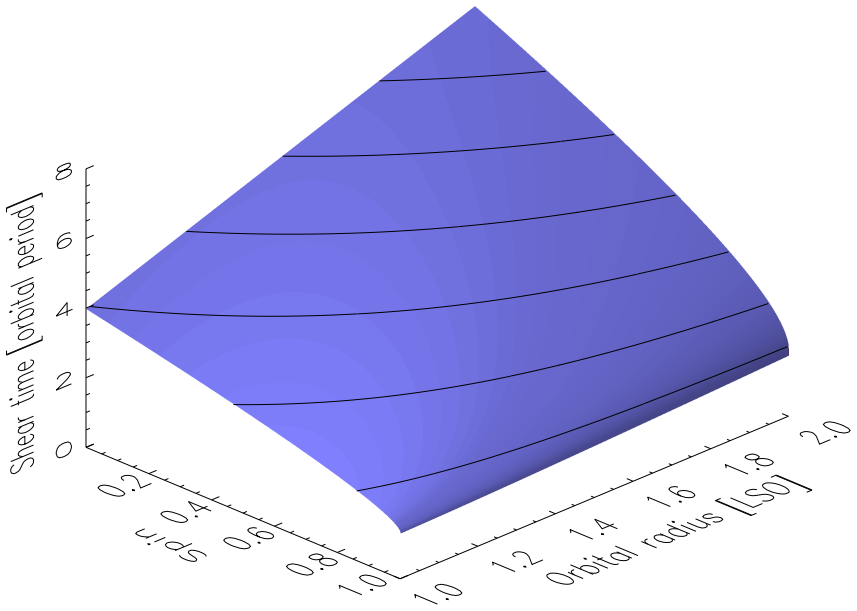

Figure 4.4: Dependency of the gravitational shear time τ_{shear} in units of the orbital period T_{circ} on the spin-parameter $a[M_{\text{SgrA}^\star}]$ and the orbital radius r in units of the last stable orbit radius. For every multiple of one orbital period a contour line is drawn.

4.2.4 Magnetohydrodynamic shear

The crucial assumption for considering gravitational shear is to neglect any bonding forces within the plasma around the black hole. However, a strong magnetic field is likely to be present and may prevent hot spots from shearing on the Kepler-timescale.

The characteristic shear-timescale of such a scenario is increasing with higher magnetic field strengths. This is due to a so called *magneto-rotational instability* (MRI), discovered by Balbus and Hawley in 1991 [1]. It acts against the tidal forces caused by the gravitational field and creates an attractive force among adjacent elements of the accretion disk, trying to enforce a rigid rotation. In Figure 4.5 this force is visualized by a spring.

Thus, in the case of a very strong magnetic field, the hot spot can be regarded as a rigid source, retaining its shape during the whole duration of a flare. In this limit the shear time can be approximated to be infinite.

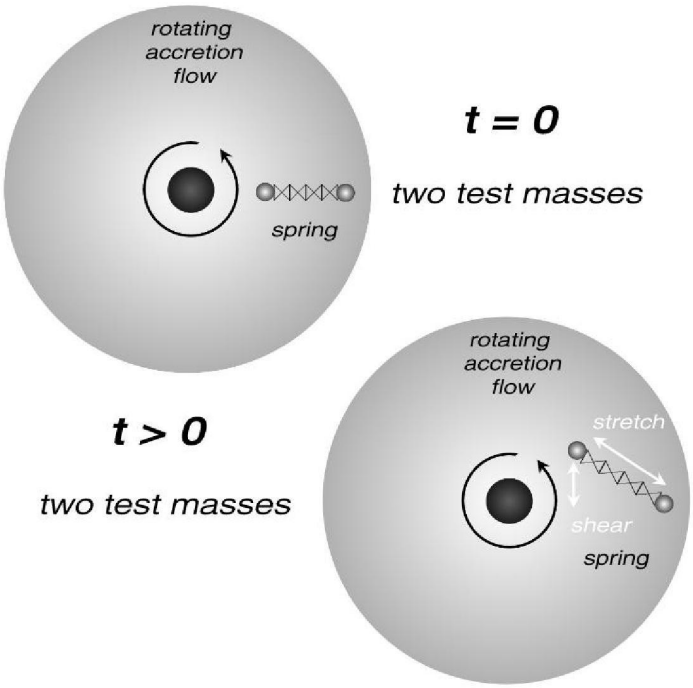

Figure 4.5: Illustration of the magneto-rotational instability of a magnetized accretion disk around a rotating black hole (from [27]).

Chapter 5

Modeling flares from SgrA*

The code developed above allows us to study the influences of various parameters on the simulated light curves and centroid tracks. We will start simulating a simple light source to analyze how the different relativistic effects are revealed in the data. Hereafter more realistic models will be discussed and checked against real observations.

5.1 Compact blob-model

In order to study only relativistic effects it is most convenient to set up a light source as simple as possible. To this effect we will simulate a single blob without any spatial elongation or intrinsic temporal evolution. Thus, it is sufficient to only compute one full orbit in a given configuration. The simulation parameters for the realization of this scenario are:

$$\sigma^{\mathrm{s}}_{\mathrm{rise}} = \sigma^{\mathrm{s}}_{\mathrm{decay}} = \infty,\ k^{\mathrm{s}}_{\mathrm{peak}} = 1,\ k^{\mathrm{a}}_{\mathrm{peak}} = 0,\ T^{\mathrm{s}}_{\mathrm{peak}} = 0,\ \alpha^{\mathrm{s}} = 0 \tag{5.1}$$

By setting $k^{\mathrm{a}}_{\mathrm{peak}} = 0$ we simply " switch off " the arc, that's why we don't have to specify the other parameters concerning it.

For the mass and distance of the black hole we will use the values of the Galactic Center black hole given in the introduction in order to produce realistic data comparable to observations.

5.1.1 Photometry

Let us first focus on the light curves. In a classical situation we would expect a constant light curve throughout the whole orbital period, since the brightness of a constant light source on a Keplerian orbit should not depend on time. In a highly relativistic regime though, Doppler- and beaming-effects make the apparent brightness of the source depend on its relative velocity to the observer. Since it moves on a circular orbit, the light curves are modulated with a sine-pattern. But due to the fact that the hot spot moves with

velocities close to the speed of light, the relativistic Doppler effect makes it appear slower when it is receding, and faster when it is approaching the observer. This stretches the sine-pattern around its minimum and compresses it around its maximum. Furthermore, the bending of light rays produces multiple images of the source in different locations, leading to a substructure in the light curves.

Below we investigate in detail how the shape of the curves depends on changes in the basic parameters of the model. We normalize each light curve to its minimum flux and plot it against the orbital phase in radiants (zero designates the point where the hot spot is closest to the observer). This representation is quite suitable for the comparison of the curves, since it scales them to the same length and provides an easy way to read off the amplification of flux from minimum to maximum.

Orbital radius and inclination

Figure 5.1 displays light curves of hot spot orbits with different orbital radii and inclinations around a Schwarzschild black hole (details are given in the figure caption). Obviously, decreasing the orbital radius generally leads to narrower and higher peaks. This is due to the increasing spot-velocity leading to stronger relativistic Doppler- and beaming-effects, respectively.

The same changes can be produced by increasing the inclination of the orbit, since this increases the line of sight velocity of the hot spot (both relativistic Doppler- and beaming-effects depend on the line of sight velocity $v \cos \vartheta$, see section 2.1). In our range for the parameters, changes in the inclination indicate these relativistic effects even stronger than changes in the orbital radius.

Furthermore, the light curves with 90° inclination reveal an additional feature. Before each light curve reaches its usual peak-maximum, a spiky second peak appears. Its peak-flux exceeds the latter's by far. It originates from the development of an *Einstein ring*, an apparent ring-shaped image of the hot spot around the black hole. It occurs, when the light source, the black hole and the observer are aligned (and the black hole is in between). In this axially symmetric geometry, the lengths of the light paths between source and observer are rotationally invariant with respect to the line of sight. Hence, the observer receives a rotationally symmetric image and the total observed flux is increased significantly.

Higher order Einstein rings appear, when light rays revolve the black hole. For instance, the secondary Einstein ring appears, when the hot spot passes in front of the black hole. We then receive photons from the far side of the spot that revolved the black hole once. Actually it occurs a bit later, since one still has to consider the finite speed of light on its way round the black hole. The corresponding peaks can also be seen in the last plot of Figure 5.1, although they are a lot smaller than the ones created by the

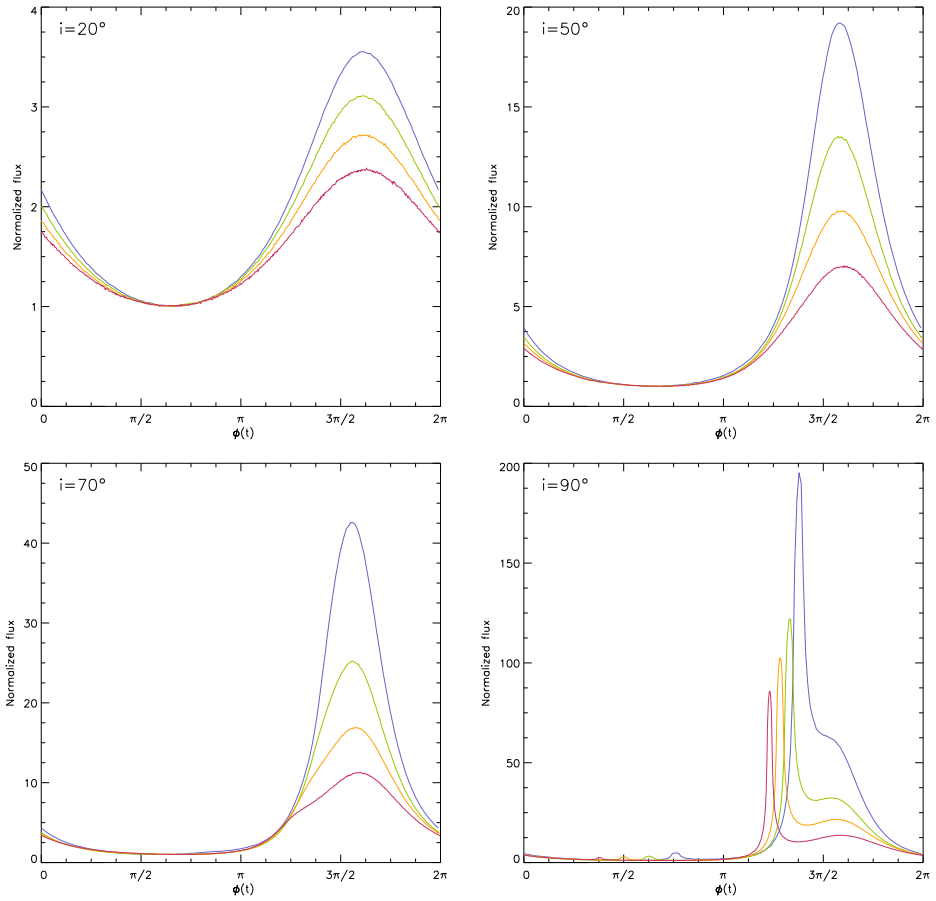

Figure 5.1: Light curves of a compact hot spot orbiting a Schwarzschild black hole in different orbital radii and inclinations. Colors indicate the orbital radius (blue: $1.0r_{\mathrm{LSO}}$, green: $1.2r_{\mathrm{LSO}}$, yellow: $1.5r_{\mathrm{LSO}}$, red: $2.0r_{\mathrm{LSO}}$).

primary Einstein ring.

It is interesting to see how the occurrence of the Einstein rings depends on the orbital radius of the spot. At larger radii, the primary Einstein ring emerges at a smaller orbital phase. This is again due to the relativistic Doppler effect, that makes the light source appear slower on the receding side. If it is strong, the Einstein ring is more delayed. The occurrence of the secondary Einstein ring is determined by two counteracting effects: the travel time of the light rays revolving around the black hole grows with higher orbital radii, but so does the orbital period. The latter effect dominates and therefore the secondary Einstein ring appears at lower orbital phases with increasing radii.

Figure 5.2 shows simulated images of a primary and a secondary Einstein ring for a compact hot spot on the last stable orbit. The secondary ring is

very dim and can just be resolved in the used pixelscale.

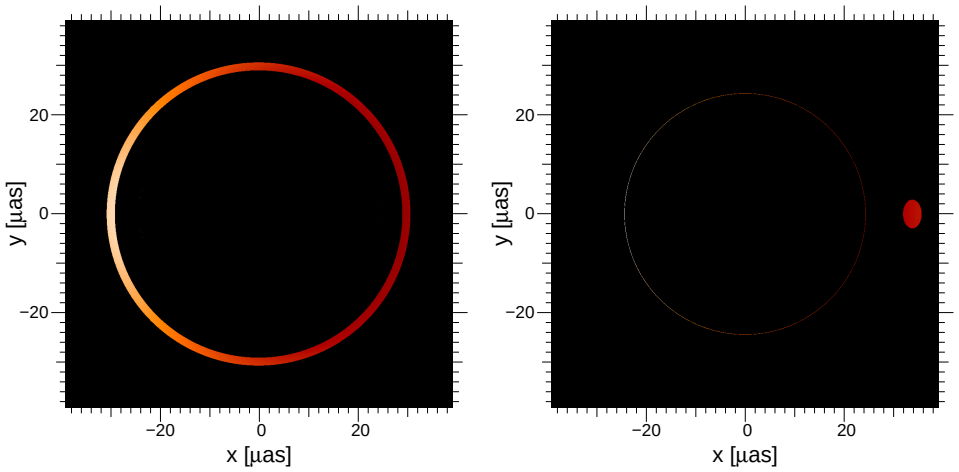

Figure 5.2: Primary and secondary Einstein ring of a compact hot spot orbiting a Schwarzschild black hole on the last stable orbit in 90° inclination.

If we go back to lower inclinations, we expect no Einstein rings, but still multiple images of the hot spot. Obviously, their effects on the light curves are marginal. Only the light curves with 70° inclination show a slight distortion of the main peak, suggesting the existence of a secondary image. It is not only the small size that prevents the secondary image from being observable in the light curves, but also the fact that its brightness is not as variable as the Einstein ring's.

Spin

Now that we know that relativistic effects show up most strongly at 90° inclination, we will investigate the impact of different black hole spins on such a configuration. Figure 5.3 displays the corresponding light curves for various spin-parameters. A logarithmic representation (in magnitudes) emphasizes the fainter parts of the light curves more strongly. Here, one can even see another peak, corresponding to the tertiary Einstein ring. The main differences between the curves is due to the fact that the last stable orbit shrinks with higher spin-parameters. Thus, they change in the same way as before, when we changed the orbital radius.

By looking more closely to the Einstein ring peaks, one can find a slight broadening with higher spin. This is due to the fact that the blob occupies a bigger fraction of the orbit at smaller radii. The result is that the required conditions for an Einstein ring are met for a larger orbital phase. It is hard to tell, whether there is another effect solely caused by the black hole spin. By all means its influence on the light curve shapes is marginal.

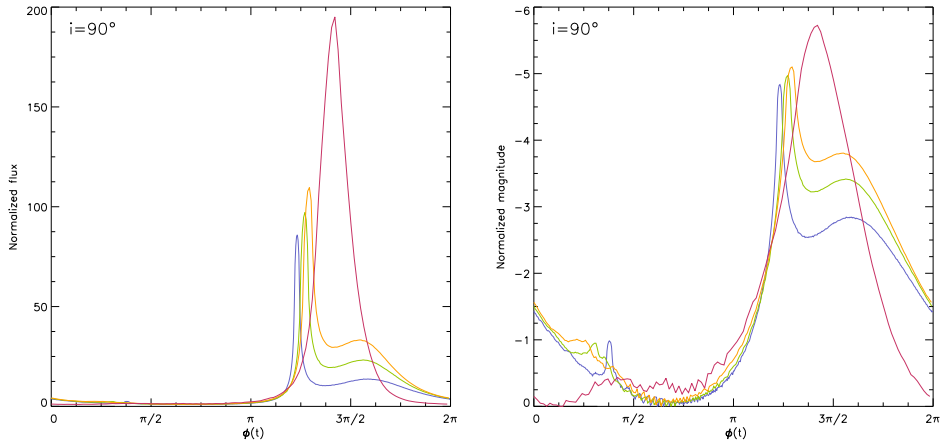

Figure 5.3: Light curves of a compact hot spot orbiting a Schwarzschild black hole (blue), a Kerr black hole with $a = 0.52M$ (green), $a = 0.7M$ (yellow) and $a = 0.998M$ (red) in 90° inclination with an orbital radius of $2r_{\mathrm{LSO}}$. The plot to the right shows the normalized magnitude of the light curves to the left ($m := -2.5 \log_{10} \overline{S_o}$).

Spectral index

Changing the SED of the hot spot emission has strong implications on the light curves as well. Since we're observing in a confined range of frequencies (observing band), Doppler shifting the emitted radiation makes us observe different parts of the SED every instant of time. If, for instance, the hot spot is approaching us, the observed radiation is blue-shifted. In the rest frame of the blob, though, this radiation was emitted at lower frequencies. Depending whether the hot spot emission follows a blue, white or red SED, the observed flux is lower, equal or higher, respectively. This means that a red SED ($\alpha^{\mathrm{s}} < 0$) amplifies the beaming effect by brightening the hot spot on the approaching side and dimming it on the receding side, while a source with a blue SED ($\alpha^{\mathrm{s}} > 0$) behaves contrariwise. A white or constant SED ($\alpha^{\mathrm{s}} = 0$) does not affect the observed flux at all.

Figure 5.4 displays light curves for all three cases. Clearly, the peaks broaden with increasing spectral index. In higher inclinations (right plot) the effect of the spectral index gets stronger. One can see that in the case of a blue SED the observed flux of the hot spot at the approaching side is dimmed so strongly, that the secondary image of the blob is revealed. Its flux exceeds the brightness of the primary image for a short fraction of the orbital period. In the case of a red SED the opposite happens: the primary peak gets so narrow and bright, that the secondary peak appears before.

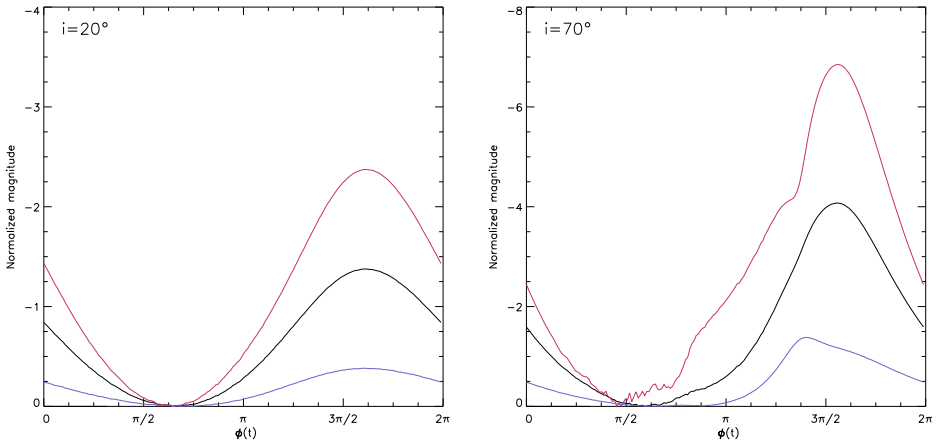

Figure 5.4: Light curves (in magnitudes) of a compact hot spot orbiting a Schwarzschild black hole on the last stable orbit in 20° and 70° inclination. Each plot shows light curves for three different spectral indices of the emitted hot spot SED with $\alpha^{\mathrm{s}} = 0$ (black), $\alpha^{\mathrm{s}} = -3$ (red), $\alpha^{\mathrm{s}} = 3$ (blue).

5.1.2 Astrometry

The centroid tracks of our simplified hot spot model provide further information on its configuration. In the following, the same parameters as above will be varied and their impact analyzed.

Orbital radius and inclination

Obviously, decreasing the orbital radius leads to smaller centroid tracks, as can be seen in Figure 5.5. Then, just as with the light curves, the relativistic effects increase, i.e. the deviation of the centroid tracks from the classical ones (dashed lines) gets bigger. On the one hand, this deviation is caused by multiple images of the hot spot. When the secondary image gets brightest, the centroid of the received light lies somewhere in between the primary and the secondary image. But since the latter only brightens up shortly (it moves faster on the approaching side), this causes a cusp in the centroid track. On the other hand, deflection of the primary rays distorts the centroid track as well. The rear part of the orbit appears to be folded upwards in higher inclinations.

Like before, raising the inclination leads to stronger relativistic effects. The cusp in the centroid track, for instance, becomes more and more prominent. Since the centroid track for the 90° case is just a horizontal line, we instead plot the orbital phase $\phi(t)$ against $x(t)$, as shown in the last plot of Figure 5.5. First, one can see how the classical sine-pattern is deformed due to the relativistic Doppler effect, as discussed above. Second, distinct spikes appear in the pattern. These can be associated with the Einstein rings.

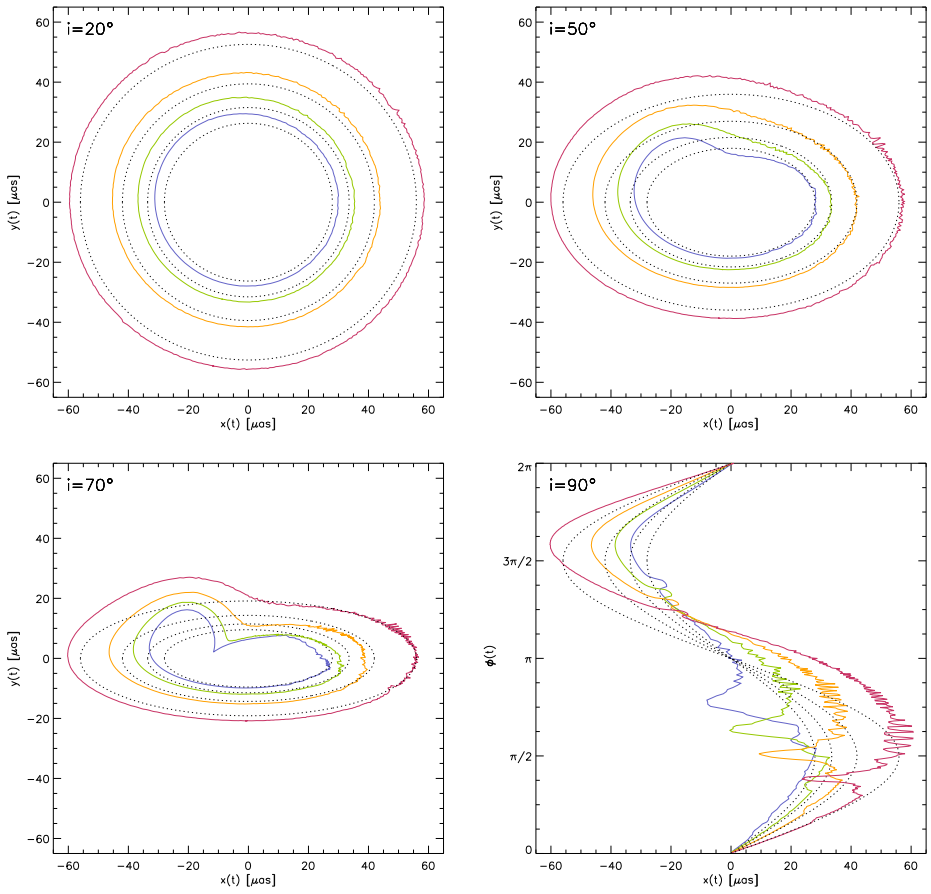

Figure 5.5: Centroid tracks of a compact hot spot orbiting a Schwarzschild black hole in different orbital radii and inclinations. Colors indicate the orbital radius (blue: $1.0r_{\mathrm{LSO}}$, green: $1.2r_{\mathrm{LSO}}$, yellow: $1.5r_{\mathrm{LSO}}$, red: $2.0r_{\mathrm{LSO}}$). The dashed lines indicate the classical behavior neglecting any relativistic effects.

Comparing the occurrence of these spikes with the occurrence of the sub-peaks in the light curves, one can ascertain that they appear at the same orbital phase for a given configuration. Thus, the first spike (in the first half of the orbital period) corresponds to the secondary Einstein ring and the second spike (in the second half of the orbital period) corresponds to the primary Einstein ring.

The jitter of the curve at the receding side is due to the limited resolution of the ray traced images. It starts, when a secondary image of the blob appears at the approaching side. Because it only consists of a few bright pixels, the location of the centroid is highly sensitive on changes in the number of integrated pixels.

Spin

Higher spin makes the last stable orbit shrink. Thereby the centroid tracks deform even stronger, i.e. the cusp develops more strongly and the rear part of the orbit is dragged up further. In addition, a second cusp emerges on the receding side, due to the tertiary image of the spot. The cusps may even turn into loops provided the multiple images are bright enough, as apparent from the left plot in Figure 5.6.

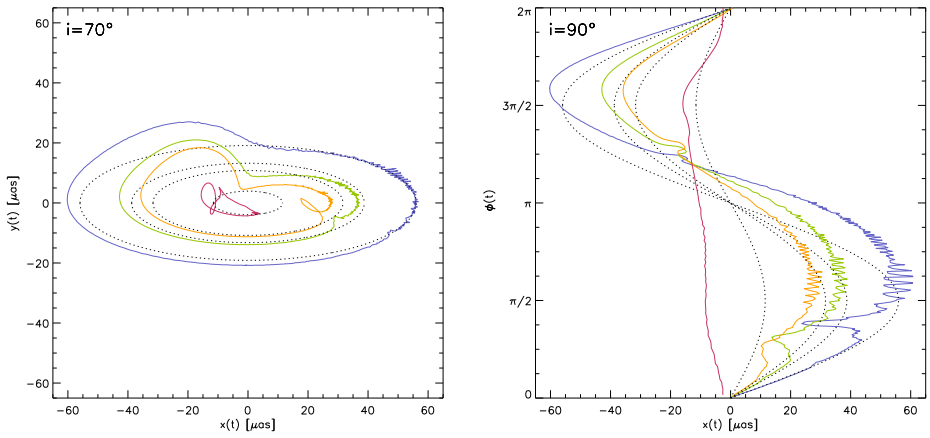

Figure 5.6: Centroid tracks of a compact hot spot orbiting a Schwarzschild black hole (blue), a Kerr black hole with $a = 0.52M$ (green), $a = 0.7M$ (yellow) and $a = 0.998M$ (red) in 70° and 90° inclination with an orbital radius of $2r_{\mathrm{LSO}}$. The dashed lines indicate the classical behavior neglecting any relativistic effects.

The right plot shows the 90° case. Just like the sub-peaks in the light curves, the spikes in the deformed sine-pattern are broadened with higher spin-parameters of the black hole. In the high-spin case the secondary Einstein ring even dominates throughout the entire first half of the orbital motion. Thereby it shrouds the motion of the hot spot almost completely.

Spectral index

As the light curves have shown, the slope of the hot spot SED may either intensify (red spectrum) or attenuate (blue spectrum) the relativistic beaming effect. In Figure 5.7 it appears that the centroid tracks with a red spectrum are dragged towards the approaching side, whereas the one's with a blue spectrum towards the receding side. The multiple images have a greater influence on the shape of the centroid track in the case of a red SED, since the primary image of the hot spot is dimmed stronger on the receding side of the orbit, whereas the secondary image is amplified stronger on the approaching side.

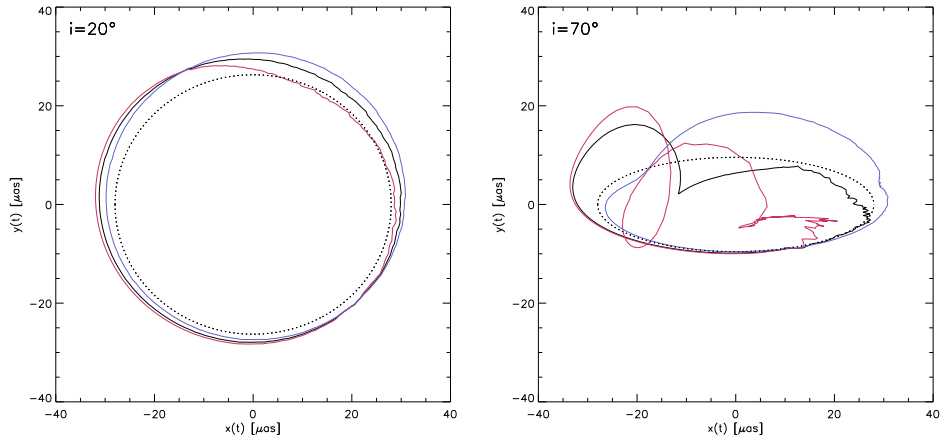

Figure 5.7: Centroid tracks of a compact hot spot orbiting a Schwarzschild black hole on the last stable orbit in 20° and 70° inclination. Each plot shows centroid tracks for three different spectral indices of the emitted hot spot SED with $\alpha^{\mathrm{s}} = 0$ (black), $\alpha^{\mathrm{s}} = -3$ (red), $\alpha^{\mathrm{s}} = 3$ (blue).

5.1.3 Combination of photometry and astrometry

Light curves and centroid tracks comprise complementary information on the configuration of the considered system. It is therefore possible to break degeneracies in some of the parameters of the model by regarding both photometric and astrometric information.

For example, one can compare the flux-amplification in the light curves with the diameter of the centroid tracks. Since both properties depend on the inclination, the orbital radius and the spin-parameter of the configuration, they are suitable for this kind of analysis. The *amplification* A is defined as the difference between the apparent magnitudes of the light curve's maximum and minimum within one orbital period:

$$A := |m^{\max} - m^{\min}| = 2.5 \log_{10} \left(\frac{\overline{S_o}^{\max}}{\overline{S_o}^{\min}} \right) \tag{5.2}$$

In Figure 5.8 the amplification of each light curve is plotted against the horizontal diameter of the corresponding centroid track for each grid-configuration. Obviously, in such a representation it is possible to distinguish every single configuration by the set of parameters $\{r, i, a, T_{\mathrm{circ}}\}$. This is because the inclination mainly influences the light curve peaks and does not change the horizontal centroid deflection so much, whereas the orbital radius has a stronger influence on the centroid deflection than on the light curves. Changing the spin-parameter of the black hole has no big effect on either the amplification or the diameter of the centroid track. Configurations with the same location in this plot (i.e. same orbital radius and inclination) can

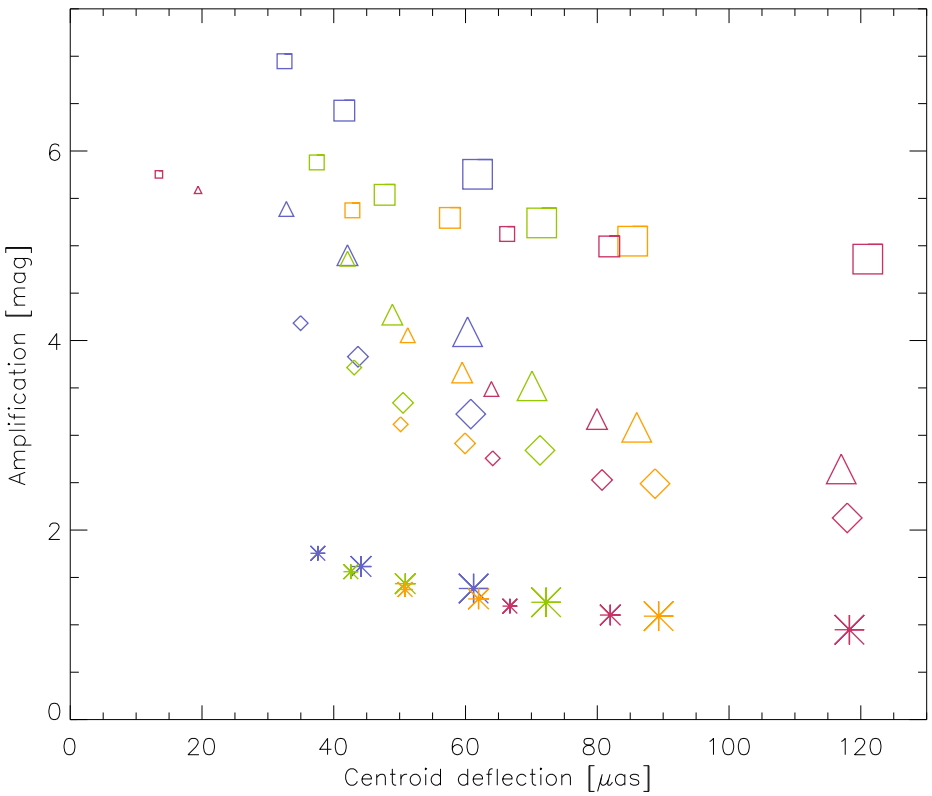

Figure 5.8: Amplification of the light curve in magnitudes plotted against the horizontal diameter of the centroid track in μas for each grid-configuration in the compact blob-model. The symbol-shape indicates different inclinations (star: 20°, diamond: 50°, triangle: 70°, square: 90°). Colors indicate the orbital radius (blue: $1.0r_{\mathrm{LSO}}$, green: $1.2r_{\mathrm{LSO}}$, yellow: $1.5r_{\mathrm{LSO}}$, red: $2.0r_{\mathrm{LSO}}$). The symbol-size indicates the spin-parameter (big: $a = 0$, medium: $a = 0.52M$, small: $a = 0.7M$, tiny: $a = 0.998M$).

be distinguished by their orbital period that can be taken from the light curves. Then, the spin-parameter is determined via equation (2.113).

Thus, obtaining astrometric data from SgrA⋆ could on the one hand help to verify the hot spot model and constrain its properties, especially the spin of the black hole. On the other hand though, the new data could rule out the hot spot model and favor other scenarios instead.

5.1.4 Multiple blobs

The simple model of a single compact light source can be easily extended by adding further blobs on the same orbit. On average, flares occur once a day, so it is not unlikely that two flare events may sometimes coincide. As a result one would expect the light curve to contain two sequences of major

peaks, displaced according to the separation of the two blobs.

In the special case of a separation of half an orbital phase one would expect the light curve to show twice the frequency in the oscillations compared to the single blob case. Hence, it might be hard to distinguish between a single blob on a close orbit with orbital period T_{circ} and two blobs on farther orbits with each an orbital period of $2T_{\mathrm{circ}}$. In both cases the resulting light curves would show a periodicity of T_{circ}.

Figure 5.9 demonstrates the two cases showing the corresponding light curves (again normalized to the minimum flux) and centroid tracks for a particular configuration. Obviously, the two blobs create far weaker and broader oscillations than the single one. Say we assumed the two-blob light curve to be caused by a single blob on a closer orbit around the black hole. We then have to stretch the first half of the corresponding light curve to the full orbital phase. Thus, the resulting light curve would peak earlier than the real single-blob light curve and show a far broader modulation.

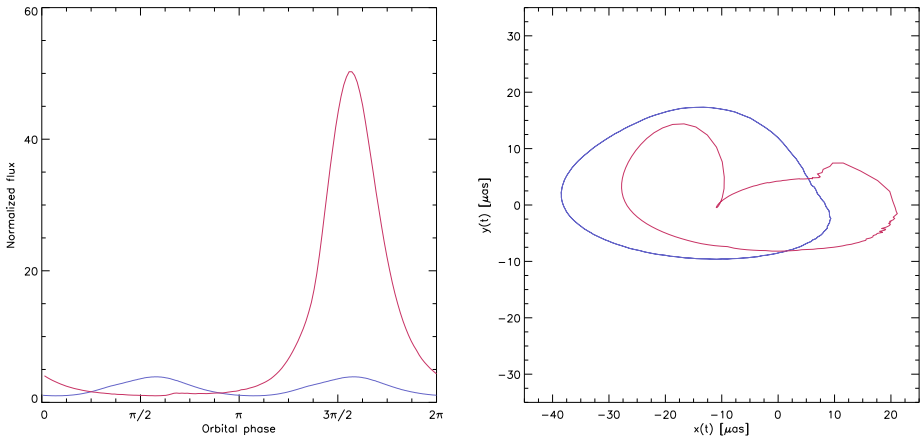

Figure 5.9: Light curves (left) and centroid tracks (right) of one blob (red, $r = 1.2r_{\mathrm{LSO}}$) and two oppositely situated blobs (blue, $r = 2.0r_{\mathrm{LSO}}$) orbiting a Kerr black hole with $a = 0.52M$ in 70° inclination.

Also the shapes of the centroid tracks suggest how to discriminate the two models. Although one might naively expect the centroid track in the two-blob case to degenerate into a single spot, this is not the case due to relativity. The relativistic Doppler effect causes the two blobs to never appear equally fast because of their opposite line of sight velocities. Thus, most of the time the blobs are seen on the receding side, separated by less than half an orbital phase (see Figure 5.10). Nevertheless the resulting centroid motion is dragged further to the approaching side due to relativistic beaming.

Multiple images play a minor role, because their brightness is always outreached by the one blob closest to the approaching side. This makes the

cusp in the centroid track almost disappear.

In general one can say that relativistic effects are suppressed in the case of two oppositely situated sources. Yet it might be hard to discriminate between one and two blobs in a real observation.

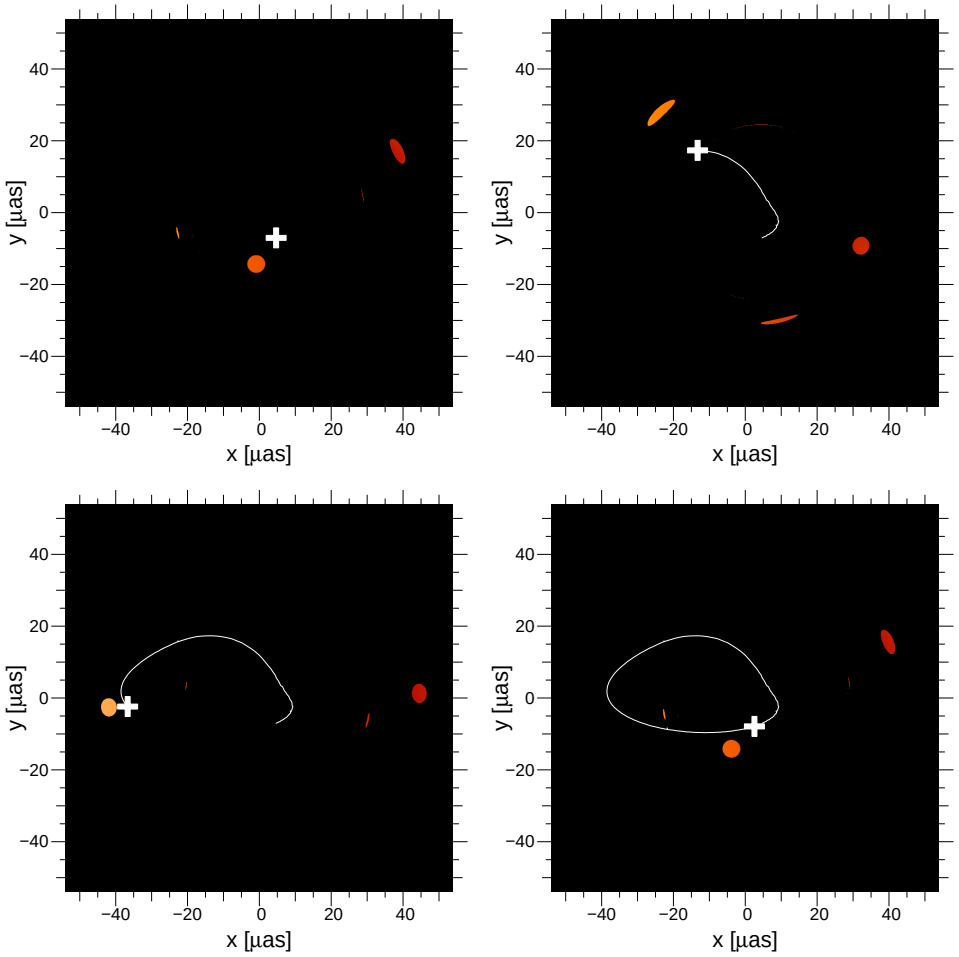

Figure 5.10: Sequence of two blobs orbiting a Kerr black hole with $a = 0.52 M_{\mathrm{SgrA}^\star}$ in 70° inclination and $2.0 r_{\mathrm{LSO}}$ distance, separated by half an orbital perimeter. The images are taken roughly every 7.5 minutes as measured by a distant observer, showing half an orbital period of each blob. The white cross marks the centroid of the particular image and leaves a trace of its previous motion.

5.2 Shearing blob-arc-model

The conception of a single compact object revolving a supermassive black hole in its closest vicinity, maintaining a constant shape and brightness is somewhat artificial and has presumably little physical relevance. In order to

improve this model we will additionally implement an elongated arc, which is spreading from the blob due to gravitational shear. Both components (blob and arc) will furthermore vary their intrinsic brightness with time to emulate heating and cooling sequences.

The timescales for these processes is determined by the *synchrotron cooling time* τ_{syn}, which depends on the magnetic field strength B and the wavelength λ of the observed synchrotron radiation. For the case of SgrA* it is estimated as [20]:

$$\tau_{\mathrm{syn}} \approx 8\,(B/30\mathrm{Gauss})^{-3/2}\,(\lambda/2\mu\mathrm{m})^{1/2}\,\mathrm{min} \tag{5.3}$$

Computational models in *general relativistic magnetohydrodynamics* (GRMHD) suggest that in the close vicinity of a Kerr black hole the magnetic field strength within the accretion disk decreases with radial distance. In contrast, higher spin-parameters lead to stronger magnetic fields [9]. These dependencies are fairly complicated and presumably cannot be derived analytically. Since a full GRMHD-simulation exceeds the scope of this work, we will determine the heating and cooling timescales from the observations.

From the flare light curves one can estimate these parameters to be of the order of the orbital timescale, i.e. the temporal separation between two successive major peaks. The decaying edge of the flare usually turns out to be wider than the rising one. For these reasons we fix the rise- and decay-times of blob and arc to the following values:

$$\sigma^{\mathrm{s}}_{\mathrm{rise}} = \sigma^{\mathrm{a}}_{\mathrm{rise}} = T_{\mathrm{circ}} \quad , \quad \sigma^{\mathrm{s}}_{\mathrm{decay}} = \sigma^{\mathrm{a}}_{\mathrm{decay}} = 2T_{\mathrm{circ}} \tag{5.4}$$

The exact values for these parameters vary from flare to flare and may deviate from the ones above, but since we're only modeling the flares qualitatively in this section, they are reasonable. The same holds for the peak-flux ratio of blob and arc. We use

$$k^{\mathrm{s}}_{\mathrm{peak}}/k^{\mathrm{a}}_{\mathrm{peak}} = 4/1 \tag{5.5}$$

which means the blob is five times as bright as the arc, since the arc-brightness is also added at the location of the blob. The total number of orbits and the location of the flux-maxima of blob and arc are chosen to be:

$$n = 6 \quad , \quad T^{\mathrm{s}}_{\mathrm{peak}} = T^{\mathrm{a}}_{\mathrm{peak}} = 2T_{\mathrm{circ}} \tag{5.6}$$

The shear time τ_{shear} is determined by equation (4.25), since we're assuming purely gravitational shear. τ_{shear} is shortest for small orbital radii and high black hole spins, i.e. the effect of shear is strongest in these configurations.

Now, only the spectral indices of blob and arc remain to be specified. Observations from the flares in the Galactic Center suggest a connection between brightness and color. In times where the flare is dim it shows a

red spectrum, whereas in bright states it is rather white [20]. Since in our model the blob is brighter than the arc, motivated by the observations, we use the following values:

$$\alpha^{\mathrm{s}} = 0 \quad , \quad \alpha^{\mathrm{a}} = -3 \tag{5.7}$$

With this set of parameters we simulate all the grid-configurations and investigate the impacts of the grid-parameters on light curves and centroid tracks, respectively.

5.2.1 Photometry

In contrast to the previous model, now the shape of the major peaks in the light curves is changing with time. While the first peaks may be similar to the ones already discussed in the last section, the later ones differ strongly. This is due to the fact that in the beginning of the simulation we start with a compact blob, which is then spreading into an arc along the orbit. The degree of deformation depends on the shear time.

Light curves for various configurations are presented below. As before, the abscissa shows the orbital phase in radiants and the ordinate is normalized to the minimum flux.

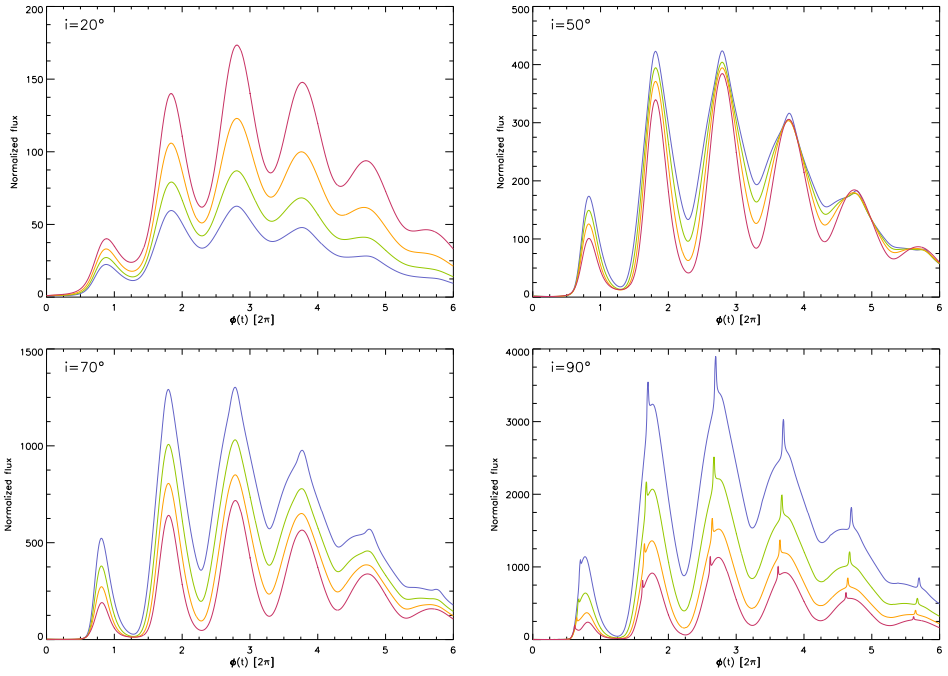

Figure 5.11: Light curves of the shearing blob-arc-model for different orbital radii and inclinations in the case of a Schwarzschild black hole. Colors indicate the orbital radius (blue: $1.0r_{\mathrm{LSO}}$, green: $1.2r_{\mathrm{LSO}}$, yellow: $1.5r_{\mathrm{LSO}}$, red: $2.0r_{\mathrm{LSO}}$).

Orbital radius and inclination

Figure 5.11 displays light curves with different orbital radii and inclinations. The first orbital period shows a similar behavior as in the compact blob-model. The peak-modulations are stronger for lower orbital radii and higher inclinations, for reasons discussed above (at low inclination and high orbital radii the arc occupies a significantly larger area on sky, in this case the total flux is rising with the orbital radius). This feature is continuously reversed in the subsequent peaks, due to faster shear at lower radii. While for $r = 2.0r_{\mathrm{LSO}}$ there are still distinct peaks after four orbital periods, for $r = 1.0r_{\mathrm{LSO}}$ the modulations become very weak and even may reveal a more narrow peak caused by the compact blob.

In the case of 90° inclination the sub-peaks associated with the Einstein rings evolve similarly. Note, that the major peaks tend to move towards the sub-peaks during the flare, i.e. they peak earlier every following orbital period. This is caused by the rise and decay of the arc-brightness, superimposed on the orbital variations.

Spin

Finding imprints of the black hole spin in the light curves becomes even harder in this model. As we have seen in the last section, higher spin-parameters cause the Einstein ring peaks to broaden slightly. Since higher spin means smaller orbital radii and thus stronger shear, the broadening is not solely due to the latter effect, but also due to gravitational shear. Hence, it is hard to disentangle between these two processes.

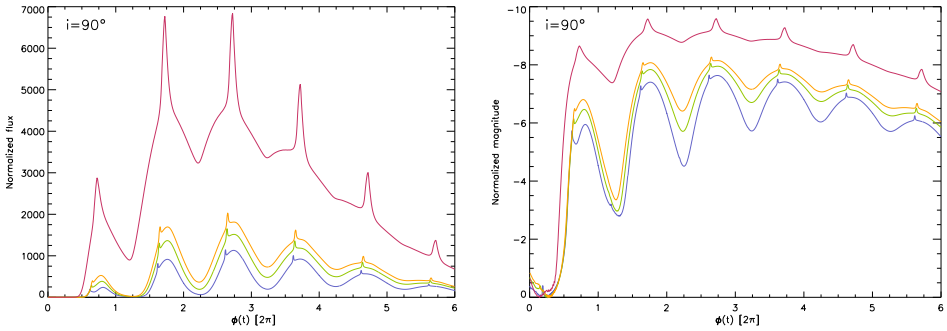

Figure 5.12: Light curves of the shearing blob-arc-model with 90° inclination and an orbital radius of $2r_{\mathrm{LSO}}$ for different black hole spins. Colors indicate the spin-parameter: Schwarzschild (blue), Kerr with $a = 0.52M$ (green), $a = 0.7M$ (yellow) and $a = 0.998M$ (red). The plot to the right shows the normalized magnitude of the light curves to the left ($m := -2.5 \log_{10} \overline{S_o}$).

Figure 5.12 shows four light curves with each different black hole spins. Even in the logarithmic representation one can hardly find the secondary

Einstein ring peaks. As soon as the arc has developed, most of the substructure in the light curves is suppressed.

5.2.2 Astrometry

The motion of the centroid does not result in a closed curve in the shearing blob-arc-model anymore. Due to the extension of the light source it tends to converge to a single point, producing a spiral centroid track. As for the light curves, gravitational shear dilutes the relativistic effects gradually.

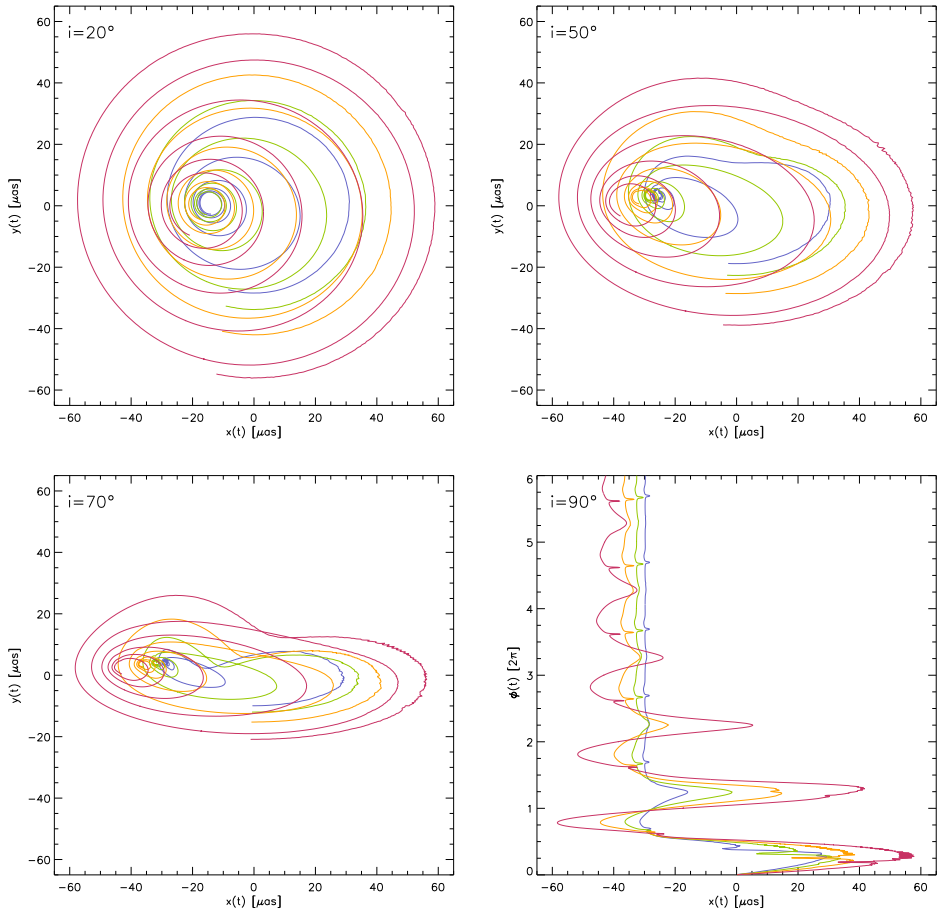

Figure 5.13: Centroid tracks of the shearing blob-arc-model in different orbital radii and inclinations in the case of a Schwarzschild black hole. Colors indicate the orbital radius (blue: $1.0r_{\mathrm{LSO}}$, green: $1.2r_{\mathrm{LSO}}$, yellow: $1.5r_{\mathrm{LSO}}$, red: $2.0r_{\mathrm{LSO}}$).

Orbital radius and inclination

In Figure 5.13 one can see how the cusp, associated with the secondary image of the source, fades away with every new orbital period. As the light distribution spreads out, the contribution of the higher order images to the total flux becomes negligible.

Classically, the centroid would converge to the center of the image, but due to relativistic beaming, the point of convergence is shifted to the approaching side. It moves further with increasing inclination due to stronger beaming. The same happens with growing orbital radius, although beaming decreases. At higher radii this trend would reverse and the point of convergence would approach the center. One can already see that in the cases of high orbital radius, the spiral becomes more and more symmetric.

Spin

Apart from gaining a lower limit for the spin-parameter from the diameter of the centroid tracks, any signature of the black hole spin is again very hard to find, even in the centroid motion. In order to see some effects it is important to look at the very beginning of the flare before the shear smears the centroid track.

As shown in Figure 5.14, in the high spin case, the centroid converges quickest. Unfortunately, most of the relativistic effects can only be observed in the first orbital motion. This fact imposes high demands on observational instruments that aim at performing such measurements, because they have to be operational immediately when the flare starts.

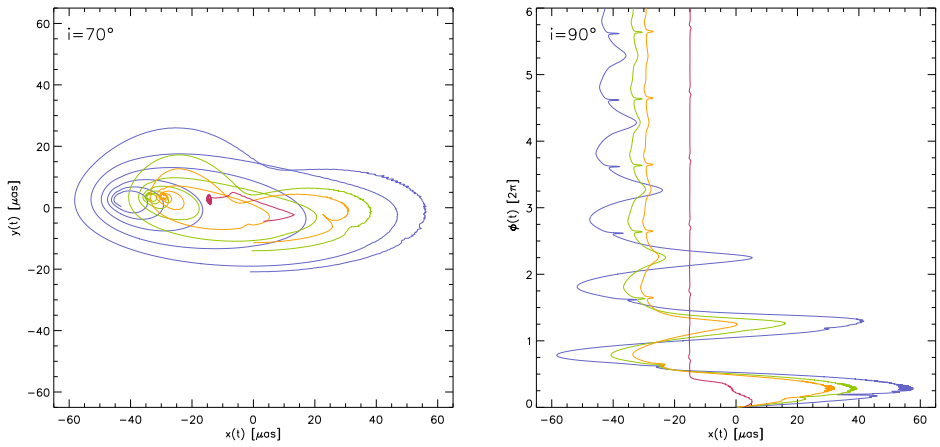

Figure 5.14: Centroid tracks of the shearing blob-arc-model with 70° and 90° inclination and an orbital radius of $2r_{\mathrm{LSO}}$ for different black hole spins. Colors indicate the spin-parameter: Schwarzschild (blue), Kerr with $a = 0.52M$ (green), $a = 0.7M$ (yellow) and $a = 0.998M$ (red).

5.3 Fitting observational data

The developed model for the possible origin of the flares from SgrA⋆ is now ready to be tested. This means one can try to arrange its parameters in such a way that it reproduces the observational data. A fit of the simulated light curves to the observed ones will help to determine these parameters and provide theoretical predictions for future measurements.

5.3.1 Approach

Due to the complexity of the model and its numerous degrees of freedom it does not make any sense to implement a fitting routine that determines all the parameters at once. Not only that this approach would be far too time consuming, but also due to the degeneracy in many of the parameters one would not get any reasonable result.

Instead, it is more handy to estimate several parameters from the observed data and then run a simulation with only a few degrees of freedom. The resulting light curves can then be fitted to the observation. The parameters of the best fitting ones are then improved by further simulations and fits until one ends up with a single best fit model. The single steps can be summarized as follows:

- Determine the orbital period from the observed light curve by measuring the distance between successive major peaks or computing a periodogram.
- Choose most suitable configurations from table 4.2 that have orbital periods close to the one measured[1].
- Estimate heating and cooling timescales ($\sigma_{\mathrm{rise}}, \sigma_{\mathrm{decay}}$), peak fluxes ($k_{\mathrm{peak}}$) and peak times ($T_{\mathrm{peak}}$) of blob and arc as well as the shear time (τ_{shear}) and the number of orbital periods (n) from the shape of the observed light curve.
- Run a simulation for each configuration with this set of parameters.
- Fit the resulting light curves to the data-points of the observation by reshifting in x (time) and rescaling in y (brightness). We're free to do this since the absolute values for the occurrence and the peak-flux of the flare are not specified by the simulations, they are free parameters.
- Pick the best-fit model(s) and try to improve the values of the parameters mentioned above.

[1] Of course there are many combinations of orbital radius and spin-parameter that give the same orbital period, but since the influence of the black hole spin on the shape of light curves and centroid tracks is marginal, we decide on those configurations and use them to constrain the other parameters.

- Start a simulation with these new values and fit the computed light curves to the real flare again.
- Repeat the last two steps a number of times until the fit cannot be improved anymore.

In order to evaluate the quality of a fit it is helpful to compute the corresponding *reduced chi-square*, defined as

$$\chi^2 := \frac{1}{N-F} \sum_{i=1}^{N} \left(\frac{\overline{S_{\mathrm{m}}}(t_i) - \overline{S_{\mathrm{s}}}(t_i)}{d\overline{S_{\mathrm{m}}}(t_i)} \right)^2 \tag{5.8}$$

where $\overline{S_{\mathrm{m/s}}}(t_i)$ is the i'th data-point of the light curve at the time t_i ('m' for *measured* and 's' for *simulated*), $d\overline{S_{\mathrm{m}}}(t_i)$ the corresponding error, N the total number of data-points and F the number of free parameters in the fit. Here, $F = 2$ due to the freedom of scaling in the y-direction and shifting in the x-direction. The reduced chi-square estimates the goodness of a fit and ideally takes the value one (for Gaussian noise). In this case the data-points of the fitting function are compatible with the error bars of the measured data. The higher the reduced chi-square the poorer the fit.

The above procedure was applied to two of the best IR-flares ever observed from the Galactic Center. The best fits for these are presented below.

5.3.2 L-band flare from April 4, 2007

Photometry

The light curve of this flare was already presented in the introduction. It has three major, fairly broad peaks with quite a substructure. Additionally, four smaller peaks are found on the wings of the light curve. The periodogram indicates a periodic timescale of about 23 minutes. The configurations at hand with the closest orbital period to that timescale are the ones with $r = 1.5 r_{\mathrm{LSO}}$ and $a = 0.7M$ yielding $T_{\mathrm{circ}} = 22.6\mathrm{min}$.

The peaks in the flare-data don't give any indication for gravitational shear since there is no broadening with time. For this reason we start the simulations with an already extended arc with a constant elongation. The parameter to describe its shape is the arc-extension Δ defined in equation (4.20). But, instead of using this definition we simply replace the right hand side by a constant number determining the full width half maximum of the Gaussian extension.

In Figure 5.15 the best fits for four different inclinations are shown. Each light curve constitutes $n = 7$ orbital motions of a compact blob ($\alpha^{\mathrm{s}} = 0$) with a constantly extended arc ($\alpha^{\mathrm{a}} = -3$). The simulation parameters found from the fit are given in Table 5.1.

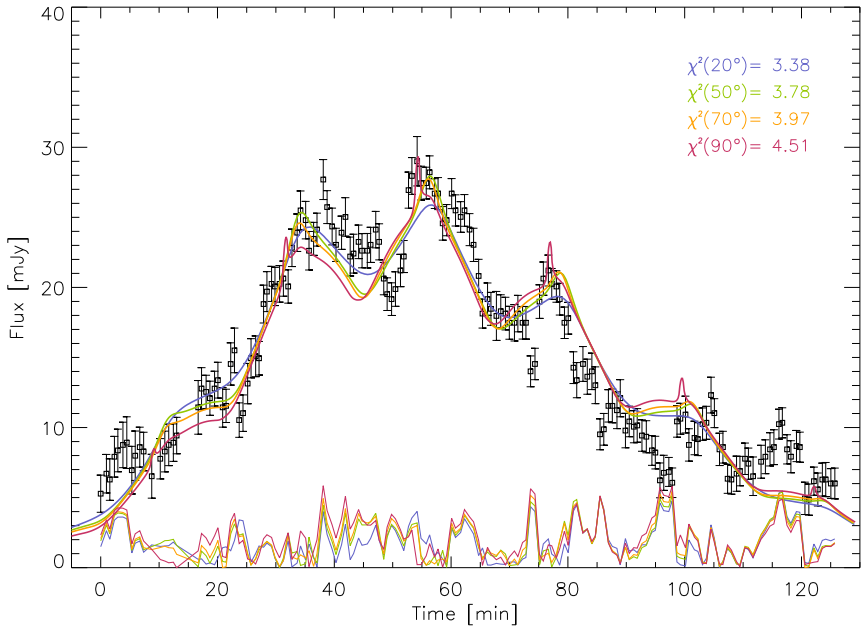

Figure 5.15: Best-fit light curves for the L-band flare from April 4, 2007. Colors indicate the inclination (blue: 20°, green: 50°, yellow: 70° and red: 90°), the corresponding reduced chi-square values are given in the upper right of the plot. At the bottom the residuals of the fit are drawn.

	$\sigma_{\rm rise}$	$\sigma_{\rm decay}$	$k_{\rm peak}$	$T_{\rm peak}$	Δ
Blob	$1.1T_{\rm circ}$	$1.8T_{\rm circ}$	3	$3.3T_{\rm circ}$	-
Arc	$1.1T_{\rm circ}$	$1.8T_{\rm circ}$	1	$3.3T_{\rm circ}$	$1.2T_{\rm circ}$

Table 5.1: Best-fit parameters for the L-band flare from April 4, 2007.

Obviously, the reduced chi-square values favor lower inclinations. However, this should not be taken too seriously for the following reasons:

First, the arc-extension Δ and the inclination are degenerate parameters which both determine the width and the hight of the peaks. If Δ is raised, at some point the order of the chi-square values is reversed in terms of inclinations.

Second, the fit gets worse towards the wings of the flare. By checking the distances between the major peaks one finds that the outer peaks don't match the 23 minutes timescale anymore. However, the flux in these parts of the light curve is quite low and may more strongly be influenced by background sources (the errors might be underestimated). For these reasons the very low flux levels should be considered as less significant.

Higher inclinations produce sharper sub-peaks on top of the major peaks. These are generated by the compact blob and may reproduce some substructure in the observed flare quite well. The Einstein ring peaks in the 90° case are still compatible with the data, however, the sampling of the instrument is too wide to constrain them. An unambiguous detection of such a peak could directly suggest the occurrence of an Einstein ring, a high-order general relativistic effect.

Periodogram

Having found a reasonable fit to the observed flare light curve it is of interest to extract its periodic properties by computing a periodogram and comparing it to the one obtained from the experimental data. To this end we use a routine called *Lomb normalized periodogram*, which belongs to the data analysis software *IDL* (*Interactive Data Language*) and is a standard tool for analyzing time series.

In order to make the simulated and the observed data best comparable, we pick out only those data-points from the simulated light curve that lie closest in time to the ones measured. Thus we get the same amount of data-points and nearly the same sampling.

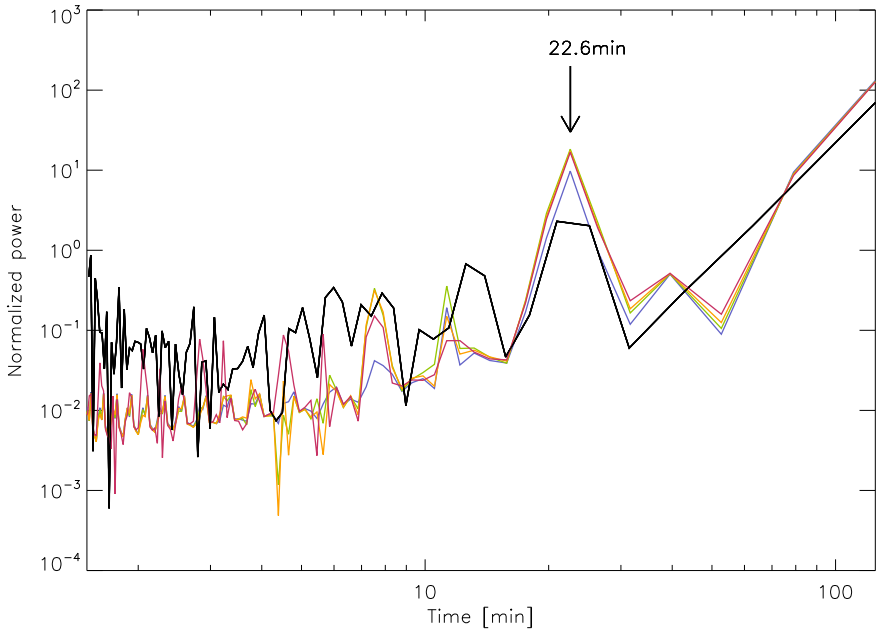

Figure 5.16: Lomb normalized periodogram of the best-fit light curves from Figure 5.15 and the observed light curve (black).

The periodograms for the four best-fit light curves from above and the observed flare are plotted in Figure 5.16. Obviously, the 23min-feature is nicely reproduced in the simulated data. Higher inclinations show more power in the periodogram due to the fact that the peaks in the corresponding light curves are higher and more confined. The rise towards higher timescales is caused by the overall structure of the flare light curves, yielding a periodic timescale of the whole flare duration.

Higher frequencies, though, are suppressed in comparison to the observed data. This is due to the fact that the source as well as the observing instrument generate intrinsic noise. While the power spectral density (PSD) of the instrumental noise is usually Gaussian (i.e. constant), the one generated by the source may have a more complicated profile (like a broken power law, for instance). In this case the periodogram of the observed flare shows a slight rise to longer timescales.

It is still being discussed in the scientific community which kind of physical processes could generate these profiles in the PSD and how to distinguish between purely random processes and distinct non-probabilistic events. The quality of this flare data is still not considered good enough to unambiguously rule out a random physical process in favor of a rotating hot spot model. Still it is remarkable how well the simulated periodograms fit the measured ones. The basic assumption of a periodically moving object in our model does not produce a significantly higher power in the orbital timescale than the power in the observed characteristic timescale. Also the rise towards longer timescales below the orbital period is present.

If we want to include the observational process into our simulations we can artificially add noise to our data. We can also mimic the flux-integration at the detector of the telescope by using the method described in section 4.1.3. Figure 5.17 shows the light curves from above, treated with the said procedure. First, the light curves were integrated with an integration time of 45 seconds, which is the average value from the observation. Then, a normally (Gaussian) distributed noise with a mean of zero and a standard deviation of 5 percent of the flare-peak-flux was superimposed. This value can be obtained by comparison of the mean error in the flare-data to its maximum flux-value.

Running a periodogram on these new light curves leads to the result presented in Figure 5.18. The power in the high frequencies is raised and has a flat shape, pretty similar to the observed data (the fact that there is more power in the simulated periodograms at short timescales may be due to an overestimation of the observational errors). The peaks associated with the 23min-timescale now match up very well, a slight discrepancy can be found in the middle part of the spectrum, where the observation suggests higher power in slightly shorter timescales. One could argue to have an underlying red noise process here, but this is yet a vague conclusion.

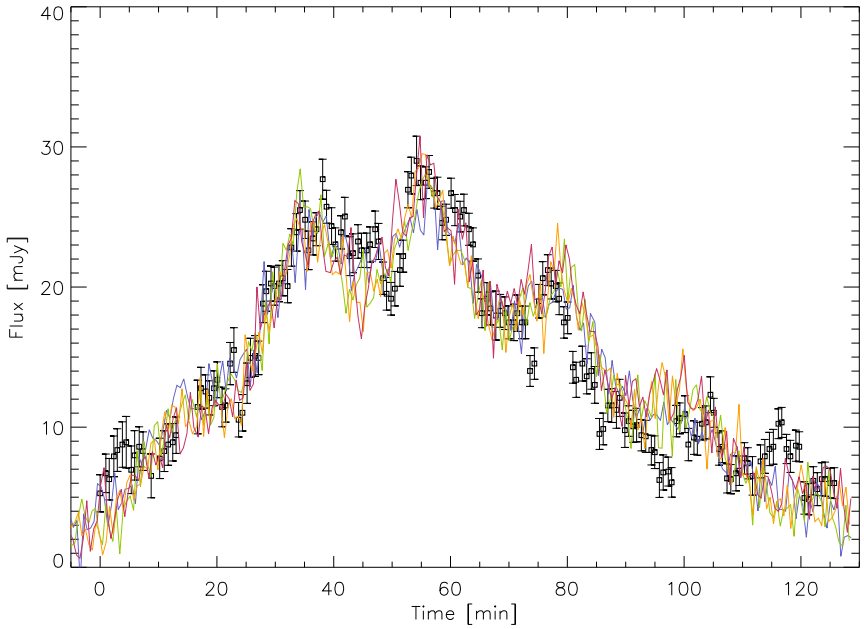

Figure 5.17: Best-fit light curves from Figure 5.15, added with Gaussian noise.

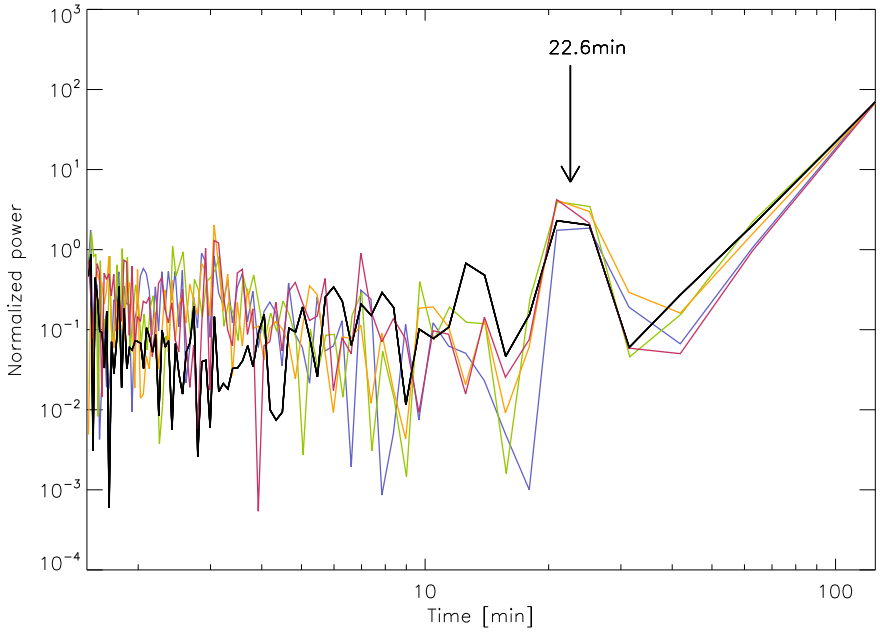

Figure 5.18: Lomb normalized periodogram of the noisy light curves from Figure 5.17 and the observed light curve (black).

Astrometry

Having acquired the best-fit parameters for a particular flare light curve one can immediately use them to compute the corresponding centroid tracks. These are direct predictions of our flare-model and may be checked against real observations in the future.

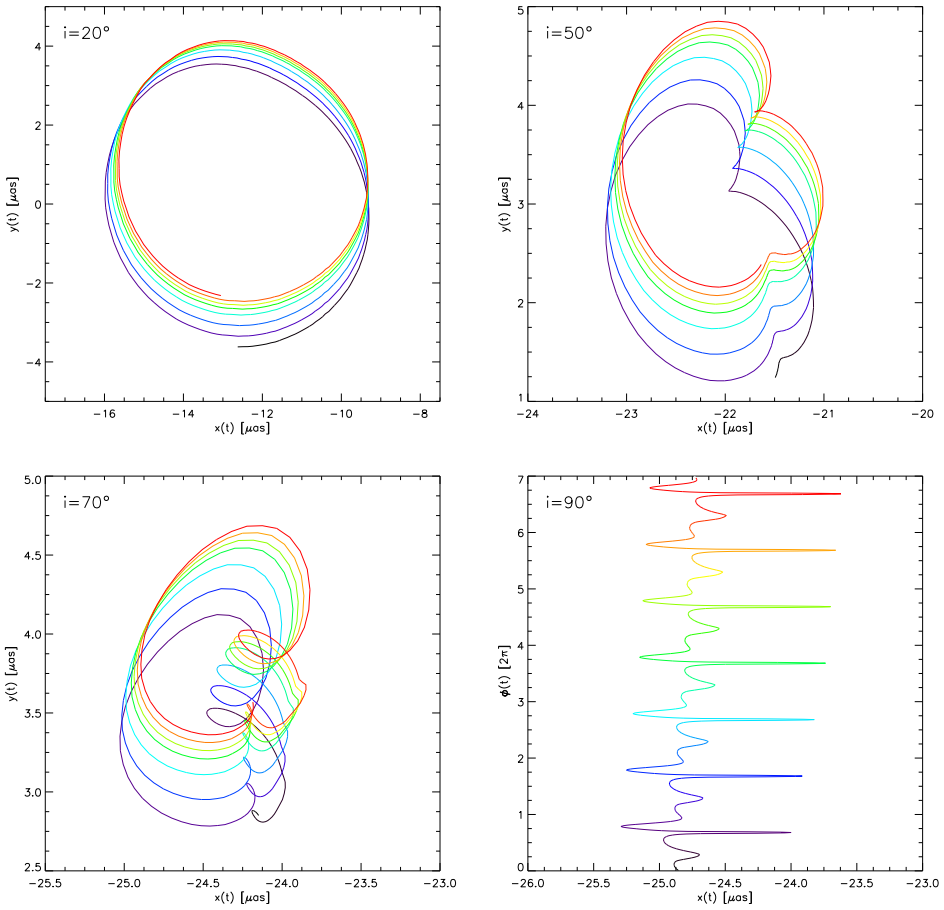

Figure 5.19: Centroid tracks of the best-fit model for the L-band flare from April 4, 2007 for different inclinations. The progression of the centroid motion is indicated via color coding, changing from black to violet, blue, green, yellow and finally red.

In Figure 5.19 the centroid tracks of the four best-fit models from above are displayed. At first glance they seem to show strong relativistic effects, but a look at the axis labeling reveals their scaling. Due to the rather strong contribution of the extended arc ($k^{\mathrm{s}}_{\mathrm{peak}}/k^{\mathrm{a}}_{\mathrm{peak}} = 3/1$), the centroid of emission is not moving far, yielding deflections of at most 2μas relative to its starting point. The centroid track is dragged to the approaching side because of relativistic beaming, additionally, lensing effects shift it upwards.

The higher the inclination the stronger are these effects, except for the 90° case where symmetry avoids a shift in the y-direction. The evolution of the blob's and arc's intrinsic brightness makes the centroid track move a bit every orbit. As time goes by it draws off towards the upper right side of the field of view.

It may be impossible to astrometrically resolve a flare like this in the near future, but it is noteworthy that the smearing of the light source relatively strengthens the relativistic features in the centroid tracks.

5.3.3 L-band flare from July 22, 2007

Photometry

Another fairly bright flare from the Galactic Center was caught in July 2007 at the VLT under good observing conditions (see Figure 5.20). Only a few short interruptions on account of calibration issues had to be carried out, causing gaps in the light curve data. Qualitatively, this light curve appears quite differently compared to the one before. The major peaks are more prominent and the overall rise and decay of the whole flare light curve is suppressed. In particular, the separation of the peaks is noticeable, amounting to roughly 45 minutes.

In order to fit this flare one needs to assume a larger orbital radius of the orbiting material and a more compact emission region. To this end we use the same flare-model as before and find the best-fit parameters given in Table 5.2. We used configurations with $r = 2.0 r_{\mathrm{LSO}}$ and $a = 0.52M$ yielding an orbital period of 45.4 minutes and simulated $n = 5$ orbits.

	σ_{rise}	σ_{decay}	k_{peak}	T_{peak}	Δ
Blob	$0.5T_{\mathrm{circ}}$	$1.0T_{\mathrm{circ}}$	85	$1.8T_{\mathrm{circ}}$	-
Arc	$4.0T_{\mathrm{circ}}$	$7.0T_{\mathrm{circ}}$	1	$1.8T_{\mathrm{circ}}$	$1.05T_{\mathrm{circ}}$

Table 5.2: Best-fit parameters for the L-band flare from July 22, 2007.

The resulting best-fit light curves are superimposed on the flare-plot in Figure 5.20. The corresponding reduced chi-square values suggest an even better approximation than in the April flare. Because the blob is dominant in this fit, the 90° case shows very strong Einstein ring peaks, by far exceeding the observed flux. The arc only contributes little to the light curve flux, it just broadens the wings of the major peaks. Its rise- and decay-time is so long that it barely varies in brightness.

In contrast, the blob must vary much stronger in order to reproduce the observed peaks. Although its rise- and decay-time seems to be very short in terms of the orbital period, it is comparable to the same timescales in the April flare. Multiplying the orbital period leads to $\sigma^{\mathrm{s}}_{\mathrm{rise}} = 22.7\mathrm{min}$, $\sigma^{\mathrm{s}}_{\mathrm{decay}} = 45.4\mathrm{min}$ for the July flare and $\sigma^{\mathrm{s}}_{\mathrm{rise}} = 24.9\mathrm{min}$, $\sigma^{\mathrm{s}}_{\mathrm{decay}} = 40.7\mathrm{min}$ for

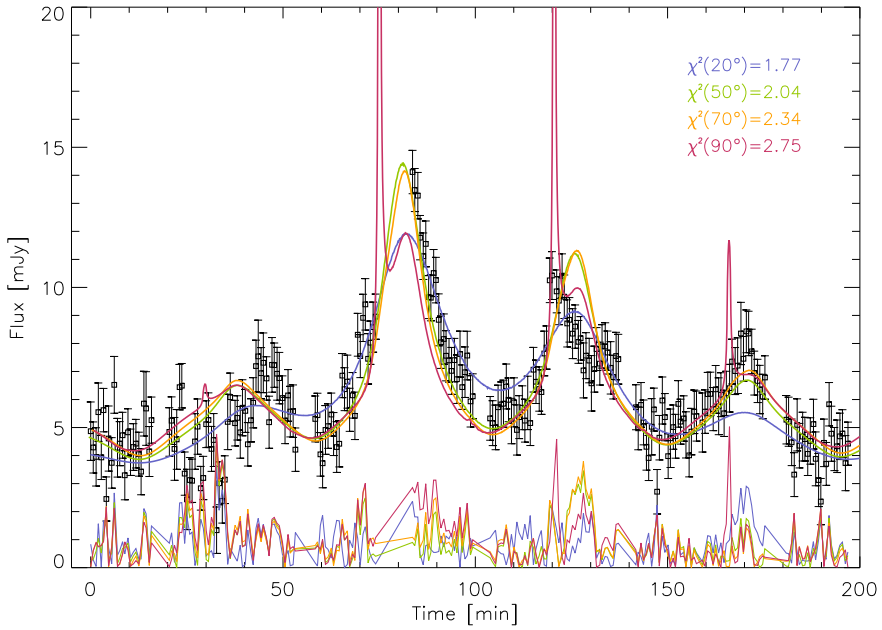

Figure 5.20: Best-fit light curves for the L-band flare from July 22, 2007. Colors indicate the inclination (blue: 20°, green: 50°, yellow: 70° and red: 90°), the corresponding reduced chi-square values are given in the upper right of the plot. At the bottom the residuals of the fit are drawn.

the April flare. This surprising concordance might indicate a fundamental heating- and cooling-process of the flares, not changing from one event to the other.

Periodogram

A simulated realistic observation is shown in Figure 5.21 using an integration time of 50 seconds and a Gaussian noise with a standard deviation of 6 percent of the flare-peak-flux (average values from the data). The corresponding periodogram is given in Figure 5.22. It yields quite a good agreement between the simulations and the observation. The power in the characteristic timescale of the flare exceeds the one in the April flare by nearly one order of magnitude. This is due to the concentrated emission of the compact blob in the center of the hot spot, which produces more accentuated peaks in the light curves.

The fit at the middle part of the spectrum shows a better agreement in the July flare. The slightly too high power in the upper frequencies again suggests an overestimation of the errors in the measurement.

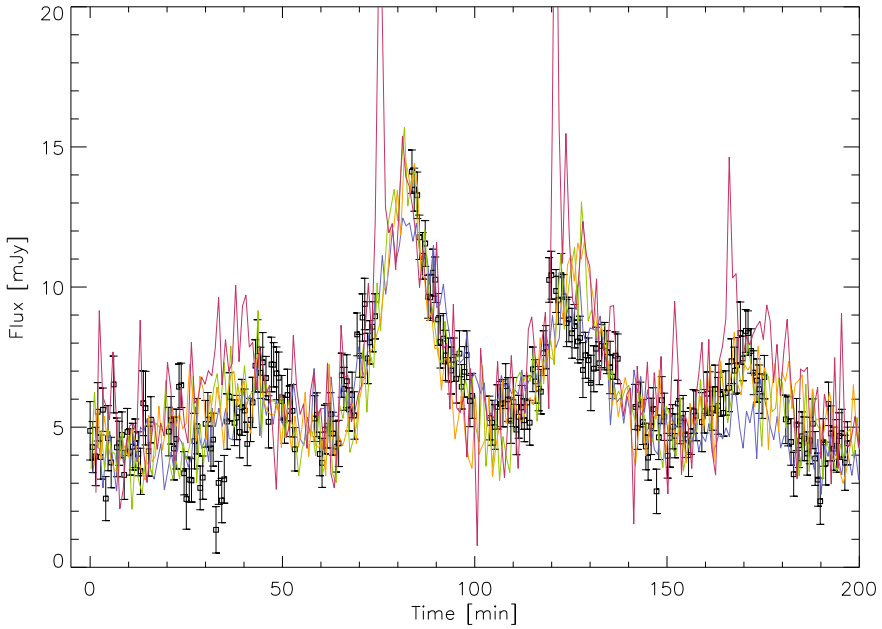

Figure 5.21: Best-fit light curves from Figure 5.20, added with Gaussian noise.

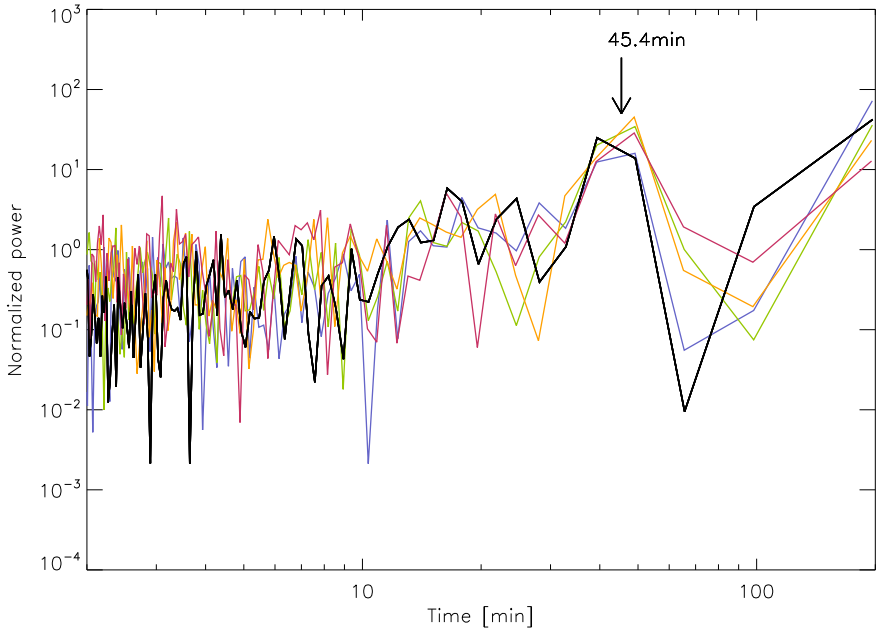

Figure 5.22: Lomb normalized periodogram of the noisy light curves from Figure 5.21 and the observed light curve (black).

Astrometry

The astrometric motion of the centroid, as it results from this fit, yields better prospects regarding future measurements than the April flare. As can be seen in Figure 5.23, diameters of up to 40μas are reached in the centroid tracks. This is due to the bright compact component in this model. Because the blob's brightness varies strongly, the centroid deflection grows first and then shrinks again, until it finally reaches its starting point.

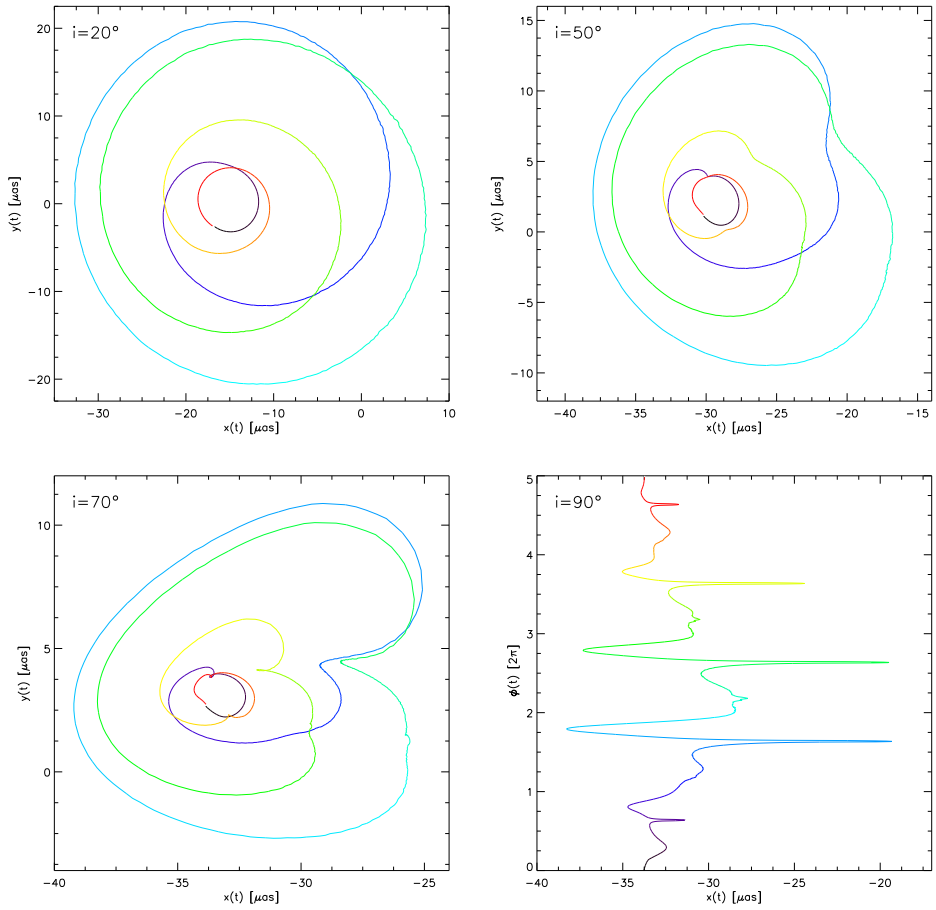

Figure 5.23: Centroid tracks of the best-fit model for the L-band flare from July 22, 2007 for different inclinations. The progression of the centroid motion is indicated via color coding, changing from black to violet, blue, green, yellow and finally red.

As for the light curves, observations of the centroid motion as it might be possible in future experiments can be simulated. Therefore we again integrate every 50 seconds and add a Gaussian noise to both the x- and y-component of the centroid. Its standard deviation is chosen to be 10μas,

the aimed resolution of ground-based interferometric instruments.

Figure 5.24 displays the obtained data-points of this procedure. In order to shrink the error bars, it is useful to average over several successive points (here about 10). In the cases of 50° and 70° inclination the plots additionally contain the $x(t)$ versus $\phi(t)$ motion of the centroid (shifted to $x(0) = 0$) to visualize its deflection more clearly.

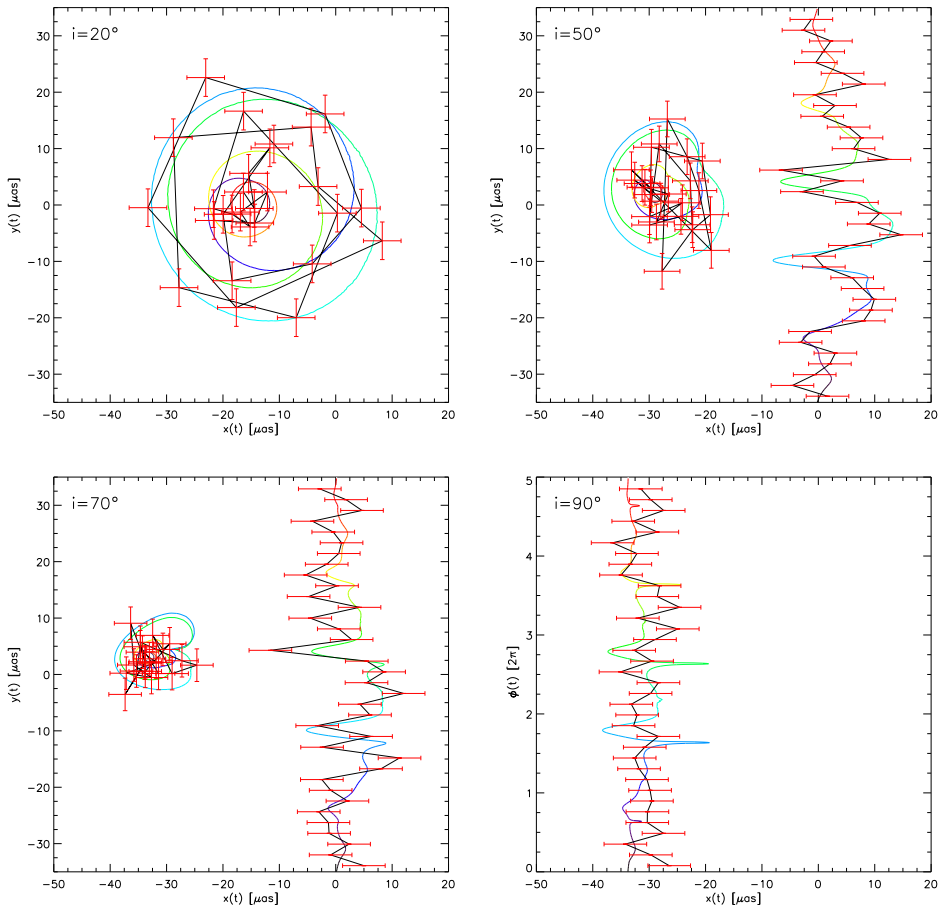

Figure 5.24: Centroid tracks from Figure 5.23, superimposed by simulated data-points obtained by an instrument with 50 seconds integration time and 10μas resolution. The cases of 50° and 70° inclination additionally contain the $x(t)$ versus $\phi(t)$ motion of the centroid shifted to $x(0) = 0$.

Obviously, the centroid tracks in higher inclinations are harder to catch. Nevertheless, significant deflections of the centroid can be measured in most cases. A comparison of many different flare events could further constrain the configuration of hot spot and black hole.

Chapter 6

Analytic approach

To a certain extent it is possible to derive some observable properties of the hot spot model analytically. Of course, several simplifications and approximations have to be considered in order to keep the calculations simple. In the following we will neglect:

- Relativistic lensing effects (responsible for the distortion of an image, changing light travel times and the occurrence of multiple images)
- The finite extension of the source
- The acceleration of the source's frame of reference

The remaining relativistic effects to be considered are the relativistic Doppler effect caused by the high velocity of the orbiting source and the gravitational redshift due to the curvature of spacetime. Both are responsible for frequency shifts of radiation, as we have seen in section 2.1. However, in the Kerr metric, the notions of Doppler shift and gravitational redshift cannot be treated as independent quantities anymore due to the effect of frame dragging.

A generalized *redshift factor* z_{Kerr} can be extracted from the metric by simply plugging in the properties of the circular orbit, namely:

$$dr = 0 \quad , \quad \theta = \frac{\pi}{2} \quad , \quad d\theta = 0 \quad , \quad d\phi = \omega_{\mathrm{circ}} dt \tag{6.1}$$

This yields:

$$\begin{aligned} ds^2 = c^2 d\tau^2 &= \left(1 - \frac{R_s r}{\Sigma}\right) c^2 dt^2 + \frac{2\omega_{\mathrm{circ}} R_s r a c}{\Sigma}\, dt^2 - \frac{\omega_{\mathrm{circ}}^2 A}{\Sigma}\, dt^2 = \\ &= \left(1 - \frac{R_s}{r}\right) c^2 dt^2 + \frac{2\omega_{\mathrm{circ}} R_s a c}{r}\, dt^2 - \omega_{\mathrm{circ}}^2 \left(r^2 + a^2 + \frac{R_s a^2}{r}\right) dt^2 \end{aligned} \tag{6.2}$$

and thus:

$$z_{\mathrm{Kerr}} = \frac{d\tau}{dt} = \sqrt{\left(1 - \frac{R_s}{r}\right) + 2\omega_{\mathrm{circ}}\frac{R_s a}{rc} - \frac{\omega_{\mathrm{circ}}^2}{c^2}\left(r^2 + a^2 + \frac{R_s a^2}{r}\right)} \quad (6.3)$$

This expression allows to transform between the proper time of the moving object close to the black hole and the coordinate time of the remote observer. Due to the finite propagation speed of light we still have to consider the stretch or compression of signals when the source is moving with a nonzero line of sight velocity $v\cos\vartheta$ with respect to the observer. Hence, the number D from subsection 3.2.2 can be expressed as:

$$D \equiv \frac{\nu_o}{\nu_s} = \frac{z_{\mathrm{Kerr}}}{1 - \beta\cos\vartheta} \quad (6.4)$$

ϑ depends on the location of the source on its orbit (orbital phase $\phi = \omega_{\mathrm{circ}}\tau$) and the inclination i of the orbital plane. Assuming the distance between source and observer to be infinite one simply gets:

$$\cos\vartheta = -\sin(i)\sin(\omega_{\mathrm{circ}}\tau) \quad (6.5)$$

The minus sign appears here, because we assign $\tau = 0$ to the, with respect to the observer, closest point of the clockwise orbiting hot spot. Finally, the velocity v of the source can be calculated from equation (2.119). It depends on the orbital radius and the spin-parameter.

Now we can also approximate the emission time T of the light rays from the source if we neglect the change of light travel time in different light rays. Therefore we simply integrate equation (6.4):

$$\begin{aligned} T \equiv t = \int_0^\tau D^{-1}\, d\tau' &= \frac{1}{z_{\mathrm{Kerr}}}\int_0^\tau \Big(1 + \beta\sin(i)\sin(\omega_{\mathrm{circ}}\tau')\Big)\, d\tau' = \\ &= \frac{1}{z_{\mathrm{Kerr}}}\Big[\tau - \frac{\beta}{\omega_{\mathrm{circ}}}\sin(i)\Big(\cos(\omega_{\mathrm{circ}}\tau) - 1\Big)\Big] \end{aligned} \quad (6.6)$$

6.1 Photometry

As long as the image of the source is not markedly distorted during one revolution, it roughly occupies a constant area on sky. The total flux is then only modulated via frequency shifts and relativistic beaming, assuming a constant intrinsic brightness of the source. This and equation (4.5) yields:

$$\overline{S_o} \propto S_o \propto D^{4-\alpha} \quad (6.7)$$

Plotting the integrated flux density $\overline{S_o}$ against the emission time T and normalizing the resulting curve to its minimum, allows us to compare it to the simulated light curves of the compact blob-model. In Figure 6.1 this

is illustrated with increasingly relativistic configurations. One can clearly distinguish the limits of our approximation. It mainly deviates due to the negligence of multiple images, but since these only contribute significantly in cases of high inclination and/or low orbital radius, it is quite good. In this way it enables us to disentangle the influence of relativistic lensing from all other effects in the light curves.

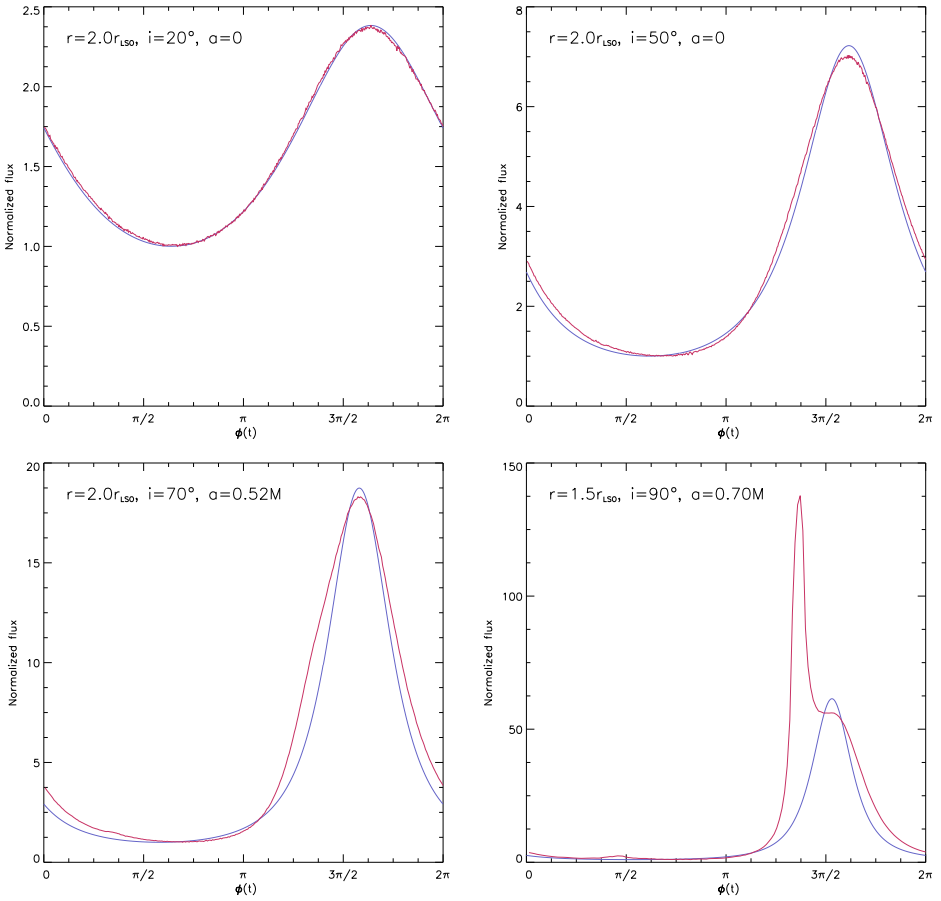

Figure 6.1: Comparison of analytically derived light curves (blue) with simulated light curves from the compact-blob model (red) in various configurations.

The light curve is a function of the orbital radius, the inclination, the spin-parameter and the spectral index:

$$\overline{S_o} = \overline{S_o}(r, i, a, \alpha) \tag{6.8}$$

An advantage of the analytical approach is the possibility to vary these parameters continuously. A characteristic property of each light curve is its *amplification* A, defined in equation (5.2). It can easily be determined using

our approximation:

$$A \approx 2.5\log_{10}\left(\frac{D^{\max}}{D^{\min}}\right)^{4-\alpha} = 2.5\,(4-\alpha)\log_{10}\left(\frac{1+\beta\sin(i)}{1-\beta\sin(i)}\right) \tag{6.9}$$

Figure 6.2 shows how A depends on these parameters in this approximation. We must expect strong deviations from these curves at high inclination or small orbital radius, since then multiple images cannot be neglected.

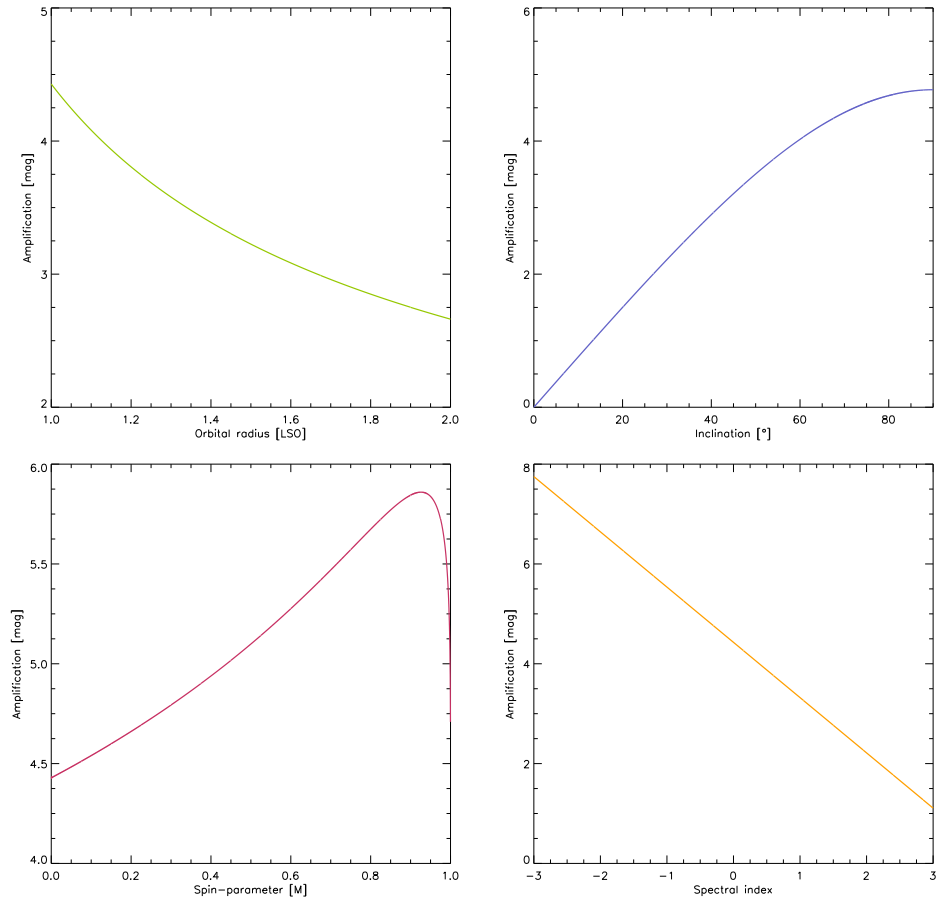

Figure 6.2: Dependency of the amplification on orbital radius, inclination, spin-parameter and spectral index in the analytic light curves. In each plot one of these parameters is varied and all the other ones are held constant with values: $r = 1.0r_{\mathrm{LSO}}$, $i = 70°$, $a = 0$, $\alpha = 0$.

The dependency on the spin-parameter looks somewhat unexpected at first glance. The amplification starts to rise as the spin increases, but suddenly falls down again at high spin. This is due to the character of the hot spot-velocity on the last stable orbit, which is influenced by two counteracting effects. Increasing the spin-parameter on the one hand leads to smaller

orbital radii and thus to higher orbital velocities (according to Kepler's third law). On the other hand, frame dragging becomes stronger and the orbital velocity in the locally nonrotating frame decreases. The turnaround happens when the last stable orbit enters the ergosphere.

6.2 Astrometry

Applying the above derived approximation to compute the centroid of emission in our simplified model yields:

$$\begin{aligned}\overrightarrow{C} &\equiv \frac{1}{\int S_o(x,y)\,dx\,dy}\begin{pmatrix}\int S_o(x,y)\cdot x\,dx\,dy\\ \int S_o(x,y)\cdot y\,dx\,dy\end{pmatrix} \approx \\ &\approx \frac{1}{\int \overline{S_o}\,\delta(x-x_0)\delta(y-y_0)\,dx\,dy}\begin{pmatrix}\int \overline{S_o}\,\delta(x-x_0)\delta(y-y_0)\cdot x\,dx\,dy\\ \int \overline{S_o}\,\delta(x-x_0)\delta(y-y_0)\cdot y\,dx\,dy\end{pmatrix} = \\ &= \frac{1}{\overline{S_o}}\begin{pmatrix}\overline{S_o}\,x_0\\ \overline{S_o}\,y_0\end{pmatrix} = \begin{pmatrix}x_0\\ y_0\end{pmatrix} \qquad (6.10)\end{aligned}$$

where x_0 and y_0 are the classical coordinates of the blob-center on sky. Thus the centroid track is an ellipse just as in the classical case, because we're omitting lensing effects. In order to derive its proper shape we would have to include the computation of geodesics for all points and directions, which goes beyond the scope of this work. For this, the numerical approach is convenient.

Chapter 7

Conclusion

We have studied the hot spot model as a physical origin of the observed flares from the Galactic Center. To this end we created a model for the hot spot emission and applied general relativistic ray tracing simulations to visualize its appearance for a remote observer.

In the case of a confined spherical emission-region (compact blob-model) various relativistic effects can be studied in detail. Both light curves and centroid tracks show strong deviations from the laws of classical physics, especially if the hot spot is close to the black hole and its orbit is highly inclined. In such configurations the occurrence of Einstein rings and multiple images can be inferred from the substructure in the data. The spin of the central black hole can be determined by combining photometric and astrometric measurements.

A more advanced model for the hot spot assumes an elongation of the compact source with a certain temporal evolution (shearing blob-arc-model). Gravitational shear gradually modifies the shape of light curves and centroid tracks with time and thereby "washes out" the substructure caused by high-order relativistic effects. Most rigorously this happens at small orbital radii and high black hole spins.

The parameters of this model can be adjusted in such a manner that the observed light curves from the Galactic Center (SgrA*) can be reproduced fairly well. The best fit models for the flares from April 4 and July 22, 2007 both suggest a negligible shear of the hot spot. Anyhow, some properties of the hot spot seem to vary from flare to flare, such as the orbital radius or the contribution of the arc. An analysis of the simulated light curves in frequency space yields an astonishing agreement with the observed data. This fact strongly supports the hot spot model.

The centroid tracks from the best fit models anticipate future high resolution measurements. Especially the July-case announces the possible detection of a centroid motion. Such a measurement would not only further constrain the hot spot model, but also probe spacetime in the strong field

limit of general relativity. Thus, the simulations provide theoretical predictions from fundamental physics that can be tested in the near future.

There are several ways to further extend the simulations for the hot spot model. For instance one could vary the radius of the emitting sphere and study its influence on light curves and centroid tracks. Additionally, other types of orbital motion could be investigated, like orbits off the equatorial plane or plunge orbits. Last but not least it is possible to model the polarization of the hot spot emission and study the influence of relativistic effects on polarization degree and polarization angle a remote observer would measure. This method provides further constraints on the black hole spin and the orientation of the orbital plane. However, these simulations are a great deal more time-consuming and require further parameters to be determined for the model.

Appendix A

Fundamental constants and units

Gravitation constant	G	=	$6.673 \cdot 10^{-11}\,\mathrm{m^3/kg\,s^2}$
Speed of light	c	=	$2.997924562 \cdot 10^{8}\,\mathrm{m/s}$
Planck's constant	h	=	$6.6263 \cdot 10^{-34}\,\mathrm{J\,s}$
Boltzmann's constant	k_B	=	$1.38 \cdot 10^{-23}\,\mathrm{J/K}$
Electron rest mass	m_e	=	$9.11 \cdot 10^{-31}\,\mathrm{kg}$
Proton rest mass	m_p	=	$1.67 \cdot 10^{-27}\,\mathrm{kg}$
Quantum of charge	e	=	$1.60 \cdot 10^{-19}\,\mathrm{A\,s}$
Solar mass	$M_\odot$	=	$1.989 \cdot 10^{30}\,\mathrm{kg}$
Solar radius	$R_\odot$	=	$6.96 \cdot 10^{8}\,\mathrm{m}$
Solar luminosity	$L_\odot$	=	$3.85 \cdot 10^{26}\,\mathrm{W}$
Astronomical unit	1AU	=	$1.5 \cdot 10^{11}\,\mathrm{m}$
Lightyear	1ly	=	$9.46 \cdot 10^{15}\,\mathrm{m}$
Parsec	1pc	=	$3.09 \cdot 10^{16}\,\mathrm{m}$
Jansky	1Jy	=	$10^{-22}\,\mathrm{W/m^2\,s\,Hz}$

Appendix B

Geometrized unit system

In this unit system, the speed of light, the gravitation constant and Boltzmann's constant are all set to unity:

$$c = G = k_B \equiv 1 \tag{B.1}$$

The standard unit, in terms of which length, time, mass, energy, momentum, etc. is measured, is centimeters. One obtains a desired value in geometrized units by multiplying the given SI value by a factor of unity, expressed through c, G and k_B, such that one gets centimeters.

For instance, the mass of the sun can be converted as follows:

$$M_\odot = 1.989 \cdot 10^{30}\,\mathrm{kg} = 1.989 \cdot 10^{30}\,\mathrm{kg} \cdot G/c^2 = 1.477 \cdot 10^5\,\mathrm{cm} \tag{B.2}$$

In order to go the other direction, one has to invert this procedure:

$$M_\odot = 1.477 \cdot 10^5\,\mathrm{cm} = 1.477 \cdot 10^5\,\mathrm{cm} \cdot c^2/G = 1.989 \cdot 10^{30}\,\mathrm{kg} \tag{B.3}$$

Appendix C

How to use the code developed in this work

Here, the procedure for running a simulation is described in detail. It may be of interest for someone who wants to continue this study on the hot spot model.

C.1 Processing raw data

The basis for all simulations are the ray-traced images delivered by *Thomas Müller*. A zip-file contains data for one particular configuration of orbital radius, inclination and spin-parameter, stated in the filename. It consists of ray-traced images for one full orbit of the particular configuration. These are subdivided into "frequency-shift" and "time-of-emission", containing the values T and D for every pixel, respectively. The data is stored in the *HDF5*-format (filename extension ".h5"), which is an open source data management tool for handling complex datasets. The scientific programming language *IDL* (Interactive Data Language) provides a package of procedures and functions to access these files. To read in the raw datasets, an *IDL*-script called `make-indexed.idl` is used. It does the following:

- Extract the zipped *HDF5*-files
- Read in the 1000×1000 pixel maps of T and D for every frame
- Only store those values unequal zero to save memory
- Assign an index to every nonzero pixel according to its position
- Store the indexed pixels in a *FITS*-file (Flexible Image Transport System, extension ".fits")

In order to facilitate the access to the desired configuration, a particular directory structure is applied. Each raw zip-file is stored in a directory

stating the corresponding grid-parameters, like `gc_a*_i*_rlso*_bs*`. The wildcard character "`*`" stands for the particular values of spin-parameter (a/M), inclination (i), orbital radius (r/r_{LSO}) and blobsize (this parameter hasn't been varied in this work, it is always $r_{\mathrm{blob}} = 0.25R_s$). This directory also contains the indexed files after processing. All these various configurations are found in the directory `Raw_data`. The script `make-indexed.idl` is called in *IDL* by typing

```
.run "make-indexed.idl"
```

in the command line from the directory of a particular configuration.

C.2 Running a simulation

The simulation of the hot spot model is implemented in *Yorick*. Before initializing the detailed properties of a simulation one has to decide on the basic model of the hot spot, namely:

- Compact blob-model (`run_blob.i`)
- Two oppositely situated compact blobs (`run_2blob.i`)
- Shearing blob-arc-model (`run_arc.i`)
- Constantly elongated blob-arc-model (`run_disk.i`)

In brackets, the filename of the corresponding main routine (simulation initializer) is stated. Each file allows to specify all the parameters for the related model. In order to run a simulation one has to:

- Specify a name for the simulation run (`simrun`)
- Choose the desired configurations to be simulated (`simlist`)
- Define resolution and duration of the simulation (`step`, `n_periods`)
- Specify the model-parameters (the names of the parameter-variables should be intuitively clear)
- Decide whether a video clip shall be created (`make-movie.i`)

To start the simulation for a compact blob-model, for instance, one has to run the corresponding main routine by typing

```
#include "run_blob.i"
```

in Yorick's command line from the root-directory `RotatingBlob`. The progression of a simulation is written into the terminal showing the actual frame that is being computed.

C.3 Simulation output

The output of a simulation run is stored in the directory `Simulations`, which contains the same directories as `RawData` . There, each grid-configuration directory contains the directories of the different simulation runs. The output consists of:

- A file `astrometry.fits` containing all the photometric and astrometric data computed in the simulation
- A file `parameters.txt` containing the model-parameters and other specifications of the simulation
- Preliminary plots of light curves and centroid tracks
- A video clip, if specified in the simulation initializer

In order to generate light curves and centroid tracks it is convenient to use *IDL*, since it provides nice plotting tools. The simulated data can be accessed by opening the file `astrometry.fits` and storing its contents in a two-dimensional array. The first dimension of this array specifies a particular quantity and the second dimension the frame number. There are ten quantities stored in the file:

1. Frame number
2. Coordinate time t
3. Integrated flux density $\overline{S_o}$ (light curve)
4. x-coordinate of centroid C_x
5. y-coordinate of centroid C_y
6. Minimum flux density value in the image $S_o^{\min}$
7. Maximum flux density value in the image $S_o^{\max}$
8. Averaged integrated flux density with noise $< \tilde{\overline{S_o}} >$
9. Averaged x-coordinate of centroid with noise $< \tilde{\overrightarrow{C_x}} >$
10. Averaged y-coordinate of centroid with noise $< \tilde{\overrightarrow{C_y}} >$

For example, a light curve is created by plotting the third against the second quantity of this array.

List of Figures

1.1 Pseudo-color image of the central parsec of the Milky Way in the near infrared 5
1.2 SgrA* flare light curves and periodogram 6
1.3 Schematic illustration of a star-disk interaction 7
1.4 Schematic illustration of the jet-model 8
1.5 Schematic illustration of the orbiting hot spot model 9
1.6 The Very Large Telescope on mount Paranal in Chile 10

2.1 Effective potential for test particles with different specific angular momenta in the Schwarzschild metric 26
2.2 Trajectories of test particles in the Schwarzschild metric . . . 27
2.3 Effective potential for photons with different specific angular momenta in the Schwarzschild metric 28
2.4 Event horizon and ergosphere of a Kerr black hole 31
2.5 Trajectory of a particle, falling into a Kerr black hole 33
2.6 Characteristic radii in the Kerr metric 35
2.7 Dependency of the orbital period on the spin-parameter and the orbital radius 36
2.8 Dependency of the orbital period on the spin-parameter and the orbital radius in units of the last stable orbit radius . . . 36

3.1 Concept of ray tracing 38
3.2 Ray traced image of three spheres that reflect off the floor and each other 38
3.3 Ray tracing in special relativity 39
3.4 Ray tracing in general relativity 41
3.5 Ray traced images of a sphere orbiting a Kerr black hole on the last stable orbit in 70° inclination 42
3.6 Real and apparent locations of the sphere at the observer's coordinates 43

4.1 An integrated image of a radiating sphere with extended arc . 48
4.2 Temporal and spatial intrinsic brightness distribution of a blob-arc-model 52

4.3 Dependency of the gravitational shear time on spin-parameter and orbital radius 54
4.4 Dependency of the gravitational shear time in units of T_{circ} on spin-parameter and orbital radius 55
4.5 Illustration of the magneto-rotational instability of a magnetized accretion disk around a rotating black hole. 56

5.1 Light curves of a compact hot spot orbiting a Schwarzschild black hole in different orbital radii and inclinations 59
5.2 Primary and secondary Einstein ring of a compact hot spot orbiting a Schwarzschild black hole 60
5.3 Light curves of a compact hot spot orbiting a black hole with different spin-parameters 61
5.4 Light curves of a compact hot spot with different spectral indices orbiting a Schwarzschild black hole 62
5.5 Centroid tracks of a compact hot spot orbiting a Schwarzschild black hole in different orbital radii and inclinations . . 63
5.6 Centroid tracks of a compact hot spot orbiting a black hole with different spin-parameters 64
5.7 Centroid tracks of a compact hot spot with different spectral indices orbiting a Schwarzschild black hole 65
5.8 Amplification of the light curve plotted against the horizontal diameter of the centroid track 66
5.9 Light curves and centroid tracks of one and two oppositely situated blobs 67
5.10 Sequence of two blobs orbiting a Kerr black hole 68
5.11 Light curves of the shearing blob-arc-model for different orbital radii and inclinations 70
5.12 Light curves of the shearing blob-arc-model for different black hole spins 71
5.13 Centroid tracks of the shearing blob-arc-model in different orbital radii and inclinations 72
5.14 Centroid tracks of the shearing blob-arc-model for different black hole spins 73
5.15 Best-fit light curves for the L-band flare from April 4, 2007 . 76
5.16 Lomb normalized periodogram of the best-fit light curves for the L-band flare from April 4, 2007 77
5.17 Best-fit light curves for the L-band flare from April 4, 2007 with noise 79
5.18 Lomb normalized periodogram of the L-band flare from April 4, 2007 with noise 79
5.19 Centroid tracks of the best-fit model for the L-band flare from April 4, 2007 80
5.20 Best-fit light curves for the L-band flare from July 22, 2007 . 82

5.21 Best-fit light curves for the L-band flare from July 22, 2007 with noise 83
5.22 Lomb normalized periodogram of the L-band flare from July 22, 2007 with noise 83
5.23 Centroid tracks of the best-fit model for the L-band flare from July 22, 2007 84
5.24 Centroid tracks of the best-fit model for the L-band flare from July 22, 2007, superimposed by simulated data-points 85

6.1 Comparison of analytically derived light curves with simulated light curves from the compact-blob model 88
6.2 Dependency of the amplification on orbital radius, inclination, spin-parameter and spectral index in the analytic light curves 89

Bibliography

[1] Balbus, S. A., and Hawley, J. F. A powerful local shear instability in weakly magnetized disks. I - Linear analysis. II - Nonlinear evolution. *ApJ 376* (July 1991), 214–233.

[2] Bao, G., Hadrava, P., and Ostgaard, E. Multiple images and light curves of an emitting source on a relativistic eccentric orbit around a black hole. *ApJ 425* (Apr. 1994), 63–71.

[3] Bardeen, J. M., Press, W. H., and Teukolsky, S. A. Rotating Black Holes: Locally Nonrotating Frames, Energy Extraction, and Scalar Synchrotron Radiation. *ApJ 178* (Dec. 1972), 347–370.

[4] Boyer, R. H., and Lindquist, R. W. Maximal Analytic Extension of the Kerr Metric. *J. Math. Phys. 8* (1967), 265–281.

[5] Broderick, A. E., and Loeb, A. Imaging bright-spots in the accretion flow near the black hole horizon of SgrA*. *MNRAS 363* (Oct. 2005), 353–362.

[6] Broderick, A. E., and Loeb, A. Imaging optically-thin hotspots near the black hole horizon of SgrA* at radio and near-infrared wavelengths. *MNRAS 367* (Apr. 2006), 905–916.

[7] Carter, B. Global structure of the Kerr family of gravitational fields. *Phys. Rev. 174* (1968), 1559–1571.

[8] Cunningham, J. M., and Bardeen, C. T. The Optical Appearance of a Star Orbiting an Extreme Kerr Black Hole. *ApJ 183* (July 1973), 237–264.

[9] De Villiers, J.-P., Hawley, J. F., and Krolik, J. H. Magnetically Driven Accretion Flows in the Kerr Metric. I. Models and Overall Structure. *ApJ 599* (Dec. 2003), 1238–1253.

[10] Eckart, A., Baganoff, F. K., Schödel, R., Morris, M., Genzel, R., Bower, G. C., Marrone, D., Moran, J. M., Viehmann, T., Bautz, M. W., Brandt, W. N., Garmire, G. P., Ott, T.,

Trippe, S., Ricker, G. R., Straubmeier, C., Roberts, D. A., Yusef-Zadeh, F., Zhao, J. H., and Rao, R. The flare activity of Sagittarius A*. New coordinated mm to X-ray observations. *A&A 450* (May 2006), 535–555.

[11] Eisenhauer, F. e. a. GRAVITY: The AO assisted, two object beam combiner instrument for the VLTI. *Astronomische Nachrichten 326* (Aug. 2005), 561–562.

[12] Eisenhauer, F. e. a. SINFONI in the Galactic Center: Young Stars and Infrared Flares in the Central Light-Month. *ApJ 628* (July 2005), 246–259.

[13] Falanga, M., Melia, F., Tagger, M., Goldwurm, A., and Bélanger, G. General Relativistic Flux Modulations from Disk Instabilities in Sagittarius A*. *ApJ 662* (June 2007), L15–L18.

[14] Falcke, H., and Hehl, F. W. *The Galactic Black Hole*. IoP Bristol and Philadelphia, 2003.

[15] Falcke, H., and Markoff, S. The jet model for SgrA*: Radio and X-ray spectrum. *A&A 362* (Oct. 2000), 113–118.

[16] Falcke, H., Melia, F., and Agol, E. Viewing the Shadow of the Black Hole at the Galactic Center. *ApJ 528* (Jan. 2000), L13–L16.

[17] Fliessbach, T. *Allgemeine Relativitätstheorie*. Spektrum, 2003.

[18] Genzel, R., Schödel, R., Ott, T., Eckart, A., Alexander, T., Lacombe, F., Rouan, D., and Aschenbach, B. Near-infrared flares from accreting gas around the supermassive black hole at the Galactic Centre. *Nature 425* (Oct. 2003), 934–937.

[19] Ghez, A. M., Hornstein, S. D., Lu, J. R., Bouchez, A., Le Mignant, D., van Dam, M. A., Wizinowich, P., Matthews, K., Morris, M., Becklin, E. E., Campbell, R. D., Chin, J. C. Y., Hartman, S. K., Johansson, E. M., Lafon, R. E., Stomski, P. J., and Summers, D. M. The First Laser Guide Star Adaptive Optics Observations of the Galactic Center: SgrA*'s Infrared Color and the Extended Red Emission in its Vicinity. *ApJ 635* (Dec. 2005), 1087–1094.

[20] Gillessen, S., Eisenhauer, F., Quataert, E., Genzel, R., Paumard, T., Trippe, S., Ott, T., Abuter, R., Eckart, A., Lagage, P. O., Lehnert, M. D., Tacconi, L. J., and Martins, F. Variations in the Spectral Slope of Sagittarius A* during a Near-Infrared Flare. *ApJ 640* (Apr. 2006), L163–L166.

[21] Hollywood, J. M., Melia, F., Close, L. M., McCarthy, Jr., D. W., and Dekeyser, T. A. General Relativistic Flux Modulations in the Galactic Center Black Hole Candidate Sagittarius A*. *ApJ 448* (July 1995), L21+.

[22] Kerr, R. P. Gravitational field of a spinning mass as an example of algebraically special metrics. *Phys. Rev. Lett. 11* (1963), 237–238.

[23] Luminet, J.-P. Image of a spherical black hole with thin accretion disk. *A&A 75* (May 1979), 228–235.

[24] Markoff, S., Falcke, H., Yuan, F., and Biermann, P. L. The Nature of the 10 kilosecond X-ray flare in SgrA*. *A&A 379* (Nov. 2001), L13–L16.

[25] Meyer, L., Eckart, A., Schödel, R., Duschl, W. J., Mužić, K., Dovčiak, M., and Karas, V. Near-infrared polarimetry setting constraints on the orbiting spot model for SgrA* flares. *A&A 460* (Dec. 2006), 15–21.

[26] Misner, C. W., Thorne, K. S., and Wheeler, J. A. *Gravitation.* Freeman San Francisco, 1973.

[27] Müller, A. *Black Hole Astrophysics: Magnetohydrodynamics on the Kerr Geometry.* PhD thesis, Ruperto-Carola University of Heidelberg, 2004.

[28] Müller, J., and Nordtvedt, K. Lunar laser ranging and the equivalence principle signal. *ApJ 58*, 6 (Sept. 1998).

[29] Müller, T. *Visualisierung in der Relativitätstheorie.* PhD thesis, Eberhard-Karls-Universität zu Tübingen, 2006.

[30] Nayakshin, S., Cuadra, J., and Sunyaev, R. X-ray flares from SgrA*: Star-disk interactions? *A&A 413* (Jan. 2004), 173–188.

[31] Novikov, I. D., and Frolov, V. P. *Physics of Black Holes.* Kluwer, 1989.

[32] Ori, A., and Thorne, K. S. Transition from inspiral to plunge for a compact body in a circular equatorial orbit around a massive, spinning black hole. *Phys. Rev. D 62*, 12 (Dec. 2000), 124022–+.

[33] Pacholczyk, A. G. *Radio Astrophysics.* Freeman San Francisco, 1970.

[34] Paumard, T. *Scientific motivation and VLTI context of GRAVITY*. GRAVITY Midterm Review Heidelberg, Mar. 2007.

[35] Paumard, T. e. a. Scientific prospects for VLTI in the Galactic Centre: Getting to the Schwarzschild radius. *Astronomische Nachrichten 326* (Aug. 2005), 568–568.

[36] Quataert, E. Radiatively Inefficient Accretion Flow Models of SgrA*. *Astronomische Nachrichten Supplement 324* (Sept. 2003), 435–443.

[37] Raychaudhuri, A. K., Banerji, S., and Banerjee, A. *General Relativity, Astrophysics and Cosmology*. Springer New York, 1992.

[38] Rindler, W. *Relativity*. Oxford, 2006.

[39] Sexl, R. U., and Urbantke, H. K. *Gravitation und Kosmologie*. Spektrum, 1995.

[40] Trippe, S., Paumard, T., Ott, T., Gillessen, S., Eisenhauer, F., Martins, F., and Genzel, R. A polarized infrared flare from Sagittarius A* and the signatures of orbiting plasma hotspots. *MNRAS 375* (Mar. 2007), 764–772.

[41] van Putten, M. *Gravitational Radiation, Luminous Black Holes and Gamma-Ray Burst Supernovae*. Cambridge, 2005.

[42] Yuan, F., Quataert, E., and Narayan, R. Nonthermal Electrons in Radiatively Inefficient Accretion Flow Models of Sagittarius A*. *ApJ 598* (Nov. 2003), 301–312.

[43] Yuan, F., Quataert, E., and Narayan, R. On the Nature of the Variable Infrared Emission from Sagittarius A*. *ApJ 606* (May 2004), 894–899.

[44] Zeldovich, Y. B., and Novikov, I. D. *Relativistic Astrophysics Vol. 1, Stars and Relativity*. University of Chicago press, 1971.

Acknowledgments

The completion of this work would not have been possible without the contribution of my collaborators and the support from my supervisors. To this end I want to thank:

Prof. Dr. Reinhard Genzel for giving me the possibility to work in the Galactic Center group at the MPE and to be involved with this very interesting subject of current research.

Dr. Stefan Gillessen for supervising the progression of my thesis, contributing many ideas to this work and being addressable for a lot of questions.

Dr. Thomas Müller for the good collaboration and the time he invested for running the ray tracing simulations. He also helped me with many technical issues of this work.

Dr. Thibaut Paumard for letting me continue his work and introducing me into the topic.

Furthermore I want to thank **Katie Dodds-Eden** for proofreading this thesis and the entire **Galactic Center team** for many fruitful discussions and the good working atmosphere in the institute.

Last of all I thank my parents who supported me throughout my studies and enabled me to write this thesis.

Eidesstattliche Erklärung

Hiermit erkläre ich, dass ich die vorliegende Arbeit selbstständig und ohne Benutzung anderer als der angegebenen Hilfsmittel angefertigt habe; die aus fremden Quellen direkt oder indirekt übernommenen Gedanken sind als solche kenntlich gemacht.

Die Arbeit wurde bisher in gleicher oder ähnlicher Form keiner anderen Prüfungskommission vorgelegt und auch nicht veröffentlicht.

München, den 8. Januar 2008